Channelrhodopsin Assisted Synapse Identity Mapping Reveals Clustering of Layer 5 Intralaminar Inputs

Onur Gökçe

München 2013

Channelrhodopsin Assisted Synapse Identity Mapping Reveals Clustering of Layer 5 Intralaminar Inputs

Onur Gökçe

Dissertation
of the Graduate School of Systemic Neurosciences
of Ludwig–Maximilians–Universität
München

Submitted by
Onur Gökçe

Munich, 16.10.2013

CHANNELRHODOPSIN ASSISTED SYNAPSE IDENTITY MAPPING REVEALS CLUSTERING OF LAYER 5 INTRALAMINAR INPUTS

Onur GÖKÇE

PhD Thesis, 2013

Thesis Supervisor: Dr. Volker SCHEUSS

Abstract

The computation in the brain is executed at different levels, from single synapses to ensembles of networks. Perception, behavior, and phenomena such as consciousness emerge from the activity of all levels. The synaptic input, which is mostly received on the dendrites of the neurons is integrated linearly or nonlinearly with other inputs as it propagates to the soma. There, depending on the strength of the signal, the neuron passes this information to its downstream partners in the network.

To be able to relate the computation of a single neuron to the computation of the network, the information on how and where the individual neurons integrate into the circuit is essential. For this reason, different techniques currently try to map the connectivity between different neurons in the network.

This study presents a new approach for connectivity mapping by utilizing the light activated cation channel, channelrhodopsin-2 (ChR2). Specific presynaptic neuronal populations are targeted genetically to express ChR2 and driven to fire action potentials by photostimulation. In individual spines of the target postsynaptic neurons, calcium signals evoked by the stimulated presynaptic neurons are detected. These sites reliably locate the input of the presynaptic neurons with single synapse resolution. By systematically scanning over the dendrites of the postsynaptic neurons, this technique yields input maps that exhibit the connectivity between the two neuronal populations.

Analysis of the spatial organization of these identified inputs reveals clustering in the connectivity between pre- and postsynaptic layer 5 neurons of the primary visual cortex.

Acknowledgments

I would like to express my uttermost gratitude towards,

Dr. Volker Scheuss, for his incredible supervision. I cannot remember a single time that he left my questions unanswered. He has always been available. He taught and led me. He kept my enthusiasm running at times when I wished for anything but science. This project could not have been possible without his input and help.

Prof. Dr. Tobias Bonhoeffer, for his long lasting support. His interest and belief in this project kept it alive. I feel privileged that he employed me and gave me the chance of experiencing his department. This experience had been irreplaceable.

Prof. Dr. Christian Leibold and Prof. Dr. Klaus Conzelmann, for their fruitful input and questions, as well as, for sparing their time to be a part of my thesis advisory committee.

Dr. Christiaan Levelt, for his unarguably essential know-how with the *in utero* electroporation surgeries. Without his tips and tricks it would not have been possible to apply the technique to this project.

Volker Staiger, Claudia Huber, Max Sperling and Frank Voss, for their assistance. They made everything run very smoothly.

Claudia Marget-Hahn, for her immediate action in any administrative help I needed.

The nice people of Graduate School of Systemic Neurosciences involved in the scientific and administrative organization, for giving me the opportunity to enter the neuroscience field, for the initial push, and for all of the bureaucratic assistance.

All past and present members of the Bonhoeffer Lab, for making me feel comfortable, for listening to my frustration and for soothing it.

Cvetalina Coneva, Marcus Knopp, Dr. Arnab Chakrabarty and Jens Kielow, for the warm companionship on this alien soil. You gave me the room to breathe.

Dr. Özge Canlı, for listening to me hours after hours. For the stimulation, for your opinion, and for all the things we shared. For simply being there for me, whenever.

Ahu, Hayat and Levend Gökçe, my family, for the limitless support. You always let me feel of your nearness. You could always motivate me. I am indeed lucky.

I just have these words and not a better combination to be sincere.
I am thankful, and I never forget.

With my deepest regards,
Onur Gökçe

Contents

List of Figures

Acronyms

4-AP 4-aminopyridine
ACSF artificial cerebrospinal fluid
AMPA α-amino 3-hydroxy 5-methyl 4-isoxazolepropionic acid
AMPAR AMPA receptor
AP action potential
API application programming interface
ChR2 channelrhodopsin-2
EM electron microscopy
EPSC excitatory postsynaptic current
EPSP excitatory postsynaptic potential
EYFP enhanced YFP
GABA γ-aminobutyric acid
GFP green fluorescent protein
GRASP GFP reconstitution across synaptic partners
GUI graphical user interface
hChR2(H134R) codon optimized ChR2 H134R mutant
HCN channel hyperpolarization-activated cation channel
HDF5 hierarchical data format
ID identifier
IP intraperitoneal
IPSC inhibitory postsynaptic current
IUE *in utero* electroporation
L2/3 layer 2/3
L4 layer 4
L5 layer 5
L6 layer 6
LTP long-term potentiation
mGRASP mammalian GRASP
NMDA N-methyl D-aspartate
NMDAR NMDA receptor
PCR polymerase chain reaction
PKA protein kinase A
ROI region of interest
SBSEM serial block face scanning electron microscopy
TEM transmission electron microscopy
Thy1-ChR2 Thy1-ChR2 transgenic line
TTX tetrodotoxin
UV ultraviolet
V1 primary visual cortex
VGCC voltage-gated Ca^{2+} channel
VGIC voltage-gated ion channel
WPRE woodchuck hepatitis virus posttranscriptional regulatory element
wtChR2 wildtype ChR2
YFP yellow fluorescent protein

Chapter 1

Introduction

Men ought to know that from nothing else but the brain come joys, delights, laughter and sports, and sorrows, griefs, despondency, and lamentations. And by this, in an especial manner, we acquire wisdom and knowledge, and see and hear, and know what are foul and what are fair, what are bad and what are good, what are sweet, and what unsavory; some we discriminate by habit, and some we perceive by their utility. By this we distinguish objects of relish and disrelish, according to the seasons; and the same things do not always please us. And by the same organ we become mad and delirious, and fears and terrors assail us, some by night, and some by day, and dreams and untimely wanderings, and cares that are not suitable, and ignorance of present circumstances, desuetude, and unskillfulness.

[...] Wherefore, I say, that it is the brain which interprets the understanding.

Hippocrates, *On the Sacred Disease*[1], 400 B.C.

The brain is a computing biological machine. Our current interpretation of its workings, and in this respect modern neuroscience research, is based on the neuron theory, or the neuron doctrine. The doctrine describes the brain as made up of individual units (neurons) consisting of specialized compartments such as dendrites, somata and axons. The information flows generally unidirectionally from the dendrites to the axons via the soma, then to the dendrites of downstream neurons upon synaptic transmission.

Santiago Ramón y Cajal, from his studies with Golgi staining, was the first to suggest in 1888 that dendrites and axons terminate and neurons communicate across specialized contacts. This hypothesis at the time contradicted to

---

[1] Translation by Francis Adams

the prevalent idea proposed by Gerlach, where the brain was considered to be a mesh of neuronal processes forming a continuum which harbors the computations. Gerlach's reticular theory was able to readily explain the flow of the currents and thus of the information. Cajal, later in 1891, postulated his law of dynamic polarization, where he could fit his observations of a discontinuous nervous system interrupted at the contact sites in explaining the information flow. He proposed that neurons had morphological and functional polarization; the dendrites and the soma functioning as the receptor apparatus, passing the information to the emission apparatus, the axon, which then emits to numerous receivers via the distribution apparatus, the terminal axonal arborization (DeFelipe, 2010). It took around 60 years until, with the introduction of transmission electron microscopy (TEM), the synaptic cleft was visualized (Palay and Palade, 1955) and Cajal's idea of a discontinuous nervous system had been proven.

After over a century of research, we gained immense knowledge about this system. Roles, properties and functions of different types of neurons were identified. The properties of the excitable membrane and the synapses explained how the information flowed. Individual neurons were shown to compute different aspects of the sensory input. Various implementations of neuronal network architecture were discovered. The developmental studies showed how signaling pathways shaped this architecture. Detailed studies on the dendrite revealed subcompartmentalization in the neuronal computation. The plasticity studies demonstrated some of the rules governing the dynamical changes in the system and provided insight on how memory and learning might work. Molecular biology described the rich molecular content of the neurons and how this composition gave the neurons unique abilities. On one side of the scale, we learned in great detail how the synapses work and how molecules maintain the system. On the other side, we started to describe phenomena with reference to network activity. Notwithstanding, the brain still remains to be one of the most complex systems known to humanity. Sensory perception, behavior, memory, learning, analytic thinking, emotions and consciousness emerge from interactions between individual neurons, each having their individual cellular processes.

This study attempts to contribute to the general pursuit of linking the role of individual synapses to the workings of neuronal networks. The network architecture is the defining content for the function of the brain. Information processing occurs at different levels, from single synapses to dendritic stretches, from individual neurons to microcircuits, from brain regions to the brain as a whole, with all these levels interacting with each other. Different compartments on these different levels compute individually, but interdependent on each other. Eventually their outputs are integrated to be passed onto compartments of higher level computation. Most excitatory synaptic input in vertebrate central nervous system are delivered to the postsynaptic neurons through small dendritic protrusions called spines. The spines provide the first level of compartmentalization in the network, owing to their morphological properties such as the thin spine neck (Yuste, 2011). The inputs to the spines are integrated on dendritic segments, linearly or nonlinearly, depending on the spatio-temporal structure of the input and the membrane characteristics of the dendrites (Branco and Häusser, 2010). Later, the resultant signal on the dendrites could potentially trigger an action potential and the neuron gives an output to the network.

Relating the computation in individual neurons to the network requires the information about their connectivity with each other. Different techniques are currently available to tackle the connectivity of the neuronal network, each with their unique strengths, but also weaknesses. Here, we will present our efforts to open a new niche in input mapping, aiming to complement the current research by introducing single synapse resolution, neuronal population specificity and large scale applicability.

1.1   Spines

More than 90% excitatory synapses of the pyramidal neurons are located on small membranous protrusions called spines (Harris and Kater, 1994). The synapses provide information relay sites for the neurons. Upon depolarization of the axon terminals and the boutons via action potentials (APs), the vesicles containing neurotransmitter fuse with the presynaptic membrane and release their contents

into the synaptic cleft. Neurotransmitters diffuse in the synaptic cleft and bind to the receptors on the postsynaptic side of the synapse, resulting either in opening of ion channels, or in biochemical signaling cascades if they bind to metabotropic receptors. This is called synaptic transmission and it is the major way a neuron communicates to another neuron downstream. Different types of synapses utilize different types of neurotransmitter and matching receptors, and might excite, inhibit or modulate the postsynaptic cell.

The spines were first described by Cajal, who suggested they might be key elements for the connection of the dendrites with the axons, it was Gray (1959a; 1959b) who showed that they made synapses. The spines are found in various neuronal populations in all vertebrates and some invertebrates, e.g. *Drosophila* (Leiss et al., 2009), and their densities, distributions, sizes and shapes vary in different brain regions and across species (Ballesteros-Yáñez et al., 2006; Nimchinsky et al., 2002; Sorra and Harris, 2000) (**Fig. 1.1**). Three types of spines have been described based on morphology: thin, mushroom and stubby (**Fig. 1.2**). While thin and mushroom spines have long necks, stubby spines lack any. Mushroom spines are characterized with their larger heads than of thin spines (Peters and Kaiserman-Abramof, 1970). Additionally, dendritic filopodia are transient structures, lacking a head, and are primarily found on dendrites of developing neurons. They might receive synaptic input and may further develop into dendritic spines during synaptogenesis (Fiala et al., 1998).

Molecular composition of the spines is highly complex, and many biochemical reactions related to synaptic signaling and plasticity take place within the small volume of the head. Moreover, this molecular organization is highly dynamic. The abundance of the constituent molecules can be regulated, including ion channels, or the proteins can be modified to alter their characteristics (Rochefort and Konnerth, 2012).

The spines harbor different types of glutamate receptors: N-methyl D-aspartate (NMDA), α-amino 3-hydroxy 5-methyl 4-isoxazolepropionic acid (AMPA), kainate, and metabotropic glutamate receptors. NMDA receptors (NMDARs) bind glutamate, but as well require removal of their Mg^{2+} block to be activated.
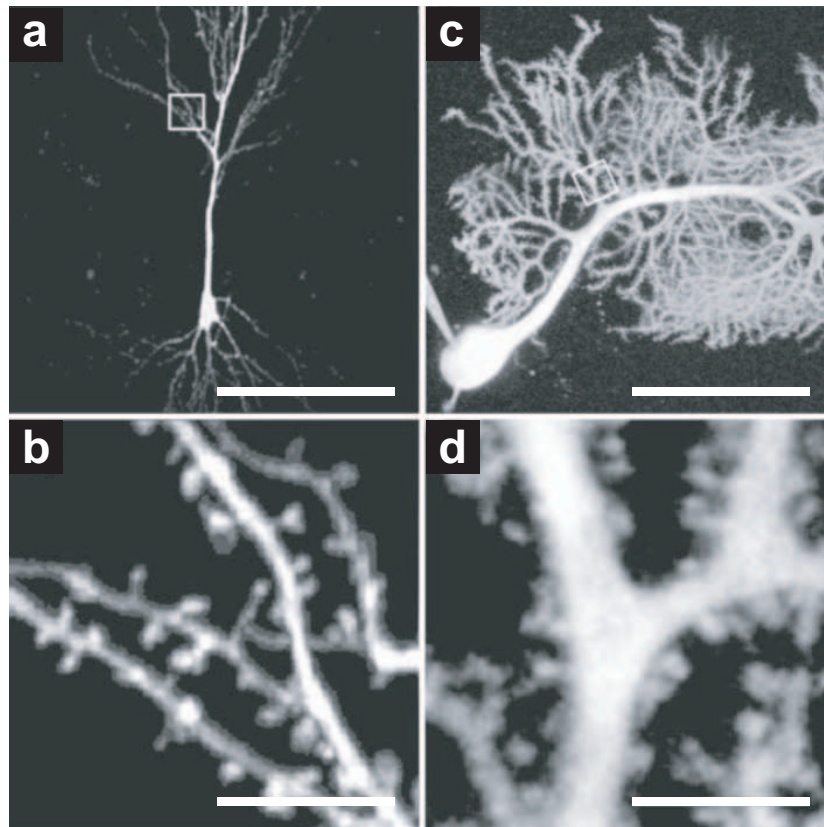
Figure 1.1: Different spines on different types of cells. (a) Spines of a hippocampal CA1 pyramidal neuron, (b) zoomed in at the box in a, and (c) of a Purkinje cell, (d) with higher magnification of the box in c. It can be observed at a first glance that the density and morphology of the spines belonging to the two distinct types of neurons show differences (scale bar: (a) 100 µm, (b) 7 µm, (c) 40 µm, (d) 5 µm). Reproduced with permission of ANNUAL REVIEWS (Nimchinsky et al., 2002).
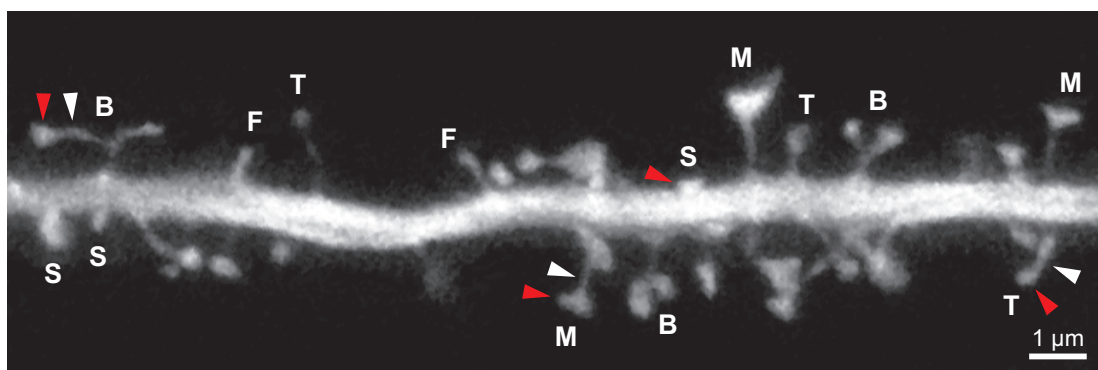
Figure 1.2: Spine types based on morphology. Different types of spines are labeled on a dendritic stretch of a hippocampal CA1 pyramidal neuron (S, stubby; M, mushroom; T, thin; B, branched; F, filopodium). The spine heads (red) and the spine necks (white) of the different spine types are marked with arrowheads. Image was taken at a custom built stimulated emission depletion laser scanning microscope. Image credit: Marcus Knopp.

This removal depends on postsynaptic depolarization, making NMDARs important for coincidence detection of pre- and postsynaptic activity in spines (Yuste and Denk, 1995). NMDARs are heteromeric tetramers and different variants show different glutamate affinity, channel kinetics and Ca^{2+} permeability depending on their subunit composition. NMDARs contribute to the spine plasticity. The spines regulate the abundance of their NMDAR (Paoletti et al., 2013). Ca^{2+} influx through NMDARs is also regulated by phosphorylation via protein kinase A (PKA) (Skeberdis et al., 2006).

Most variants of AMPA receptors (AMPARs) are not Ca^{2+} permeable, however, they could indirectly contribute to Ca^{2+} influx by aiding the removal of the Mg^{2+} block from NMDARs through depolarizing the spine head (Higley and Sabatini, 2012). Properties of AMPARs can also be dynamically regulated. It was shown that subunit composition (Liu and Cull-Candy, 2000), quantity, and/or phosphorylation state of AMPARs could be modified in relation to synaptic activity, which could be crucial for short- or long-term synaptic plasticity (Song and Huganir, 2002).

Apart from the glutamate receptors mentioned above, voltage-gated Ca^{2+} channels (VGCCs), scaffold proteins, molecules interacting with the spine cytoskeleton, signaling molecules, adhesion molecules and Ca^{2+} buffering molecules occupy the spines (reviewed in Tashiro and Yuste, 2003).

The exact function of spines is still debated. Cajal suggested that neurons might be employing them to increase the membrane area in order to pack more synapses. However, the requirement for the extra area is disputed as estimations by Harris and Stevens (1988) from electron microscopy (EM) reconstructions demonstrated in hypothetical Purkinje or hippocampal CA1 pyramidal cells which lack spines that there would still be free space on the membrane even after all of the synapses were placed. Nevertheless, spines allow dendrites and axons to arborize the neuropile with relatively straight paths while still letting them to connect with high specificity, eventually simplifying the implementation of the connectivity for the neurons (Swindale, 1981). With the aid of spines, the dendrite can reach out to axons, hence neither of the two need to make curved trajecto-

ries to contact each other. Also, with the formation or retraction of spines, the neuron can change its connectivity without the need of remodeling the whole dendritic and/or axonal structure. In addition, employing spines allows the neuron to have a greater selection of potential presynaptic partners, or in other words, more potential synapses (Stepanyants et al., 2002).

Otherwise, the primary role for spines might be for compartmentalization. The narrow spine neck constrains diffusion between the spine head and the dendrite providing compartmentalization of biochemical signals, most importantly the Ca^{2+} signals, as influx of Ca^{2+} regulates diverse processes including local biochemical signaling, protein/membrane trafficking, and synaptic plasticity (Higley and Sabatini, 2012; Sabatini et al., 2001; Zucker, 1999). Müller and Connor (1991) reported that Ca^{2+} influx through NMDARs in spines led to an increase in Ca^{2+} concentration, which was confined in the spine head. Later, Sabatini et al. (2002) showed the diffusion time constant of Ca^{2+} between the spine head and the dendrite to be in the range of 12-190 ms, up to 100 times slower than what was expected for free diffusion across a similar distance.

It is also suggested that the spine provides electrical compartmentalization. A passive electrical model for the spine stems from the assumption that spine necks have high electrical resistances. Rall (1969a; 1969b) applied the cable theory and compartmental modeling to the analysis of dendrites, which provided a theoretical basis for the interpretation of dendritic integration (Tsay and Yuste, 2004). Rall and his colleagues argued that a high neck resistance relative to the dendritic resistance would create an impedance mismatch, which would attenuate the excitatory postsynaptic potentials (EPSPs), but not the signals from dendrites invading the spines. Also, the extent of attenuation would depend on the length of the neck (Rall and Rinzel, 1973; Rinzel and Rall, 1974). Similar results were derived by Koch and Poggio (1983a; 1983b) according to their model of the spine, with a small head capacitance, a high head input resistance, a variable neck resistance and a negligible neck capacitance (**Fig. 1.3a**). Simulations on this model revealed a local amplification of the EPSPs in the spine if neck resistance was increased (**Fig. 1.3b**). This scenario had another consequence: If small
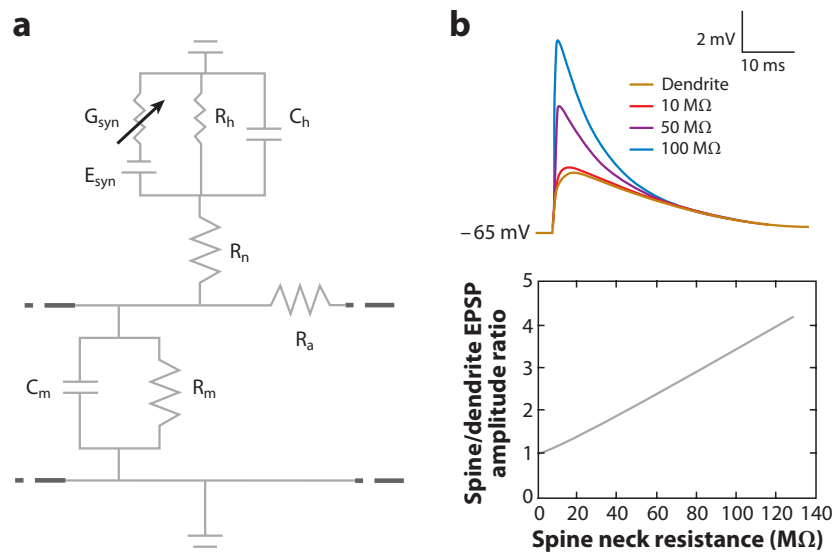
Figure 1.3: Passive electrical model of a dendritic spine. (a) The equivalent circuit of the passive spine coupled to the passive dendrite. (b) EPSP gain in relation to the spine neck resistance. Reproduced with permission of ANNUAL REVIEWS (Yuste, 2013).

synaptic conductance could lead to large changes in the ionic composition within the spine, then it would be expected that this conductivity could potentially disrupt Na^+ gradients across the spine membrane (Yuste, 2013), which could result in low-pass filtering of the synaptic inputs. From a different perspective, even if the spine neck does not have a high resistance, the additional membrane area contributed by the spines could lower the membrane resistance and increase its capacitance. Such changes in the membrane properties would still alter temporal dynamics of input integration (Jaslove, 1992).

Further possible electrical properties were attributed with the assumption that voltage-gated Na^+ and K^+ channels resided on the spines at sufficient densities (Tsay and Yuste, 2004; Yuste, 2013). Such active spines could trigger spine action potentials that might propagate to neighboring spines (Miller et al., 1985), increase reliability of dendritic integration (Segev and Rall, 1988) and implement logical operations (Shepherd and Brayton, 1987).

Imaging experiments demonstrated that spines provided biochemical compartmentalization for the synaptic input. However, justifying the electrical compartmentalization is not as straightforward, since providing evidence requires direct

electrical measurements from inside the spine head and its base on the dendrite. The exact resistance of the spine neck is still unknown to this day. Therefore, studies about electrical properties of the spines remain largely theoretical (Tsay and Yuste, 2004; Yuste, 2011). The neck resistance was measured most directly using a voltage-sensitive dye. Palmer and Stuart (2009) detected the fluorescence changes of the voltage indicator in the dendrite and in the spines during backpropagating APs and calculated the neck resistance to be up to $\sim$500 MΩ. Their simulations revealed that the resistance of this magnitude affected the amplitude of the EPSPs at the soma by less than 15%. Other indirect measurements provided approximations of the neck resistance. In a recent study with rat hippocampal CA1 pyramidal neurons, Harnett et al. (2012) calculated the neck resistance to be also $\sim$500 MΩ by assuming that Ca^{2+} influx is proportional to the local voltage. They argued that this resistance was large enough to amplify spine head depolarization and to promote nonlinear dendritic processing. Other evidence of electrical compartmentalization has been reviewed by Yuste (2013).

As mentioned above, there are multiple opinions on the function of the spines. However, there is no reason not to expect each of them being as significant as the other. The evolutionary drive for the formation of these structures might have been to acutely deal with a single challenge, and possibly response to this drive was once the sole function of the spines. It could be expected that, as the brain continued its evolution, it would have incorporated all emerging advantages of having spines into its functionality. One recent opinion proposes that the spines enable implementation of a distributed circuit with widespread connectivity, with most of the functionality introduced above contributing to the system (Yuste, 2011).

Finally, it should also be stressed, it is not only the molecular organization which is dynamic in the spines, but also, morphologically, spines are motile. They can change shape and size. Reasons for this motility are not exactly known, but it has been proposed that such changes might be altering Ca^{2+} compartmentalization characteristics of spines, serve in synaptogenesis and developmental plasticity, and/or aid connectivity (Bonhoeffer and Yuste, 2002). Furthermore,

new spines form, or existing ones retract in accordance with network activity (Hofer et al., 2009; Keck et al., 2008), providing, conjointly with single spine modifications, a basis for learning and memory (Yuste and Bonhoeffer, 2001).

1.2   Dendritic Computation

Except for some special synapses, such as the Calyx of Herd (Borst and Soria van Hoeve, 2012), it is seldom for a single synapse to drive the neuron to fire as the magnitude of the signal is small to start with and it is further attenuated while being relayed to the soma. On the other hand, the activation or the dormancy of a single synapse could determine whether or not the neuron fires (London et al., 2002). The next level of computation occurs at the dendritic segments, where signals from individual synapses are integrated. Dendrites are not just passive cables. If it were the case, they could have only linearly integrated the synaptic input and propagated it to the soma. With voltage-gated ion channels (VGICs) and cooperativity between synapses, various nonlinear computations can occupy the dendritic branches. The computation takes place in various different levels in the dendrites, from individual spines, to spine clusters, branchlets, branches and dendritic regions (**Fig. 1.4**) (Häusser and Mel, 2003).

Until the emergence of techniques, which enabled direct measurements from the dendrites, studies about the synaptic integration on dendrites were theoretical, pioneered by Wilfrid Rall. To analyze signal propagation in the dendrites, he applied William Thomson's cable theory originally developed to describe signal
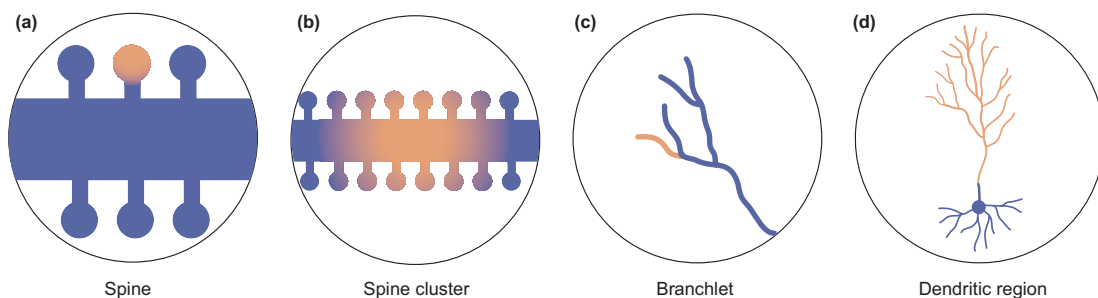
Figure 1.4: Different levels of computation in dendrites. Reprinted from Current Opinion in Neurobiology with permission from Elsevier (Häusser and Mel, 2003).

propagation through undersea telegraph lines (Gulledge et al., 2005). Models of passive dendrites predicted attenuation and temporal broadening, consequently low-pass filtering of synaptic inputs as they propagated to the soma (**Fig. 1.5**). These predictions were later experimentally verified in neocortical pyramidal neurons (Stuart and Spruston, 1998) and in hippocampal CA1 pyramidal neurons (Golding et al., 2005). Such an attenuation also suggested that distal synapses would not have be represented in the output of a neuron if no other mechanism compensated. Magee and Cook (2000) showed in hippocampal pyramidal neurons that the EPSP amplitude measured at the soma did not depend on where on the dendrite the synapse was, and that the somatic EPSP amplitude was even greater for distal synapses, suggesting a synaptic scaling mechanism. However, this mechanism was not universal, since a similar effect was not observed in neocortical layer 5 (L5) pyramidal neurons (Williams and Stuart, 2002).

The passive model of the dendrite could also predict how multiple inputs were integrated depending on their spatial and the temporal relationship. Synaptic inputs which were spatially and/or temporally close showed sublinear sigmoidal summation due to a reduction of driving force, whereas distributed inputs showed near-linear summation (Gulledge et al., 2005). These findings were as well verified experimentally (Polsky et al., 2004).

The limitation in signal propagation described for passive dendrites was addressed when dendrites were shown to harbor VGICs. Different channels were identified to contribute to active signal propagation in dendrites, specifically, voltage-gated Na^+, Ca^{2+}, and K^+ channels, hyperpolarization-activated cation channels (HCN channels) and NMDARs (Spruston, 2008), giving the dendrite nonlinear computing capabilities and enriching its potential contribution to neuronal information processing.

One important benefit of an active membrane is the facilitation of backpropagation. When a neuron fires an AP that propagates through the axon, this AP also results in a signal that, in some neurons, invades even most distal branches of the dendrites and the spines. Backpropagating APs provide retrograde signaling to the dendrite (reviewed in Stuart et al., 1997), which serves to (i) detect pre- and

postsynaptic activity coincidence, which plays a role in some forms of synaptic plasticity (e.g. Hebbian learning), (ii) influence synaptic plasticity, synaptic integration or dendritic transmitter release via induced Ca^{2+} transients, (iii) shunt out parts of the dendritic tree via activation of dendritic K^+ channels, (iv) interrupt synaptic integration by resetting the dendritic membrane potential, or (v) trigger AP bursts. Additionally, Stuart and Häusser (2001) showed a mechanism for coincidence detection in neocortical pyramidal neurons, where synchrony of an EPSP and an AP triggers additional currents facilitated by voltage-gated Na^+ channels, which results in nonlinear summation of these events (**Fig. 1.6**).

There is more to the contribution of VGICs than only enabling backpropagation. Magee and Johnston (1995) observed that synaptic events could activate VGICs in the dendrites and suggested that these channels might participate in dendritic integration, either by non-regenerative activity or by eliciting dendritic spikes.

Dendritic spike initiation usually requires a strong and synchronous input and therefore presents a form of local coincidence detection. Different patterns of synaptic activity, depending on the dendrite morphology and the VGIC distribution, produce different types of dendritic spikes with varying propagation efficiency. This determines if the spike reaches the soma with little attenuation, or stays local and does not spread far beyond the site of initiation (Häusser et al., 2000). Global spikes have been shown to facilitate distal compartments of pyramidal neurons to trigger APs, independent of other dendritic regions (Williams, 2004).

There are several reasons why spikes remain local. It may be due to structure, e.g. branching points of the dendrite progressively promote attenuation and therefore present barriers for spike propagation (Ferrante et al., 2013; Vetter et al., 2001). Or, it may be due to the physiology of the spike, e.g. NMDA spikes are constrained within the extent of the glutamergic input (Antic et al., 2010). Such local spikes result in electrical compartmentalization, yielding multiple sites of synaptic integration that can further interact with each other (**Fig 1.7**) (Häusser and Mel, 2003). Larkum et al. (2009) demonstrated in L5 pyramidal neurons how
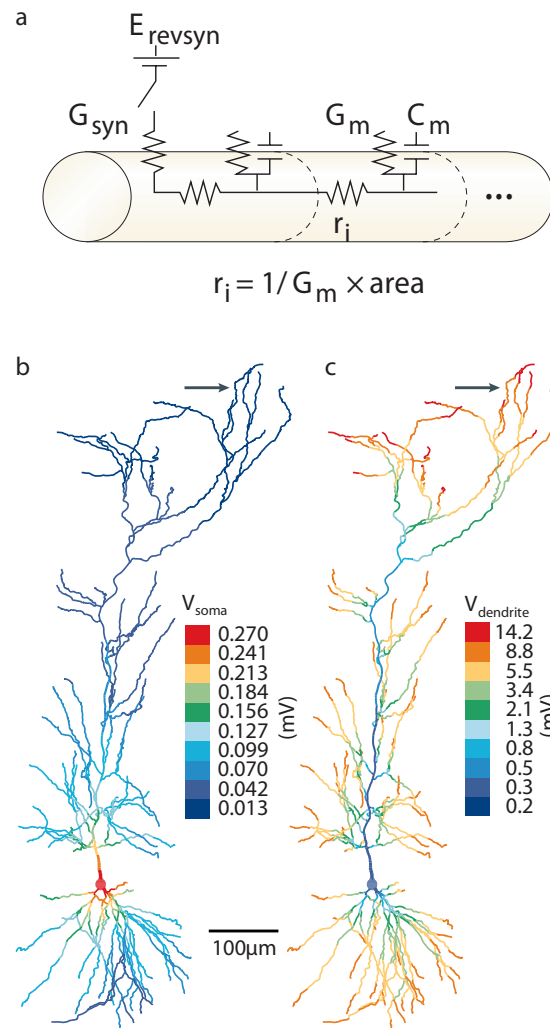
Figure 1.5: Passive dendrite model and dendritic signal attenuation. (a) The equivalent circuit diagram for the passive dendrite. (b-c) Simulation results displaying the signal attenuation as it propagates distally from the soma (b), or as it propagates to the soma (c). Reprinted by permission from Macmillan Publishers Ltd: Nature Reviews Neuroscience (Magee, 2000; Spruston, 2008).
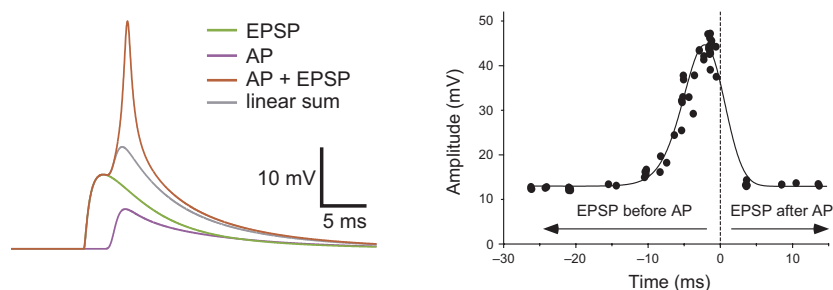
Figure 1.6: EPSP and AP coincidence. The coincidence of an AP with an EPSP results in supralinear summation (left). This summation depends on precise timing of the coincidence (right). Reprinted by permission from Macmillan Publishers Ltd: Nature Neuroscience (Stuart and Häusser, 2001).
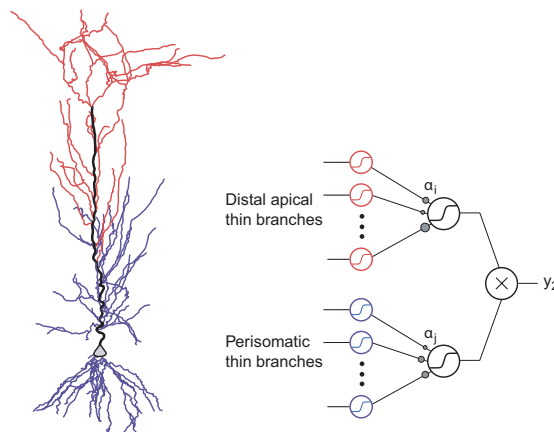
Figure 1.7: Neuron with multiple electrical compartments. Different compartments of the neuron are indicated with blue for perisomatic branches, and with red for distal apical branches (left). These compartments locally compute. Then their outputs are integrated with each other before relayed to the soma (right). Reprinted from Current Opinion in Neurobiology with permission from Elsevier (Häusser and Mel, 2003).

the different types of spikes could act together for intercompartmental communication and neuronal output generation. Their data suggested that computations were carried out locally in distal tuft and basal dendrites via NMDA spikes, which were integrated at the apical dendrite or at the soma, and relayed further via Ca^{2+} or Na^{+} spikes, respectively.

VGICs do not always function to amplify signals, but also to counteract excitability. A-type K^{+} channels and HCN channels yield non-regenerative currents in distal parts of the dendrites and further attenuate synaptic inputs, presenting compressive nonlinearities to the dendrites possibly to balance global activity (London and Häusser, 2005).

Active properties of the dendrite are determined by the composition and the distribution of VGICs. Regulation of spatial organization of the VGICs, their protein modifications, and external modulators, which alter conductivity or voltage sensitivity of these channels, provide the neuron with a higher level of adaptability, where it could be tailored to suit the needs of computation, e.g. neuronal input/output mode transitions (Magee and Johnston, 2005; Remy et al., 2010).

Various modes of dendritic integration have been described. Different studies demonstrated that hippocampal CA1 and CA2 pyramidal neurons, despite

being innervated by the same neuronal population at similar locations on their dendrites, had different integration schemes, possibly due to different branching patterns. This suggested that these different populations might be computing different aspects of similar input information (Piskorowski and Chevaleyre, 2012). Two-photon uncaging experiments provided detailed information about synaptic integration by making it possible to activate synapses with precise temporal and spatial patterns, revealing the contribution of single synapses to the compartment (Judkewitz et al., 2006).

Losonczy and Magee (2006) applied fast asynchronous input patterns via glutamate uncaging and reported the requirement of temporal coincidence and spatial closeness of synaptic activation to initiate supralinear summation and dendritic spikes in oblique dendrites of CA1 pyramidal cells. This initiation as well depended on the number of synapses that was stimulated. Later, Branco et al. (2010) could show the effect of the sequence of synaptic activation on dendritic integration, where distal to proximal synaptic activation yielded higher somatic currents in comparison to those acquired with the reversed sequence. In a similar study, Branco and Häusser (2011) explored different integration characteristics of different compartments in cortical pyramidal neurons, showing that the time window for supralinear integration was broader for distal inputs, whereas proximal inputs needed tighter temporal coincidence. Prior activity in dendrites was shown to determine the integration characteristics. In CA1 pyramidal cells, initiation of dendritic spikes depended locally on whether or not there was a previous spike, as spikes inhibit subsequent spikes through Na^+ channel inactivation. Also, in these neurons, backpropagation caused a global reduction in dendritic excitability (Remy et al., 2009).

Most of the studies on dendritic computation were done *in vitro*, and it raised the concern whether the observed mechanisms were also utilized *in vivo*. Recent publications provide *in vivo* examples from barrel cortex of behaving mice, which support nonlinear computation in dendritic compartments. Xu et al. (2012) presented evidence for utilization of nonlinear dendritic mechanisms in L5 pyramidal neurons of mice while performing an object-localization task. Authors of

the study observed that global Ca^{2+} signals were produced by plateau potentials at distal dendritic branches, which occurred during correlated vibrissal sensory input and primary motor cortex activity. This suggested a circuit-level computation implemented in these branches, which produced an object-localization signal during active touch. In a follow up study, the same authors elaborated on these nonlinearities in different compartments of L5 pyramidal neurons, describing the contribution of K^+ channels during the same object-localization task (Harnett et al., 2013). Also in barrel cortex of behaving mice, it was shown that dendrites of layer 4 (L4) spiny stellate neurons generate local and global multi-branch NMDA spikes, which preferentially amplify the preferred angular directions of whisker deflection, whereby contributing to the angular tuning of these neurons (Lavzin et al., 2012).

So far the focus has been directed to the "receptor apparatus" role of the dendrite in the neuron doctrine, but the beautiful complexity of its computational capabilities has been revealed not to be only limited to input processing. Dendrites were observed in releasing neurotransmitters, such as glutamate and γ-aminobutyric acid (GABA) (Ludwig and Pittman, 2003), or neuromodulators (Regehr et al., 2009), usually in retrograde signaling. It was shown in A17 amacrine cells in the retina that neurotransmitter release could be very local, allowing more than 100 independent parallel processes in a single neuron, each independently providing feedback inhibition to different presynaptic bipolar cells (Grimes et al., 2010).

To sum up, electrical integration mechanisms of the dendrite, plasticity of dendritic segments, and local neurotransmitter release challenge the idea that neuron is the most elemental circuit component in the vertebrate brain (**Fig. 1.8**). Compartments of dendrites perform their independent computation and share their output with other compartments. They can trigger global dendritic spikes and yield enough depolarization at the soma to elicit APs, which allows them to dictate the output of the neuron and pass the outcome of their computation to the postsynaptic neurons independently. In some circuits, they communicate directly with the presynaptic neuronal population via local neurotransmitter re-
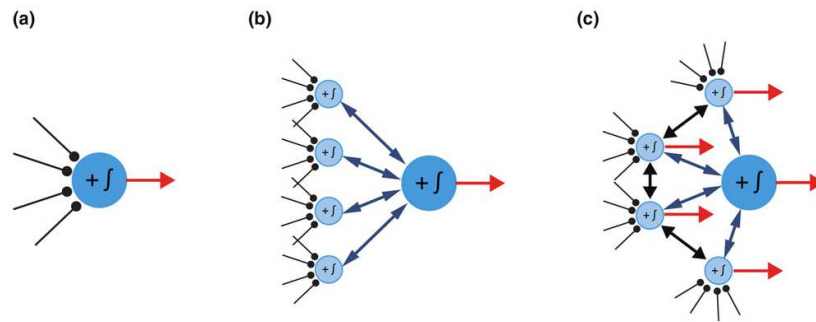
Figure 1.8: Parallel processing in the dendrite. (a) In the simplest model, inputs are linearly integrated at the soma. (b) Dendritic compartmentalization provides local integration in compartments before being integrated and relayed to the soma. (c) Via local dendritic transmitter release, compartments can give output independently. Reprinted from Current Opinion in Neurobiology with permission from Elsevier (Branco and Häusser, 2010).

lease. Therefore, these compartments are, at least in some networks, individual, independent components of the circuit.

1.3 Pursuit of Connectomes

The typical neuron in the brain receives thousands of inputs, but it has only one axon to give output to. Therefore, the dendrite essentially needs to be able to transform the wide input space to a narrow output space, at times by discarding irrelevant inputs (London and Häusser, 2005). As was discussed, the dendrite applies this transformation by exploiting local nonlinear mechanisms. Poirazi and Mel (2001) presented a theoretical work, where they compared the information storage capacity of linear and nonlinear modes of dendritic integration, and showed that the neuron gains around 50 times more capacity by utilizing local nonlinear processes. They pointed out that achieving this gain required correct addressing of relevant presynaptic contacts onto relevant postsynaptic compartments, since the effectiveness of a synapse is modulated by the neighboring synapse activity within the same compartment for nonlinear integration.

Behavior emerges from the activity of an ensemble of neurons in the brain, connected to one another with a specific architecture. The presynaptic neuronal population defines the content of the information transmitted to and processed by the postsynaptic cell. The computational outcome of this presynaptic information

depends on where and how it is delivered to the postsynaptic neuron. For these reasons, efforts have been undertaken to map the connectivity between different populations of neurons within networks of differing sizes and complexities.

Different methods have unique strengths and weaknesses. The ultimate brain map should consist of all neurons with complete morphology, at a resolution that resolves all of their connections. These connections should be complemented with additional information, such as their function, synaptic strength, and receptor composition. The location of the connections should be described with their environment, that is, with a detailed molecular map of their membranes, with all ion channels and receptors captured with their sensitivity and conductivity states, and perhaps even including molecular and ionic composition of individual compartments. Moreover, neurons are not the only family of cells in the brain, but their proper working depends on their interaction with other cell types in the tissue, such as the glia cells. Therefore, the ultimate map of the brain cannot only be constrained to the neurons and should include all cells which interact with the network. However, this map could only be a snapshot, trying to explain a system that changes every instant. Whether or not we would be able to reach this ultimate map, or if we need such a detailed picture to understand the brain, or if this detailed picture could be sufficient for an explanation shall be left for time to show. Current studies have already contributed to our knowledge immensely:

Multiple simultaneous intracellular recordings can be used to probe microcircuit connectivity. Multi-patch based methods elicit APs on one of the neurons and measure the synaptic response on the others. Connectivity information is usually based on statistics; random sets of neurons from defined populations are patched, and the connectivity is probed. Recording from enough number of sets gives a percentile of the presynaptic population that makes their connections with the postsynaptic population. This percentile can then be translated to relative connection weights. Using dual and triple intracellular recordings, Thomson et al. (2002) mapped the microcircuitry of rat and cat neocortex, including excitatory and inhibitory neurons from all layers of the cortex. Kampa et al. (2006) used recordings from triplets of rat layer 2/3 (L2/3) and L5 cortical pyramidal neurons

and could show that specific L5 subnetworks receive inputs from different L2/3 subnetworks. Brown and Hestrin (2009) recorded simultaneously from up to four L5 pyramidal neurons from subpopulations with specific long range targets and investigated their local intracortical connections in relation to their long range connectivity. Such approaches show the general architecture of the circuitry, however, although connections are detected, it is not possible to know their exact locations on dendrites.

Using light microscopy based cytomorphology to infer connectivity information extends back to Cajal, where axonal and dendritic arborizations of labeled neuron populations are cross-correlated and the circuitry is mapped with the approximation that the size of axodendritic overlap correlates with the number of connections. This approximation has been used by Peters (Peters and Feldman, 1976; Peters and Payne, 1993), and currently is referred to as Peters' rule. In the last decade, Binzegger et al. (2004) provided a quantitative map of the cat primary visual cortex (V1) circuit based on this principle. In addition to being an approximation, this approach also did not provide any spatial information about the synapses. An improvement to this technique was possible by locating potential synapses according to the proximity between the dendrite and the axon (Stepanyants and Chklovskii, 2005). This concept has been used by Shepherd et al. (2005) together with laser scanning photostimulation (ultraviolet (UV) glutamate uncaging) to demonstrate that the functional circuits in barrel cortex could be predicted from morphology. However, the location of the synapses still remained an approximation.

Connectivity maps at synaptic resolution can be acquired by EM methods. With recent advances in sample handling, such as in serial block face scanning electron microscopy (SBSEM) (Denk and Horstmann, 2004), difficulties in the alignment of subsequent sections and the automation of data acquisition were further improved, hence allowing large scale, high throughput and high resolution imaging of neuronal structures to obtain very detailed synaptomes. SBSEM has also been used in combination with two-photon calcium imaging. The connectivity of the neurons which were identified by Ca^{2+} imaging according to the

direction preference in the mouse retina (Briggman et al., 2011), or to the orientation preference in the mouse V1 (Bock et al., 2011) was subsequently mapped at a high resolution with SBSEM. Array tomography combined immunohistochemisty of very thin sections with EM, providing the molecular architecture of the neurons in addition to the connectivity maps at synaptic resolution (Micheva and Smith, 2007). Unfortunately, the analysis of these data will remain hard and tedious work, especially for large volumes of tissue, until a reliable, fully automated reconstruction algorithm is discovered. Additionally, the volume of the the tissue that is mapped is still limited and prevents EM based methods to map long range connections.

Recently, the GFP reconstitution across synaptic partners (GRASP) technique (Feinberg et al., 2008) has been adapted to be used with mammalian tissue, called mammalian GRASP (mGRASP) (Kim et al., 2012). In mGRASP, two non-fluorescent fragments of split green fluorescent protein (GFP) are expressed on pre- and postsynaptic neuron populations, respectively, and at the synapses the fragments can reconstitute, granted by the close separation in the synaptic cleft. The reconstitution restores the fluorescence of the GFP and the fluorescent puncta pinpoint location of potential synapses. This method provides maps at synaptic resolution with the ease and speed of light microscopy. A raising concern is whether neurite touches could also be facilitating reconstitution, leading to false positives. As addressed by the authors, this did not seem to be an issue. Additional affinity coming from reconstituted GFP could have also induced formation of synapses, but an increase in the number of synapses was not observed in comparison to nontransduced neurons. The great advantage aside, the functionality of the synapses is not assessed, however it potentially could be if supplemented with imaging data for synaptic transmission.

Strategies that stimulate presynaptic neurons and measure responses on the postsynaptic neurons by Ca^{2+} imaging or by electrophysiology can yield functional maps. Richardson et al. (2009) mapped thalamic and intracortical inputs to L4 auditory cortex neurons by electrically stimulating presynaptic areas and identified functional synapses via two-photon imaging of postsynaptic calcium

signals. Since stimulation was delivered electrically, the stimulated presynaptic population was local, but not targeted specifically. Matsuzaki et al. (2011) stimulated individual presynaptic neurons via two-photon glutamate uncaging and were able to locate functional synapses via calcium imaging. Stimulated cells were selected manually, therefore this method addressed the specificity of presynaptic neuronal population. However, restriction of the stimulation to individual cells and a limited field of view prevented this method from being suitable for larger scale mapping. Similarly, Nikolenko et al. (2007) stimulated presynaptic cells via two-photon glutamate uncaging and located postsynaptic partners via two-photon Ca^{2+} imaging at cellular resolution. Petreanu et al. (2007; 2009) used light activated cation channel channelrhodopsin-2 (ChR2) for presynaptic stimulation and measured light evoked postsynaptic potentials. With this method, they could target presynaptic neurons selectively with genetic tools and probe the connectivity between neuronal populations at a subcellular resolution, however, they did not resolve single synapses as the connectivity information was based on the readout of postsynaptic electrical currents. Little and Carter (2012) stimulated presynaptic neurons also with ChR2, and resolved and identified individual inputs by two-photon calcium imaging, which, as will be discussed later, is also the method of choice for this study. They did not, however, systematically scan dendritic branches and therefore did not provide any input maps.

1.4   The Basic Organization of Cortex

The cortex occupies a large portion of vertebrate brains and its complex circuitry, along with its flexibility in rewiring, gives the organisms a large variety of behavioral and perceptual abilities (Douglas and Martin, 2007a). It has a laminar six-layered organization, where neurons both excitatory and inhibitory interact with each other, with intra- and interlayer connections, as well as with long range connections to other microcircuits in the same region, or in different brain regions, ipsi- or contralaterally. The six-layered architecture is preserved across mammalian species, however with structural differences, such as different relative thickness and neuron density at different layers (DeFelipe et al., 2002).

Developed by work of Mountcastle (1957) in cat somatosensory cortex and Hubel and Wiesel (1963) in cat visual cortex, it is hypothesized that the cortex has a columnar organization in some species. It is also hypothesized that this columnar organization enabled cortex to expand laterally, unit by unit, in the course of evolution as it got more complex and capable (Buxhoeveden and Casanova, 2002; DeFelipe et al., 2002; Mountcastle, 1997).

The most extensive intracortical circuit mapping was done by Binzegger et al. (2004) in cat V1 (**Fig. 1.9**). They compared the dentritic and axonal arbors of excitatory and inhibitory neurons from different layers of the cortex. The extent of the axodendritic overlap between two neurons approximated the relative connectivity. This way, they could show, for instance, L2/3 neurons made most of their connections within the layer, which accounted for most of the intracortical connections, whereas L5 received most of its input from L2/3 and in comparison did not make as many contacts within the layer. They also showed that thalamic inputs innervated mostly L4 and made up a small fraction of all the connections in the cortex. This suggested an architecture based on recurrent neuronal circuits in the cortex, with feedforward excitatory and feedback inhibitory connections, computing locally as microcircuits (Douglas and Martin, 2007b). Prevalence of local connectivity, a columnar organization, and the general homogeneity of the cytoarchitecture throughout the cortex led to the pursuit of a canonical circuit (Douglas et al., 1989).

Some other studies revealed the existence of specific subnetworks within the cortical network, such as the study by Yoshimura et al. (2005). By cross-correlating evoked excitatory postsynaptic currents (EPSCs) and inhibitory postsynaptic currents (IPSCs) in simultaneously recorded adjacent L2/3 neurons upon photostimulating L4 or L5, they showed that there were finer subnetworks within functional columns. Separate subpopulations of L2/3 neurons received input from specific presynaptic subpopulations in L4, whereas inhibitory neurons and L5 pyramidal neurons gave output to L2/3 disregarding subpopulations.

The attempts to discover the connectivity in the cortex are not limited to the studies mentioned above. However, the cortex is a very complex network.

Therefore, novel high-throughput methods that can provide high resolution data are necessary to eventually figure out how it functions.

1.5   Objective of This Study

In this study, a new technique is developed and applied for neuronal circuit mapping at single synapse resolution. As discussed, there are several gaps in the data acquired by current methods. Some methods are not able to provide neuronal population specificity. The techniques that address the population specificity either do not have the synaptic resolution, or when they do, the technique is not applicable for large scale mapping. mGRASP cannot provide the information whether the detected puncta are functional synapses or not. EM based methods can supply very high resolution information at the expense of difficult and time consuming analysis. Additionally, they are currently only suitable for inves-
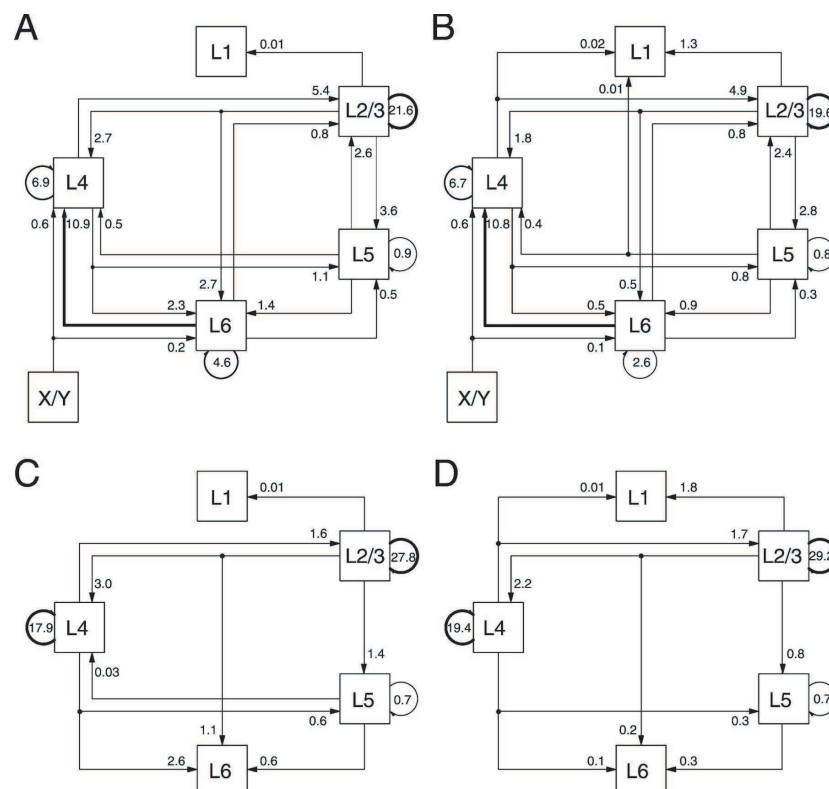
Figure 1.9: Microcircuitry of cat V1. (a) between excitatory neurons, (b) from excitatory onto inhibitory neurons, (c) from inhibitory onto excitatory neurons, and (d) between inhibitory neurons. Reproduced with permission of SOCIETY FOR NEUROSCIENCE (Binzegger et al., 2004).

tigating local connectivity. Here, this new approach addresses these issues and provides a new level of information to complement existing methods.

Shortly, we genetically target specific presynaptic neuronal populations to express ChR2 (Nagel et al., 2003), and induce activity only in these subpopulations via light stimulation (Boyden et al., 2005). Simultaneously, in a postsynaptic neuron filled with a volume marker and a calcium indicator, NMDAR mediated Ca^{2+} influx is detected in individual spines upon successful synaptic transmission from the presynaptic population (similarly as done by Zhang and Oertner, 2007). This technique adds to current mapping efforts by specific presynaptic population targeting and single synapse resolution in a single experiment. Specific presynaptic targeting also allows to acquire large scale maps since the connectivity of the whole population is mapped onto postsynaptic cells, rather than of individual presynaptic neurons.

We apply this technique to probe L5 to L5, and L2/3 to L5 excitatory connectivity in the mouse V1, specifically to scan basal dendritic branches of postsynaptic L5 neurons and map their functional synapses with the presynaptic population. Later, the spatial organization of the detected inputs are analyzed.

We chose L5 and L2/3 as the presynaptic population for practical purposes. Thy1-ChR2 transgenic mice (Section 2.5) express ChR2 in L5, and it is possible to target L2/3 for expression by *in utero* electroporation (Section 2.6).

L5 neurons were interesting to investigate as the postsynaptic neuronal population. They are the major cortical output, and therefore represent the final stage of computation in cortical circuits (Harnett et al., 2013). Moreover, L5 neurons exhibit different subpopulations within the same circuit depending on their target regions. These subpopulations have distinct morphology, membrane properties and firing characteristics, therefore, potentially compute specific output for their target regions (Hattox and Nelson, 2007; Kasper et al., 1994). Altogether, L5 is a great model to study dendritic computation in the microcircuitry.

Chapter 2

Methods

2.1 ChR2 Assisted Synapse Identity Mapping

2.1.1 Optogenetic Stimulation

ChR2 is a light gated cation channel isolated from green alga *Chlamydomonas reinhardtii.* Originally, Nagel et al. (2003) showed that mammalian systems, such as the HEK293 and BHK cell lines, could also express the functional channel and they could be depolarized via the light induced ionic currents. Later, this light induced depolarization was demonstrated to be large enough to elicit photostimulus locked APs in hippocampal neurons with millisecond time resolution (Boyden et al., 2005). This provided a powerful tool for neuroscience research. Its strength lies with the possibility to target specific neuronal populations genetically for expression, which enables selective and noninvasive stimulation of these populations with light. This is particularly important in *in vivo* studies and in studies where stimulation of specific neuronal populations is required. Over the past years, new variants of ChR2 or similar proteins were engineered to give a selection of conductivity, kinetics and excitation wavelengths (Berndt et al., 2011; Kleinlogel et al., 2011; Lin et al., 2009; Prigge et al., 2012). Additionally, halorhodopsin, a light activated Cl⁻ pump, complements ChR2 with an inhibiting function (Han and Boyden, 2007).

Optogenetic stimulation is an important tool not only for basic research, but also in medicine with a wide potential application pool, including blindness, Parkinson's disease, epilepsy, addiction, neuropsychiatric diseases, etc. (Cao et al., 2011; Kokaia et al., 2013; Zhang et al., 2007a).

2.1.2 Two-Photon Calcium Imaging

In single photon fluorescence, a fluorophore absorbs one photon of sufficient energy and subsequently enters an excited state. If its relaxation proceeds through radiative transitions, it emits a photon with lower energy, accounting for non-radiative energy losses. It is also possible to excite a fluorophore with multiple photons, when a single photon cannot provide the adequate energy for excitation. This requires these photons to be absorbed simultaneously and their summed energy to fit the energy gap for excitation. Emission happens as in single photon fluorescence. Occurrence of multi-photon absorption is a very rare event, and can happen only when the photon density is very high.

This phenomenon has been applied to microscopy, most commonly with two-photon fluorescence, where only fluorophores in very close vicinity to the focal point of the objective lens receive enough light intensity to absorb two photons and fluoresce, giving the technique an intrinsic 3D resolution (**Fig. 2.1**) (Zipfel et al., 2003). This excitation volume is scanned over the tissue to acquire an image (Denk et al., 1990). Typically near infrared light is used for excitation, which has deeper tissue penetration in comparison to lower wavelengths. The diffraction-limited focal volume (the resolution) depends on the excitation wavelength, the numerical aperture and the filling of the back aperture of the objective lens (Zipfel et al., 2003). The intrinsic 3D resolution makes its implementation relatively easy when compared to other tomographic microscopy techniques. However, the requirement of powerful femtosecond lasers makes it also an expensive technique (Denk and Svoboda, 1997; Svoboda and Yasuda, 2006).

This technique can in principle be used to image any fluorophore, synthetic or genetically encoded. By using a Ca^{2+} indicator that changes its fluorescence characteristics depending on whether Ca^{2+} is bound or not, it has been possible to make quantitative measurements of intracellular Ca^{2+} concentrations (Denk et al., 1996). This has been used with two-photon microscopy to measure Ca^{2+} dynamics in spines (Denk et al., 1995; Yuste and Denk, 1995).
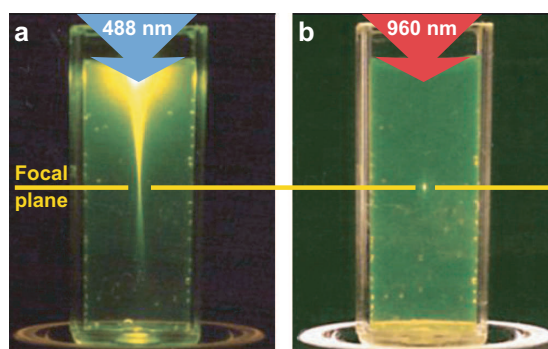
Figure 2.1: Single photon vs. two photon excitation volume. Single photon excitation (a), and two-photon excitation (b) of fluorescein. The excitation volume is localized in the focal plane with two-photon excitation, whereas single photon excitation occurs at all locations on the path of the excitation beam. Reprinted by permission from Macmillan Publishers Ltd: Nature Biotechnology (Zipfel et al., 2003).

2.1.3 Mapping of Synaptic Inputs

In this study, optogenetic stimulation was combined with two-photon calcium imaging to map functional synapses between presynaptic and postsynaptic populations (**Fig. 2.2**). Presynaptic neurons expressing ChR2 from acute brain slices were stimulated with blue light. Ca^{2+} influx into postsynaptic spines upon synaptic transmission was detected via two-photon imaging of Fluo-5F (Zhang and Oertner, 2007). Experiments were done in the presence of NBQX to block AMPARs. NMDAR currents were promoted by depolarizing postsynaptic neurons to remove the Mg^{2+} block from the channels and by including D-serine. Hence, glutamergic synaptic transmission in the slice was restricted to NMDAR of the patched neuron, allowing to map only direct inputs while preventing polysynaptic transmission. Picrotoxin blocked $GABA_A$ receptor chloride channels to avoid possible inhibition.

2.2 Experimental Setup

Imaging was done with a custom built two-photon laser-scanning microscope (**Fig. 2.3**). Two femtosecond, 80 MHz pulsed Ti:sapphire lasers (Mai Tai and Millenia-Tsunami) were tuned to different wavelengths (960 and 810 nm, respectively). The intensity of the beams could be tuned with electro-optic modulators in the beam path. Polarization of the beams was adjusted to be perpendicular
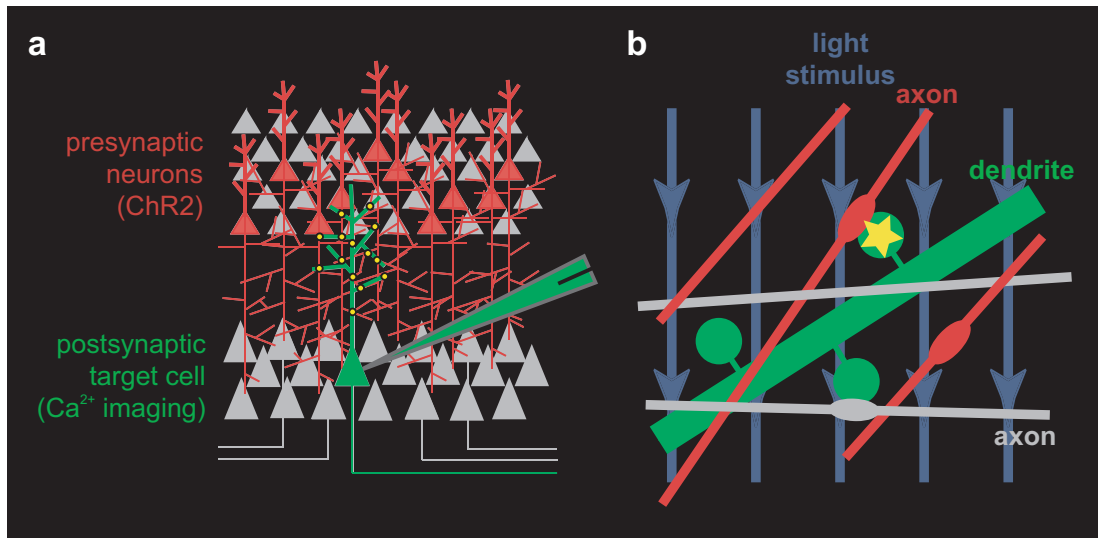
Figure 2.2: ChR2 assisted synapse identity mapping. (a) Presynaptic neuron population (red) is targeted genetically to express ChR2. A postsynaptic target cell (green) is patched and filled with a volume dye and a Ca^{2+} indicator. (b) Upon light stimulation, activity is evoked in transfected presynaptic neurons (red). At an input site between a transfected cell and the patched postsynaptic cell (green), calcium signals could be detected (yellow star) upon successful synaptic transmission. The contact site of an untransfected presynaptic cell (gray) remains dark. Illustration credit: Dr. Volker Scheuss.

to each other using a half-wave plate and subsequently the beams were combined via a polarizing beam splitter.

The combined beam was imaged onto a galvanometric scanner through two telescope lenses. After the scan-head, the deflected beam was collected with a scan lens and collimated with the tube lens to partially overfill the back aperture of the objective lens. A 470 nm light emitting diode (LED) was coupled to the beam path after the galvanometric scanner at the dichroic mirror unit of a commercial microscope body. The LED was focused at the back focal plane of the objective lens using the collector lens installed on the unit and the tube lens of the microscope body, in the epifluorescene path, to uniformly illuminate the object plane. Trans-fluorescence was collected and separated to red and green channels with a dichroic mirror and detected with shutter protected photomultiplier tubes (PMTs). Shutter protection was necessary since it was not possible to completely block the blue stimulation light with filters, and the stray light was strong enough to damage the PMTs. The PMT signals were preamplified and fed into to the

acquisition board.

The pipette holders were controlled with micromanipulators. The microscope stage was driven by stepping motors also controlled by the micromanipulator controller. Slices were visualized for patching by infrared Dodt gradient contrast video microscopy (Dodt and Zieglgänsberger, 1994). Electrical activity of the cells was recorded (see Section 2.4) with an Axon MultiClamp system. During the experiments, Labview and Matlab based custom software was used for setup control and data acquisition.

2.3   Experimental Procedures

Acute slices from 40-55 days old mice were used to map inputs to postsynaptic L5 pyramidal neurons. Slices were acquired either from Thy1-ChR2 transgenic line (Thy1-ChR2) mice for L5 presynaptic targeting, or from electroporated mice
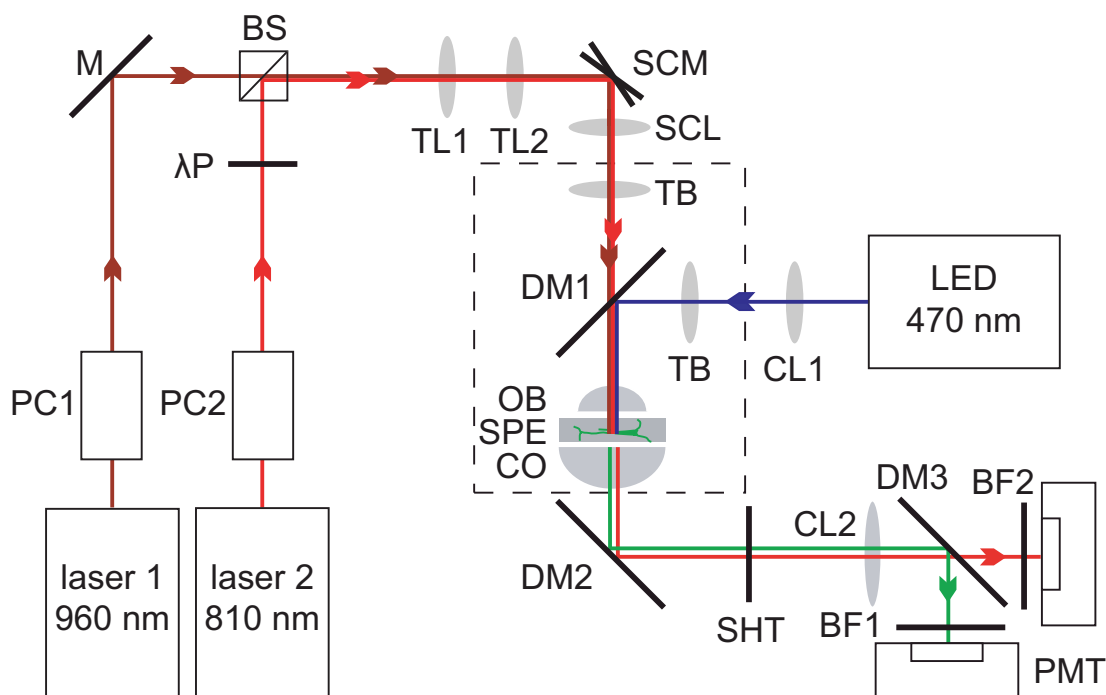
Figure 2.3: The setup light path. Refer to the text for the details. PC1 and PC2, electro-optic modulators; λP, half-wave plate; M, silver mirror; BS, polarizing beam splitter; TL1 and TL2, telescope lenses; SCM, galvanometric scanner; SCL, scan lens; TBs, tube lenses; DM1, DM2 and DM3, dichroic mirrors; CL1 and CL2, collector lenses; OB, objective lens; SPE, specimen; CO, condenser; SHT, shutter; BF1 and BF2, band-pass filters; and PMT, photomultiplier tube. Dashed rectangle encloses the microscope body. Illustration credit: Dr. Volker Scheuss.

for L2/3 presynaptic targeting. Postsynaptic L5 cells were visually identified and patched. They were kept at resting potential in voltage clamp mode and filled with 30 µM Alexa 594 fluorophore and 1 mM Fluo-5F calcium indicator at room temperature in artificial cerebrospinal fluid (ACSF) containing 10 µM NBQX, 50 µM picrotoxin, and 10 µM D-serine (experimental ACSF). The cells were filled minimum for 10 minutes before they were depolarized to NMDAR reversal potential+10 mV to remove the Mg^{2+} block. Prior to the experiments, imaging laser powers were calibrated. Experiments were conducted using a Labview based custom imaging software (Colibri), forked from the original imaging software by BioImaging Zentrum, Ludwig-Maximilians-Universität München. The acute slices were imaged at 810 nm excitation for the synthetic fluorophores (Alexa 594, Fluo-5F), and 960 nm excitation for the fluorescent proteins (enhanced YFP (EYFP), mCherry).

Mapping experiments were conducted by imaging single z-planes of dendritic segments in 5×19.8 µm tiles at 100 nm xy-sampling with a frame rate of 10 Hz. During each time series, Alexa 594 and Fluo-5F fluorescence were acquired before and after the photostimulation (470 nm LED). In Thy1-ChR2 mice, the photo-stimulus consisted of 3×2 ms pulses at 30 Hz with 4 mW power at objective lens back-aperture, and was delivered to the slice with an open field aperture. In electroporated mice, it consisted of 3×5 ms pulses at 30 Hz with 500 µW power, and was delivered with a closed field aperture (diameter ∼80 µm at the object plane).

In each acquisition, first, one blank frame was recorded to measure the electrical offset of the system. The blank frame was followed by five baseline frames. After the baseline frames, the shutter protecting the PMTs was closed for two frames and the photostimulus was delivered to the slice. Right after shutter opening, 42 poststimulus frames were acquired. In total, 50 frames were collected in 5 s. Postsynaptic electrical currents were also recorded.

At every location, multiple z-planes were imaged to be able to cover every spine. Each spine had minimum three measurements. At least 10 s passed between subsequent acquisitions. Once all the spines in multiple z-planes at a

certain tile location were imaged, a morphological z-stack was taken at 50 nm xy-sampling and with 1 μm increments in z-dimension. Afterwards, the tile was moved to a new location to continue with mapping. Dendritic branches were systematically scanned with overlapping tiles.

To be able to fit the spines and the dendritic segment optimally in the field of view, rotation of the imaging tile was adjusted. Experiments ended when the cells exhibited unrecoverable internal Ca^{2+} increase, widespread blebbing, or when the patch was lost. At the end of the experiments, low resolution, low magnification images documented the location of the cells.

2.4   Electrophysiology

Whole Cell Voltage Clamp Recordings

In mapping experiments the cells were clamped (Blanton et al., 1989; Edwards et al., 1989; Hamill et al., 1981) to NMDAR reversal potential+10 mV and meanwhile loaded with Fluo-5F calcium indicator and Alexa 594 fluorophore. The primary function for voltage clamp was to remove the Mg^{2+} block from NMDARs. Since this removal was in steady state, no compensation was made for access resistance or cell capacitance. The cells were patched using pipettes (from thin walled glass capillaries) with 3-5 MΩ resistance, and filled with Cs-based internal solution (recipe in Appendix B). Target access resistance was 20 MΩ. Lower access resistances caused cellular wash-out and blebbing, whereas higher resistances hindered loading of dyes. Cells were let for filling at the resting potential for at least 10 min before starting the experiments. NMDAR reversal was measured prior to each experiment to exclude the variations due to junction potentials (Barry and Lynch, 1991). This was done by photostimulating the slice and adjusting the holding potential until no current was observed.

Whole Cell Current Clamp Recordings

In experiments for somatic and axonal photostimulation response characterization, the membrane potential of the cells was recorded in current clamp mode (Blanton et al., 1989; Edwards et al., 1989) without any current injection. Bridge

resistance and pipette capacitance were compensated. Cells were patched using pipettes (from thin walled glass capillaries) with 3-5 MΩ resistance, and filled with K-based internal solution (recipe in Appendix B). In these experiments, experimental ACSF also contained 10 μM CPP to isolate the effect of ChR2 currents.

Cell Attached Recordings

To obtain ChR2 dose-response characteristics, spiking in the cells was measured by cell attached current recordings (Margrie et al., 2002), not to interfere with the membrane potential and change spiking properties. For this procedure, pipettes (from thin walled glass capillaries) with 3-5 MΩ resistance , filled with "loose-seal" internal solution (recipe in Appendix B) (Sato et al., 2007) were used. A seal resistance of ∼30 MΩ gave the best signal-to-noise ratio. In these experiments, experimental ACSF contained also 10 μM CPP to isolate the effect of ChR2 currents.

To verify the specificity of light evoked presynaptic activity, spikes of the cells in different layers of V1 were measured upon light stimulation. In these experiments, the ACSF solution used was identical to the one in the mapping experiments.

2.5 Transgenic Line Thy1-Chr2

Thy1-ChR2 (line-18) mice (Wang et al., 2007) were bred and used for experiments where presynaptic L5 pyramidal neurons expressed wildtype ChR2 (wtChR2). In the experiments, 40-55 days old mice were used. The lower boundary was selected based on the end of critical period for V1 (∼postnatal day 30, see Huang et al., 1999), when the cortical network could be considered mature. The upper boundary was selected to give a convenient time window for experiments, meanwhile considering the negative effect of age on the preparation quality.

2.6 *In Utero* Electroporation

Application of electrical pulses permeabilizes cell membranes and allows hydrophilic molecules to enter cells. This is commonly known as electroporation, named based on the hypothesis that electrical fields create pores in membranes by means of increasing surface tension. Although the exact mechanism is not yet understood, the technique has been widely employed to load cells with DNA, drugs, dyes, or alike (Rols, 2008).

An *in vivo* application of electroporation, *in utero* electroporation (IUE), was first introduced by Saito and Nakatsuji (2001), where a solution containing the plasmid/s is injected into the ventricles of fetuses, and cells at the lining of the ventricles are transfected by the application of an electrical field. By performing the procedure at different developmental stages of the cortex and adjusting the orientation of the electrical field, it is possible to target gene expression to different regions and layers of the cortex. In this project, the protocol by Harvey et al. (2009) was primarily followed. Wild type C57BL/6 pregnant females on fifteenth day after plug check, were used to target L2/3 of the V1. Good aseptic technique and proper animal handling were followed at every stage of the procedure. The surgeries were performed in compliance with the institutional guidelines of the Max-Planck-Gesellschaft and the local government (Regierung von Oberbayern) under the license number 55.2-1-54-2531-54-09.

Preparation

The operating bench and the heating pad were thoroughly wiped and disinfected with 80% ethanol solution. All metal instruments were sterilized with a glass bead sterilizer at 275°C. The rest of the tools were soaked in 80% ethanol for disinfection. Most consumables were purchased in sterile packages.

The bench and the heating pad were covered with a sterile surgical drape. A well soaking and thin multipurpose tissue was placed over the heating pad to provide dryness during operation. Prior to the start of a surgery, all materials were placed on the drape (**Fig. 2.4**, a complete list is found in Appendix B). 50 ml of sterile 0.9% (w/v) saline was heated to 35°C on a heatblock to be used

for flushing and moistening during the surgery. The saline solution was applied with sterile plastic Pasteur pipettes. The heating pad was prewarmed to 37°C.

DNA solution contained 10 mM Tris-HCl pH 7.4, 0.02% (w/v) Fast Green dye, 2.0 mg/ml pCAGGS - hChR2(H134R) - EYPF - WPRE plasmid, and 0.5 mg/ml pCAGGS - mCherry - WPRE plasmid (see Section 2.7). The total DNA concentration should not be below 2.0 mg/ml if high transfection rates are desired, and should not be higher than 4.0 mg/ml, since it might cause toxicity and does not contribute to a higher transfection. When cotransfecting multiple plasmids, the ratio of plasmids should be optimized to provide the desired levels of expression for each plasmid.

The DNA solution was filtered through an Ultrafree-MC centrifugal filter unit with 0.22 μm pore size. Filtration is essential, because small particles present in the DNA solution might block the ventricular ducts and cause hydrocephalus. Injection pipettes were pulled in a single step from thick wall glass capillaries with a vertical puller, and the tips were broken under a microscope to have an opening diameter of 50-100 μm and ideally a 45° bevel angle. A suitable pipette will pierce through the embryo skull smoothly without any effort. If the tips break or need too much force to penetrate, better pipettes should be prepared. One should always have extra pipettes nearby.

The pipettes were loaded with 20 μl of DNA solution. Injections were done with a picospritzer, which was driven by a Master-8 pulse stimulator. The pressure of the picospritzer was set to 18 psi. The injection volume per trigger was adjusted to 1 μl by changing the number of pulses in the 100 Hz train (single pulse width, 5 ms). Typically, depending on the tip diameter of the pipette, 10-30 pulses were sent to the picospritzer. The exact number of pulses was calibrated by comparing the size of ejected droplets from the pipette to 1 μl measured droplets.

The electroporator was set to five pulses of 50 ms width at 1 Hz with an amplitude of 30 V. More pulses and higher voltages might be used for denser transfection at an expense of a lowered survival rate (Saito and Nakatsuji, 2001). These should be optimized individually depending on requirements.

C57BL/6 mice with previous pregnancy experience and in their fifteenth day
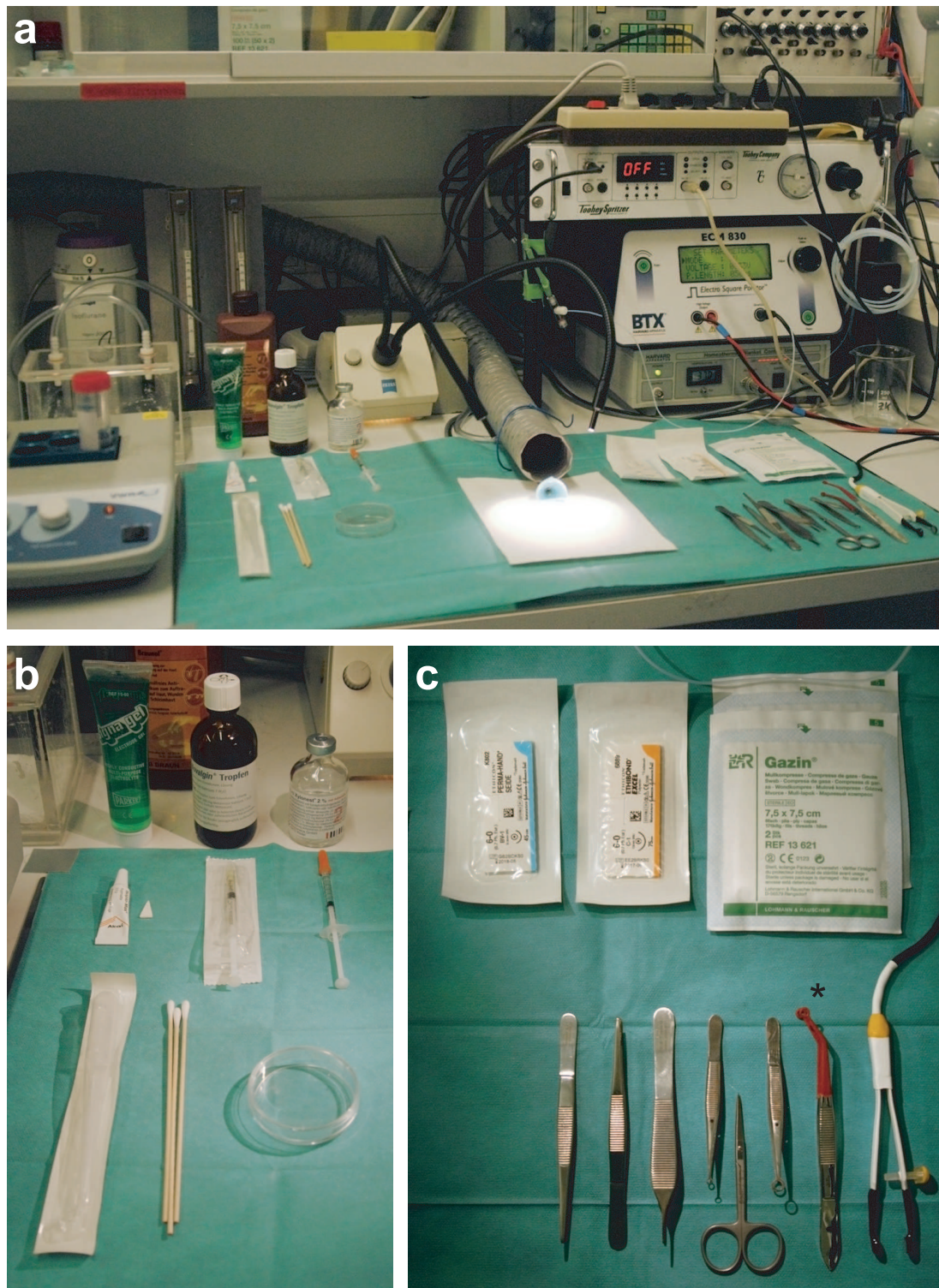
Figure 2.4: The operating area, tools and consumables. (a) The operating area prior to the start of a surgery. (b-c) The consumables and the tools used during the surgery. Asterisk marks the custom-made ring forceps with electrically insulated tips. Photo credit: Cvetalina Coneva.

of pregnancy were used for surgeries. In our early surgeries, we observed lack of maternal care in naive females and it was necessary to supply surrogate mothers for the survival of the pups. This was avoided by using experienced females.

Mice were first anesthetized with 3% isoflurane in a chamber for gentle handling during shaving of the abdomen with a trimmer. The isoflurane level was adjusted with a vaporizer and mixed with 100% O_2 at a flow rate of 800 ml/min. They were let to recover from anesthesia while being still handled and were administered orally with ~25 µl metamizole (500 mg/ml) as an analgesic. Mice do not swallow all of this volume, however, at such high concentrations, the amount they lick and what diffuses through the oral mucosa is sufficient.

Later, mice were anesthetized again with 3% isoflurane in the chamber, then laid dorsally on the multipurpose tissue over the heating pad and the head was placed into the custom made inhalation mask. Mice lose corneal reflexes under anesthesia. Therefore, Isopto-Max eye ointment was applied to the eyes to avoid drying during the procedure. The mice were restrained by taping their hind limbs onto the multipurpose tissue, and the forelimbs onto the inhalation mask. The anesthesia was reduced to operation levels (1.0-1.5% isoflurane). During the whole procedure the respiration was closely monitored. The isoflurane level was reduced if the mice started gasping, or elevated if the breathing became shallower and/or faster. The abdomen was disinfected with iodine tincture, and later cleaned with 80% ethanol. The mice were covered with sterile gauze pads moistened with saline, while leaving the abdomen accessible.

Surgery

A ~2.5 cm medial incision was made on abdominal skin starting from approximately the middle of the most posterior nipple pair using iris scissors. If the incision starts too posterior, then the adipose tissue underneath the skin makes stitching harder. The incision needs to be large enough that the uterine horns can be taken out without any resistance, however, it should also be considered that the length of the incision determines the time it takes for suturing. The incisions need to be straight and clear (**Fig. 2.5ab**).

After the skin was cut, ~50µl of Xylonest 2% (2 mg/ml prilocain with epi-
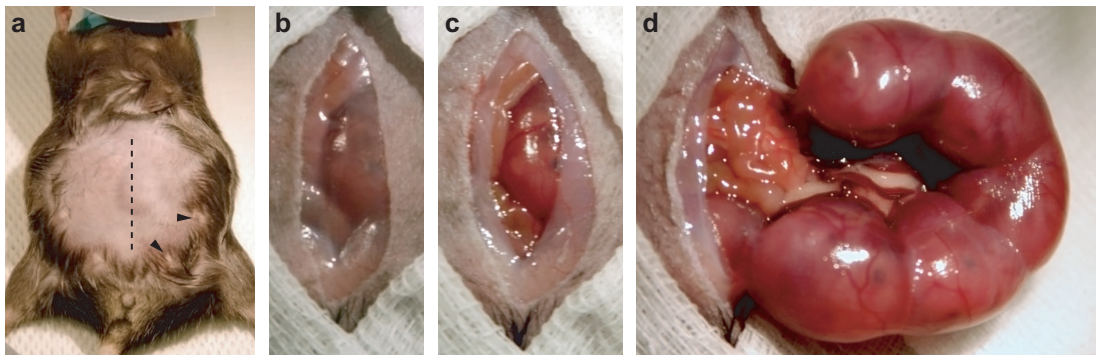
Figure 2.5: The incision. (a) The abdomen of a pregnant females shaved. The dashed line indicates the extent of the incision made during surgeries. Arrow heads mark left nipples of posterior nipple pairs. (b) The skin incision. (c) The abdominal wall incision. (d) A uterine horn exposed. Photo credit: Cvetalina Coneva.

nephrine) was spread over the incision and the tissue underneath as an additional local anesthetic and to stop any hemorrhage with the vasoconstrictor epinephrine. During the surgery, whenever there was a hemorrhage, Xylonest 2% was applied to cut blood vessel ends by dripping, complemented with compressions if necessary. Typically, hemorrhages should not be expected; most times the surgeries were executed without any.

Another slightly smaller incision was made on the abdominal wall through the linea alba (**Fig. 2.5c**). The linea alba is not vascularized, therefore incising through will not yield any hemorrhage. One of the uterine horns was pulled out using adson forceps with finely serrated tips, grabbing the uterus very gently from in between embryos and helping the pull with ring forceps. The fully exposed uterine horn was laid on the gauze pads, and kept moist by dripping saline from time to time (**Fig. 2.5d**). Exposing a single horn at a time minimizes the heat loss and drying.

Under a surgical microscope, each embryo was manipulated and held gently with ring forceps on its torso, and 1-2 µl of the DNA solution was injected into one of the lateral ventricles. This was a crucial step. If the injections failed to precisely target the lateral ventricles, the transfection efficiency turned out to be very poor. For precise targeting, the head was pushed against the uterine wall. The pipette was pushed through the parietal bone, approximately 1 mm equidistant to the sagittal and lamboidal sutures, at an angle $\sim$30°C to the tangential plane laterally
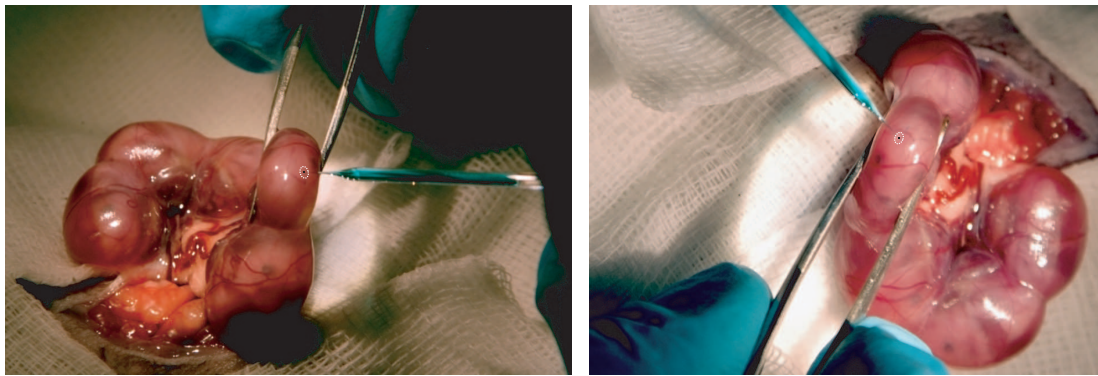
Figure 2.6: Pipette orientation to enter lateral ventricles of the embryos.
The pipette orientation is displayed at two different camera angles. The entrance
points are marked with black dots and encircled with dashed white ellipses. Photo
credit: Cvetalina Coneva.

and perpendicular to the sagittal suture (**Fig. 2.6**). The pipette was pushed with

pulses rather than a single push to avoid traveling too deep. If the injection was

too deep, then all the ventricles were filled with the DNA solution (**Fig. 2.7b**).

A correct injection filled only the targeted lateral ventricle (**Fig. 2.7a**). Before

continuing with electroporation, some time was given for the DNA solution to

diffuse and mix with the cerebrospinal fluid. Typically 3-4 embryos were injected,

then subsequently electroporated before moving to another set of injections.

The orientation of the electroporation electrodes and its contact to the tissue

was another very crucial step, especially to target V1. Some high conductive

electrode gel (covering $\sim 1/4$ of the electrodes at the tips) was applied to ensure
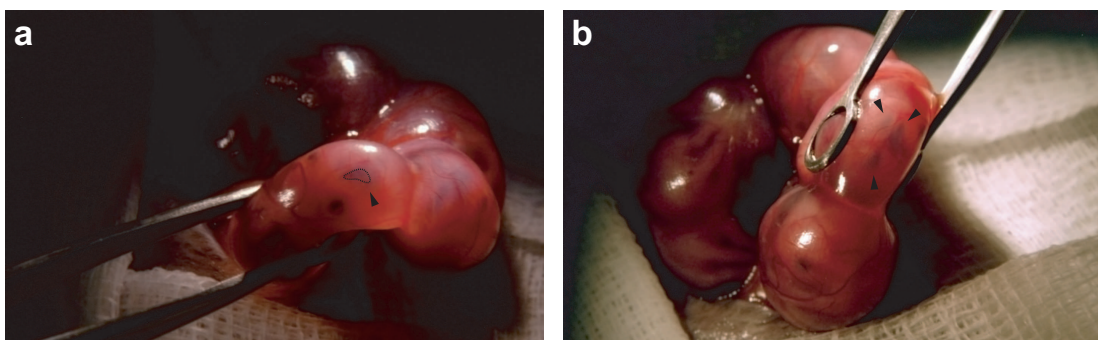
Figure 2.7: Injected ventricles. (a) A correct injection into the lateral ventricle of
embryos. Only the injected ventricle is filled (enclosed with dashed line). (b) A deep
injection into the lateral ventricle results in filling of all of the ventricles. Arrowheads
show the filled ventricles. Photo credit: Cvetalina Coneva.
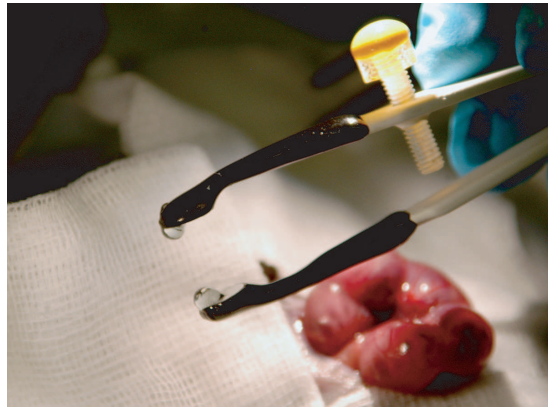
Figure 2.8: Electrode gel on the electrodes. One quarter of the electrodes at the tips are covered with the highly conductive electrode gel. Photo credit: Cvetalina Coneva.

the contact to the tissue (**Fig. 2.8**). The embryos were held on their torso with custom made ring forceps (bent and electrically insulated tips) (**Fig. 2.4c**, asterisk). The heads of the embryos were pushed against the uterine wall to minimize the amount of the amniotic fluid between the head and the uterus.

For targeting V1, the anode contacted between the contralateral eye and the nose, caring not to apply the electrical field through the eye (**Fig. 2.9a**). The cathode was brought in contact with the tissue above the dorsal posterior end of the injected ventricle, towards the cerebellum, in alignment with the central axis along the ventricle (**Fig. 2.9b**). These locations were gently touched with the gel. It was made sure that the ventricle was centered with the electrodes. During pulsing, the direction of the electrical field was always kept constant. If the electrodes or the embryo move during pulses, the efficiency of the electroporation drops. To avoid effects of the electrical field on neighboring embryos and/or the mother, the embryo to be electroporated need to be held up, away from the torso of its mother. Otherwise, twitches on the siblings or the mother would be observed. It should also be avoided to electroporate across large blood vessels.

Once one horn was finished with, it was put back in gently, caring to avoid any twists. The abdominal cavity was flushed with saline. Then the next horn was exposed for injections and electroporations. Often the transfection of embryos closest to the cervix or to the ovaries was skipped, since any damage to these
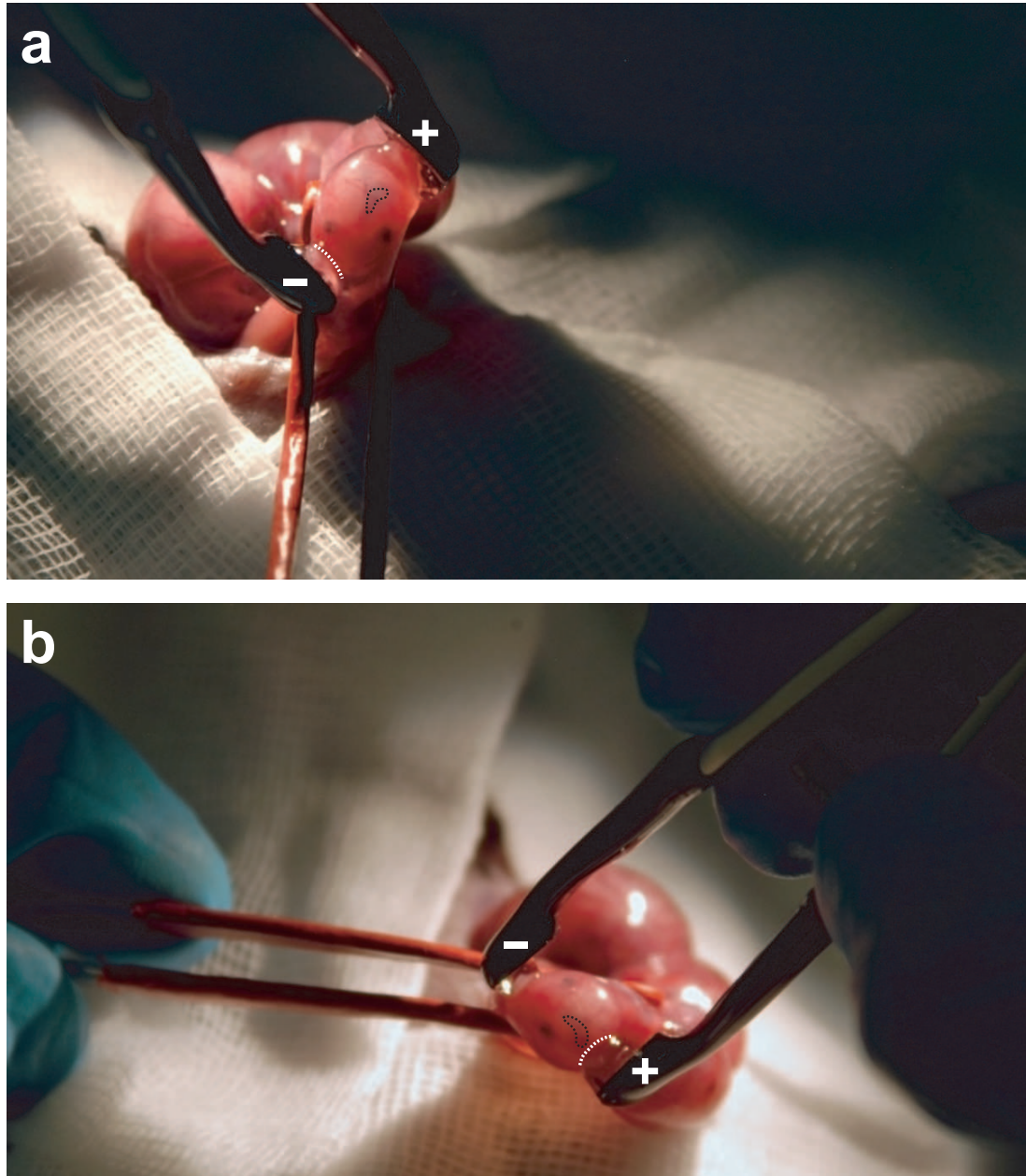
Figure 2.9: The electrode orientation for V1 targeting. Two different camera angles show the correct electrode orientation. The placement of anode (-) is clearer to see in a, and the cathode (+) in b. The rim of the gel contact is marked with white dashed lines. Ventricles are enclosed with black dashed lines. Photo credit: Cvetalina Coneva.
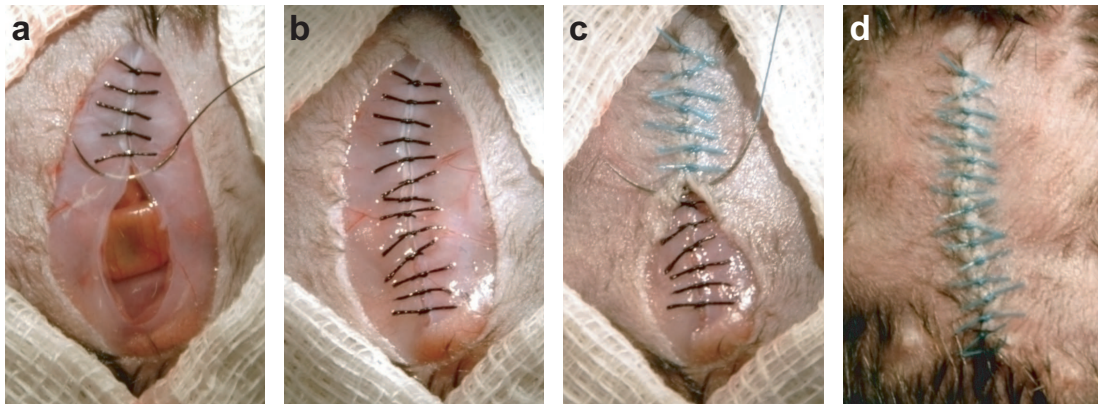
Figure 2.10: Sutures. (a) The abdominal wall stitched with silk sutures. Note the entry and the exit locations of the needle and stitch separation. (b) Closed abdominal wall. (c) The skin stitched with polyester sutures. (d) Closed skin. Photo credit: Cvetalina Coneva.

locations during embryo handling might lead to abortions.

Prior to closing, the abdominal cavity was flushed generously with saline, and the horns were lightly manipulated to slide on each other and to settle in place. Simple interrupted stitches were tied with square knots with one loop on the first throw, and two loops on the second throw. Needle entry and exit locations were ~1 mm away from the cut. The stitches were placed ~1 mm apart. The abdominal wall was sutured with silk sutures, and the skin with polyester sutures (**Fig. 2.10**). The skin should be sutured with polyester sutures, because mice cannot chew off the thread. After suturing was complete, some Xylonest 2% was dripped over the wound.

Post-Operation

The mice were let to recover under a heating lamp (150 W). They were provided with red transparent mouse houses and paper tissue in their cages for additional comfort during birth and nursing. They were closely monitored until after the delivery. After birth, the pups were observed for milk in their stomachs. A surrogate mother was placed in the cage if the pups were not fed. At postnatal day 3, the pups were screened for red fluorescence with a stereo fluorescence microscope. Positive pups were marked by tattoos on their palms of either left or right hind limb, depending on the hemisphere transfected. Tattooing was done

by inserting a tattoo ink coated sterile needle subcutaneously along the palms. The electroporated mice were used for experiments when they were 40-55 days old.

2.7 Plasmids

pCAGGS - hChR2(H134R) - EYPF - WPRE (plasmid 1), and pCAGGS - mCherry - WPRE (plasmid 2) were cloned as follows:

pCAGGS expression vector backbone, containing the synthetic CAG promoter (Niwa et al., 1991), and woodchuck hepatitis virus posttranscriptional regulatory element (WPRE) (Zufferey et al., 1999) was prepared from pCAGGS - ChR2 - Venus plasmid (Petreanu et al., 2007) by digesting it with NheI and PspXI restriction enzymes to remove the transgene. Backbone was isolated by gel electrophoresis, followed by gel extraction (QIAEX II Gel Extraction Kit).

hChR2(H134R) - EYFP transgene was extracted from pLenti - Synapsin - hChR2(H134R) - EYFP - WPRE plasmid (Zhang et al., 2007b) by polymerase chain reaction (PCR) (Saiki et al., 1988) using the forward primer PrimerF-A (primer sequences can be found in Appendix B) and the reverse primer PrimerR at 70°C annealing temperature. Flanking regions included NheI restriction site in the forward primer and PspXI restriction site in the reverse primer. The PCR product was isolated and cleaned by gel electrophoresis followed by gel extraction. Insert was acquired by digesting the PCR product with NheI and PspXI restriction enzymes.

mCherry transgene was extracted from pLenti - CaMKIIa - hChR2(H134R) - mCherry - WPRE plasmid (Zhang et al., 2007b) by PCR using the forward primer PrimerF-B and the reverse primer PrimerR at 65.5°C annealing temperature. Flanking regions included NheI restriction site in the forward primer and XhoI restriction site in the reverse primer. The PCR product was isolated and cleaned by gel electrophoresis followed by gel extraction. Insert was acquired by digesting the PCR product with NheI and XhoI restriction enzymes.

PCRs were done with iProof HF master mix with 100 pg template and each primer at 500 nM final concentration. After initial denaturation at 98°C for

30 s, 40 cycles of 10 s denaturation at 98°C, 30 s annealing at the indicated temperatures above, and 45 s extension at 72°C were executed, and the reaction ended with 10 min final extension at 72°C. All restriction digestions were carried out at 37°C for 3 hours.

Inserts were put to overnight ligation reactions with the prepared backbone (3:1 molar ratio) and T4 DNA ligase at 16°C to get target plasmids. Ligation products were transformed to competent *Escherichia coli* DH5α. The transformants were grown on lysogeny broth (LB medium) agar plates with ampicillin (100 µg/ml) overnight at 37°C. The colonies were prescreened for correct target plasmids by colony PCR (Trower, 1996) using the forward primer PrimerSeq-G and the reverse primer PrimerSeq-K for plasmid 1, and the forward primer PrimerSeq-I and the reverse primer PrimerSeq-K for plasmid 2. Target plasmids were obtained by mini prep (QIAGEN Plasmid Mini Kit) from overnight liquid cultures of the identified colonies, and were verified by sequencing (in-house facility). The following primers were used for sequencing: for plasmid 1, PrimerSeq-A, B, C, D, E, F, G, and H, and for plasmid 2, PrimerSeq-A, I, J, and K.

Finally, plasmid 1 and plasmid 2 were purified at high concentrations (>4.0 mg/ml) from overnight liquid cultures (LB medium, 100 µg/ml ampicillin, 37°C) with EndoFree Plasmid Mega Kit. Impurities, especially genomic DNA contamination, reduces tranfection efficiency with IUE. Extra attention must be paid for high purity.

2.8   Acute Brain Slices

Before starting with the slice preparation:

- ACSF solutions (see Appendix B for the recipes) (Scheuss et al., 2006) were oxygenated and pH stabilized via carbogen bubbling,

- solutions and equipment were equilibrated to their application temperatures (recovery ACSF, 35°C; choline ACSF, 0°C; vibratome slicing chamber, 0°C),

- blades were cleaned with diethyl ether off the oil residues from manufactur-

ing, and

- orientation of the cutting blade of the vibratome was calibrated.

Prior to harvesting brains, the mice were perfused with cold choline ACSF. This improves the quality of the slices, especially of those from older mice (>p20). For this procedure:

1. The mice were anesthetized, first with isoflurane (0.7 ml in ∼3 L chamber), then while the mice were still drowsy, further with 200 μl intraperitoneal (IP) injection of 7% chloral hydrate[1] in saline using a 27 gauge needle (Field et al., 1993). Before continuing, it was made sure that the mice were completely anesthetized via observing complete suppression of the toe pinch reflex. If after 5 min the reflexes were still present, more chloral hydrate was injected, up to 500 μl, paying attention to avoid overdosing, which is hinted by appearance of the gasp reflex.

2. The limbs of the mice were fixed in supine position. The thoracic cavity was opened and the heart was exposed.

3. The right atrium was incised, and the left ventricle was entered with a 23 gauge needle connected to a 10 ml syringe filled with choline ACSF. The contents of the syringe was slowly injected to the ventricle, in about 1 min, purging out blood and replacing it with choline ACSF. If the perfusion worked, twitches were observed at the tail.

After the mice were perfused, the brain was taken out. Upon successful perfusion, the brain was completely without blood, with no vessels visible. Before any cuts were made to the brain, it was let to cool down in choline ACSF for 1 min. Later, the frontal half of the cerebrum was removed coronally at midline. The cerebellum was also removed. The dorsal half of the cerebrum was glued onto the slicing platform of the vibratome, frontal side down. The hemispheres were separated prior to slicing. A surgical blade was used for all of these mentioned cuts.

---

[1]Chloral hydrate is not advised to be used as an anesthetic for survival surgeries.

The slicing platform was transferred to the slicing chamber, filled with choline ACSF. 300 µm thick slices were obtained with the following parameters: cutting speed, 0.14 mm/s; cutting amplitude, 1 mm. Slices were transferred to a chamber filled with recovery ACSF and under continuous carbogen bubbling and let to recover for 1 hr before being used in experiments. 3-4 sections were cut for V1, yielding 6-8 slices for both hemispheres. Only the slices from the transfected hemisphere were collected from the electroporated mice.

2.9 Histology

For Nissl staining and immunohistochemistry the mice were perfused as described in Section 2.8, but first with 10 ml saline containing 0.0005% lidocaine and 0.00028% heparin, then with 10 ml 4% paraformaldehyde (PFA) solution. The brains were taken out and incubated in 4% PFA for a minimum of 2 days at 4°C. Afterwards, the brains were transferred to 30% sucrose in phosphate buffered saline (PBS) solution and kept at 4°C until they sank (~2 days). Once the brains were ready to slice, 40 µm sections were cut at a sliding microtome. Sections were incubated in PBS overnight at 4°C.

When sections were ready to use, immunostaining was done as follows:

1. Wash with PBS three times, 10 min each.

2. Incubate in PBS containing 0.4-1% Triton X-100 and 10% normal goat serum (NGS) overnight at 4°C.

3. Hybridize primary antibody by incubating in PBS containing 0.4-1% Triton X-100, 5% NGS and 1:1000 dilution Anti-GFP overnight at 4°C.

4. Rinse with PBS three times, 10 min each.

5. Hybridize secondary antibody, , by incubating in PBS containing 5% NGS and 1:200 dilution Anti-Rabbit overnight at 4°C.

6. Wash with PBS three times, 10 min each.

Afterwards, Nissl staining was done as follows:

1. Wash with PBS for 5 min.

2. Wash with PBS containing 0.1% Triton X-100 for 10 min.

3. Rinse with PBS two times, 5 min each.

4. Incubate 20 min in fluorescent Nissl stain (NeuroTrace) diluted 100 times in PBS.

5. Rinse with PBS three times, 5 min each.

Once all stainings were finished, the sections were mounted on microscope slides.

2.10 Analysis

The whole analysis was conducted on custom software developed using Matlab programming language. The code was optimized to make the analysis scalable, to handle different loads and types of data and to seamlessly execute on a modest system with 2 GB of RAM. It was designed to be completely modular and expandable to incorporate new features. It is an extensive suite of software, consisting of approximately 42000 lines of code, and is called "Ateş Böceği"[2].

2.10.1 Data Organization

The acquisitions from Colibri produced separate TIFF images for each slice in z-stacks, or for each frame in time lapse imaging. Electrophysiology data were separately saved in MAT files. An additional module was programmed in Matlab and was integrated into the imaging software to be triggered at every acquisition, which then connected to the MultiClamp 700B amplifier to dump all of its settings. This module also provided a graphical user interface (GUI) where the experimenter could supply information about the experiments, e.g. experiment type, information about the mice in experiment, solutions used, cell tag, cell type, slice tag, stimulation location, etc., basically anything that could describe

---

[2]firefly

the experiment. The amplifier dumps and user supplied information were saved in separate MAT files.

All in all, each experiment produced thousands, sometimes more than 10 thousand files, distinguished primarily by file names. Handling such quantities of files was not practical in analyzing, transferring or backing up. Therefore, all of the data and associated meta-data from a single experiment were first parsed and organized in a single binary hierarchical data format (HDF5) file[3] using the application programming interface (API) in Matlab. Results of the analyses were also stored in the same file. Utilization of HDF5 had several advantages: (i) The library is open source and APIs exist for most of the popular programming languages making these files truly cross-platform. (ii) Different multidimensional data structures can be arranged in groups within the file, which makes the organization easy and robust for access. (iii) Furthermore, additional organizational schemes may be implemented without the need of duplicates by internal symbolic linking. (iv) Attributes which describe the data can be assigned and easily fetched along with the data. (v) And most importantly, for better performance and memory usage, the data can be fetched partially, i.e. only the portion of data which will be processed (e.g. from a region of interest (ROI) over time) can be read into the memory without the need to load the contents of the whole file. Such a strength cannot be achieved when using data which are fragmented in different files or with file formats such as TIFF or MAT, on which, for instance Matlab cannot operate unless the file is completely loaded to the memory. (vi) Moreover, these partial accesses can be stored virtually, without any duplication via symbolic links, and can be accessed anytime without the need of redefining them.

To improve the performance, flexibility and ease of programming even further, each experiment file was complemented with SQLite[4] databases. All of the attributes of raw and processed data, and analysis results with links to the associated data were stored in these databases to provide a directory service. This allowed at any point of analyses to quickly query and fetch the location of the

---

[3]http://www.hdfgroup.org/HDF5/
[4]http://www.sqlite.org/

data or the analysis results with specific attributes and to combine and compare specific data or analyses from selected experiments.
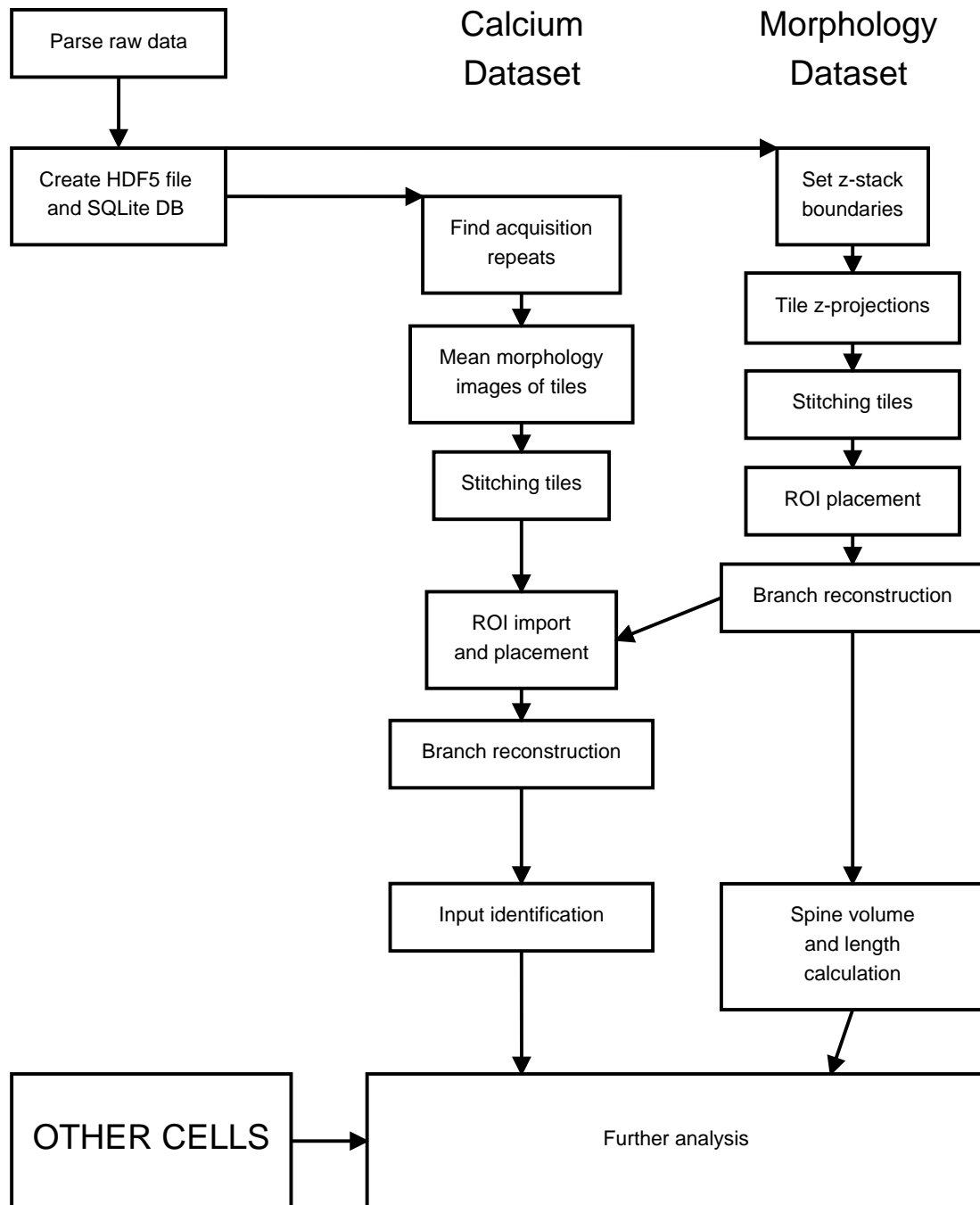
2.10.2   Analysis Flow

Analysis of the data consisted multiple steps, some completely automated, while some of the steps required manual input. **Figure 2.11** summarizes the individual steps of the analysis. The details of each step are explained below.

Parsing Raw Data and Initiation Processes

All of the files generated during the experiment from a cell were parsed and organized in a HDF5 file. A SQLite database was created for attributes of the raw data for each cell. These database entries were also appended to a separate database where all data from all cells were pooled together. Two datasets were acquired during experiments. One was structural z-stacks for tiles (morphology dataset), and the other time-lapse calcium imaging of tiles (calcium dataset). These datasets were processed independently. Boundaries in the z-dimension were set manually on the morphology dataset. Later, respecting these boundaries, maximum z-projections were taken for each tile to be used during subsequent processing. For the calcium dataset, all of the acquisitions were scanned to identify those that were repeats of each other and were grouped together. Mean morphology images of the repeats were generated by averaging all of the morphology image frames in the time series of all the acquisitions from the respective repeats.

Stitching

The coordinates acquired from stage controller during the experiments were prone to mechanical noise, and could not reliably be used to relate images from different coordinates. Establishing such relations were necessary since often the same spines were measured in different tiles at different coordinates and needed to be identified the same. For this reason, a software-based fine tuning was necessary to correct this offset due to noise. This was done by first setting assumed overlap regions on the tiles based on the stage coordinates, then cross-correlating these

Figure 2.11: Analysis Flow Chart. General steps in the analysis of the experimental data. Refer to the text for details.

regions to find the exact overlap. A semi-automatic operation mode with a GUI let users intervene at any step to check and correct if automated offset calculations were to produce errors. These true offsets between the tiles were calculated separately on the two datasets, using maximum z-projections as tile images for the morphology dataset, and mean morphology images as tile images for the calcium dataset. The offset values were saved and used extensively when defining ROIs. Also, stitched images were rendered using these offsets to acquire whole images of dendritic branches which were mapped during the experiments (**Fig. 3.6c**). These renders were further processed with nonlinear lookup table assignments for visualization purposes only.

Region of Interest Definitions

Structures in the images were enclosed with rectangles manually to be able to extract information for analysis, separately on the two datasets, easing the process with coordinate translations across the datasets. The datasets consisted of many tiles, sometimes close to a hundred. With the help of the offsets calculated during stitching, translations could be applied to avoid annotating each single tile independently.

First, rendered merge images were annotated, then the ROI coordinates were translated to individual tiles. ROIs on individual tiles were readjusted, especially for those with rotational distortions. ROI coordinates from the morphology dataset were translated to the calcium dataset, to preserve same ROI identifiers (IDs) in both datasets. Consequently, the same readjustments were made on individual tiles of the calcium dataset. Eventually, all visible spine heads were enclosed with rectangular ROIs and the dendritic branches were traced with line segments. Additionally, the spine necks were traced in the morphology dataset to measure the spine length. Spine ROIs in the calcium dataset were paired with ROIs enclosing the closest dendritic regions at the spine bases to compare the spine signal to the dendrite signal.

Spine volume and length information was acquired from the morphology dataset, and calcium signals from the calcium dataset. Spine volume and length information could only be extracted from spines extending laterally, since the

spines sticking up or down in the z-dimension could not reliably be separated from the dendrite due to the low resolution in this dimension in two-photon imaging. Hence, the morphology dataset lacked the annotations of these spines. Spine distances along the dendrite were extracted from 3D reconstructions on the calcium dataset, where all visible spines were annotated.

Image Analysis

For all calculations from the ROIs, the mean blank frame intensity was subtracted first to remove the electrical offset.

The calcium signals were extracted from the spine and the dendritic base ROIs from the calcium dataset. For the spine signal, the brightest 70% of pixels in the red channel (volume marker, Alexa 594) of ROIs were selected to fetch signals from the red and green (calcium indicator, Fluo-5F) channels, since round spine heads enclosed with rectangular ROIs had background signal contamination around the rims of spines. The mean value of these pixels in each time frame represented the fluorescence intensity for the time point. The change in calcium fluorescence (ΔG) was calculated by subtracting the mean green fluorescence of the baseline from all frames of the green channel. ΔG was normalized by dividing the signal by the mean red channel fluorescence from all frames. The ΔG/R were used for subsequent analysis. Similarly, the dendrite signal was acquired, but without any pixel selection. These spine and dendrite signals were used to decide whether there were inputs to spines. Decay time-constants (τ_{decay}) were calculated for ΔG signals by exponential curve fitting.

To be able to detect whether spines received inputs, first, the peaks of spine and dendrite signals were obtained. This was done for each acquisition independently. The peak of a ΔG/R signal was the highest value of the second, third or fourth time point after the stimulus. To reduce the effect of noise, these time point values were each averaged with one previous and one next time point value. In each acquisition, for the spine and the dendrite ΔG/R signal, the standard deviation of the baseline and the last five time points were calculated, and the highest of these standard deviation values was selected to represent the noise of the acquisition. A spine was detected to receive input if its peak was higher than

the dendrite peak by three standard deviations of the noise. Decisions of this algorithm were verified by a human subject for each individual acquisition.

The calcium signal over the entire stretch of the dendrite in individual tiles were acquired by automatically creating ROIs along the trace of the dendrite. These ROIs had the span of 0.5 µm along the trace, and extended perpendicular to the trace by 0.6 µm in both directions. Any spine overlay on these ROIs were removed before processing them. $\Delta G/R$ for each ROI was calculated as described above.

Spine volume and length were measured from the morphology dataset. For the spine volume, background was subtracted and the sum of pixels in ROIs were calculated for each z-plane in all tiles for a spine. The highest value represented the volume of the spine. Since this value is affected by the depth, the fluorophore filling and the laser power, these were normalized for cross comparisons between experiments. A universal mean spine volume was assumed, and the measured volumes were normalized to the mean spine volume of segments. A segment was the dendritic stretch between branching points. Lengths were measured from the spine neck traces as 2D projected lengths.

Spatial Analysis

From the extracted spine distances along the dendritic segments, dendrograms were constructed as simplified visualizations for the mapped branches. Order-based dendrograms (Appendix A.1) represented neighborhood information in numbers of spines. Distance-based dendrograms (Appendix A.2) were constructed from real distances extracted from 3D reconstructions of mapped branches. Nearest neighbor distance distributions between spines receiving input were computed for both types of dendrograms and were compared to Monte Carlo simulations to spot whether input locations displayed a difference to random input distribution.

Inputs that lay within 10 µm to each other were treated to belong to the same cluster. These patterns were analyzed for likelihood of occurrence.

2.10.3 Methods of Analysis

Exponential Curve Fitting

Exponential curves were fit to the spine and the dendrite signals to calculate τ_{decay}, in two steps, assuming the following model:

$$I(t) = A(1 - e^{-t/\tau_{\mathrm{rise}}})(e^{-t/\tau_{\mathrm{decay}}}) + I_0$$

First, approximate fits were obtained by scaled template matching (Clements and Bekkers, 1997), with templates created from a range of τ_{decay} and τ_{rise} values. The pair of τ_{decay} and τ_{rise} which yielded the minimum sum of squared error, together with the corresponding scaling factor and the offset were used as initial coefficients for nonlinear regression fitting based on the Levenberg-Marquardt algorithm (Marquardt, 1963). Time constants from nonlinear fitting were used to describe the signal time constants.

Monte Carlo Simulations

For each mapped cell simulated branches were generated by keeping all properties (i.e. total number of spines, total number of inputs, and location of spines) the same as the mapped branches, but randomly assigning the inputs to spines. Subsequently, these simulated data were analyzed exactly the same way as if they were experimental data. Repetition of simulations 1000 times yielded distributions of analysis results which reflect what could be expected from a random distribution of inputs on branches.

Statistics

All populations were assumed to be normally distributed. Two-sample two-tailed t-tests were applied when comparing two populations. Z-tests were applied when comparing a single value to a population. In plots asterisks illustrate p-values as *, $p<0.05$; **, $p<0.01$; and ***, $p<0.001$.

The values given in the text are mean±SEM (standard error of the mean), if not indicated otherwise.

Cluster Likelihood Scores

Cluster likelihood scores are calculated based on combinatorics according to the following formula[5]:

$$p_{N,n}(l_M, m, l_g) = \left(\sum_{i=1}^{N} \binom{M_i^{l_M} - 2}{m - 2} \binom{N - M_i^{l_M} - g_i^{l_{gl}} - g_i^{l_{gt}}}{n - m} \right) \frac{1}{\binom{N}{n}},$$

where,

$$M_i^{l_M} = \begin{cases} \text{spines}(d_i, d_i + l_M) & \text{if spines}(d_i, d_i + l_M) \geq m \\ 0 & \text{if spines}(d_i, d_i + l_M) < m \end{cases}$$

$$g_i^{l_{gl}} = \text{spines}(d_i - l_g, d_i)$$

$$g_i^{l_{gt}} = \text{spines}(d_i + l_M, d_i + l_M + l_g).$$

N is total number of spines in a segment; n, total number of inputs to the segment; l_M, length of the cluster, whose likelihood is calculated; m, number of inputs of the cluster; l_g, gap length; d, distance of spines from segment origin.

---

[5]Unpublished work by Dr. Volker Scheuss.

Chapter 3

Results

In this study, L5 and L2/3 inputs were mapped onto the basal dendritic branches of L5 pyramidal neurons.

Prior to the mapping experiments, the experimental design was verified. It was confirmed that ChR2 expressing presynaptic neurons were confined to L5 in the Thy1-ChR2 mice, and to L2/3 in the electroporated mice. The photostimulus protocol was optimized respectively for the wtChR2 and the codon optimized ChR2 H134R mutant (hChR2(H134R)) to be able to evoke the highest presynaptic activity. The photostimulation protocols were validated not to be evoking any unspecific activity in the neurons other than the ChR2 expressing ones in the targeted presynaptic layers.

When probing L5 to L5 connectivity, presynaptic inputs could reliably be detected on the postsynaptic cells. The analysis of the spatial distribution of the identified inputs presented evidence for a clustered organization. Spines with identified input did not differ morphologically from the spines with no identified input. Analysis of spine-dendrite signal coupling did not show a correlation between the coupling ratio and the spine neck length.

In L2/3 to L5 mapping experiments, sufficient number of inputs could not be detected to analyze their spatial organization, most likely due to inefficiencies in the transfection.

3.1   Targeting of Presynaptic Neurons

To be able to make safe conclusions about the connectivity between the pre-
and posysynaptic neuronal populations, it was important to verify whether the
presynaptic population could be targeted specifically to express ChR2. If the
presynaptic population was contaminated with neurons belonging to other lay-
ers, then mapping would include nonspecific inputs, rendering the experiment
unreliable. We examined 40 μm thick Anti-GFP immunostained slices of V1
of Thy1-ChR2 mice and observed that wtChR2 expressing neurons were really
confined to L5 in the cortex (**Fig. 3.1a**).

To estimate the amount of undetectable L5 input, the percentage of the
wtChR2 expressing neurons needed to be established. Counts from fluorescent
Nissl stainings (**Fig. 3.1b**) quantified the L5 neuronal density to be ∼79000
neurons/mm^3, in agreement with what was shown before (∼85000 neurons/mm^3,
Schüz and Palm, 1989). We counted the apical dendrites of fluorescent neurons
from immunostainings to approximate the number of wtChR2 positive neurons,
because the somata of these neurons were not clearly visible, since the trans-
gene was trafficked to the cellular membrane (**Fig. 3.1c**). The positive neuronal
density was observed to be ∼3000 neurons/mm^3, corresponding to ∼4% of the
L5 population. However, this contradicted the observations from photostimulus
power calibration experiments (Section 3.2), where almost every neuron that was
blindly selected responded to the light stimulus; either by firing APs or by sub-
threshold responses. This indicated that the expression level in Thy1-ChR2 varied
greatly, and the immunopositive ∼4% population reflected the "highly expressing
neurons".

A similar verification was obtained for the electroporated mice. The IUE
technique presented difficulties for V1 targeting and high transfection efficiency.
For the experiments, the mice were selected first based on the red fluorescence
(mCherry) visible across the skull at postnatal day 3 (**Fig. 3.2a**), then, after
preparation, based on the density of positive neurons and the transfected region
(**Fig. 3.2b-d**). The density of the transfection varied substantially from prepa-
ration to preparation (not quantified). The slice in **Figure 3.2** is an example

of dense transfection and does not represent a typical outcome of the procedure, however, it does represent a typical preparation used in the experiments. Targeting of the V1 L2/3 presynaptic population was very specific. Its dense axonal arborization at L5 could also be observed.

3.2 Characterization and Calibration of Optical Stimulation

The number of pulses in the photostimulus needed to be maximized in order to maximize the release probability and assure synaptic transmission. This required the highest applicable stimulus frequency. We selected 30 Hz based on what was described as the maximum reliable performance for ChR2 (Berndt et al., 2011; Boyden et al., 2005; Lin et al., 2009). It was also shown in Thy1-ChR2 mice
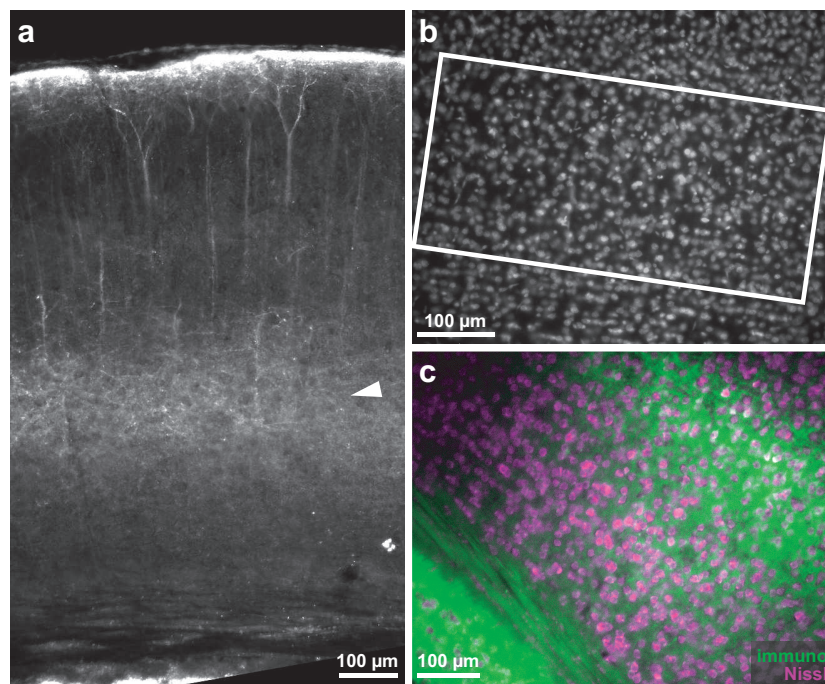
Figure 3.1: wtChR2 expression in Thy1-ChR2 mice. (a)An immunostained 40 µm thick slice from a Thy1-ChR2 mouse displays the wtChR2 expressing neurons confined to L5, observable by the dense fluorescence marked with the arrowhead. (b) Fluorescent Nissl staining of the slice in a, zoomed in to L5. The area used for the quantification of L5 neuronal density is enclosed with the rectangle. Measured density was $\sim$79000 neurons/mm^3. (c) Overlay of immuno (green) and Nissl stainings (purple) illustrate that wtChR2 is not expressed in the cytosol, therefore somata remain considerably dark.

that 30 Hz was the maximum photostimulus frequency that cortical pyramidal neurons could follow (Wang et al., 2007).

Due to the requirement of PMT protection (Section 2.2), it was not possible to photostimulate and image simultaneously. To minimize the time between the first stimulus pulse and the resumption of imaging, it was necessary to fit the stimulus in a single imaging frame of 100 ms duration. A stimulus with 3 light pulses was chosen considering also the shutter lag. With the frequency and the pulse number chosen, the power and the width of the stimulation pulse were optimized to drive ChR2 positive neurons most efficiently, caring not to damage them or the ChR2 proteins with strong illumination.

For wtChR2, we acquired cell attached recordings from blindly selected V1 L5 neurons of Thy1-ChR2 mice, while stimulating them with varying power (1, 2, 4, 6, and 9 mW at objective lens back aperture) and pulse widths (1, 2, and 5 ms) at full field aperture. Increasing the power and the pulse width increased
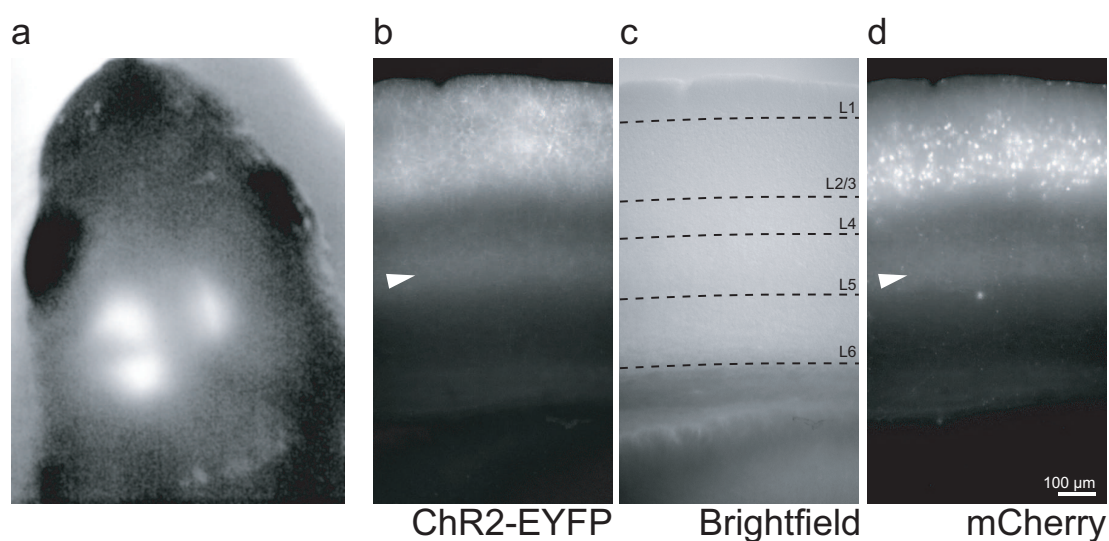
Figure 3.2: hChR2(H134R) expression in electroporated mice. (a) After IUE, transfection was visible across the skull at postnatal day 3, which gave a first impression about the efficiency and the regional targeting of the transfection. Here, a pup with dense transfection at hippocampus (right hemisphere) and a wide region from somatosensory cortex to V1 (left hemisphere) is presented. Visible fluorescence is from mCherry. (b-d) A 300 μm acute slice displays location of the positive neurons in L2/3 of V1 with membrane-bound hChR2(H134R)-EYFP fluorescence (dense dendritic arborization), and with cytosolic mCherry fluorescence (more pronounced somata). Brightfield image shows white matter (dark fibers) for orientation and outlines layers of cortex. Note the dense axonal arborization at L5, marked with arrowheads.
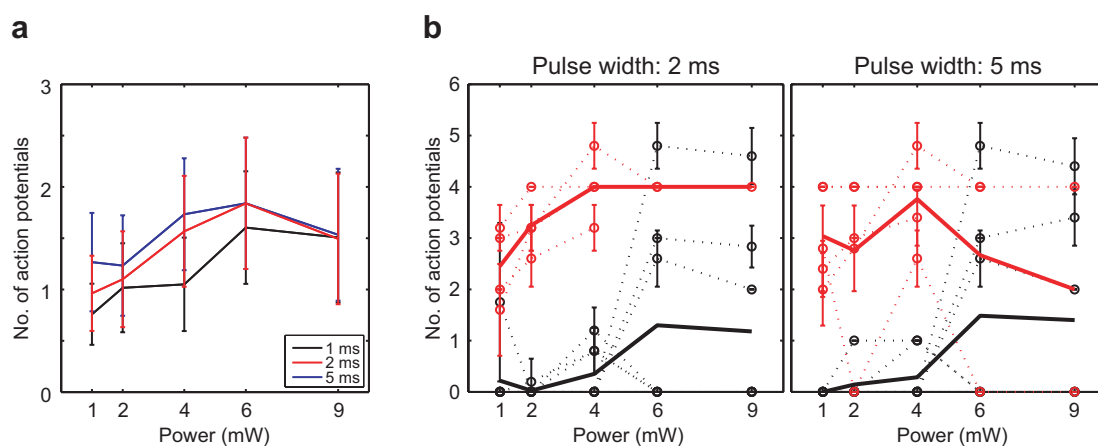
Figure 3.3: Dose-response curves for wtChR2. (a) Average number of APs measured in cell attached mode at different light intensities and at different pulse widths (see legend) of 3 light pulses at 30 Hz (n=12 cells). (b) Average AP count at different light intensities with 2 ms pulse width (left) and with 5 ms (right). The cells are separated into two groups depending on their responsiveness to the light stimulus. Red lines belong to high responding cells (n=4 cells, at 2 ms pulse width; n=5 cells, at 5 ms), black lines to low responding cells (n=8 cells, at 2 ms pulse width; n=7 cells, at 5 ms). Dashed lines represent data from individual cells and thick lines the mean of these data. Error bars correspond to standard error in a, and standard deviation in b.

the AP yield, with the exception of 9 mW (n=12 cells, **Fig. 3.3a**), revealing an adverse effect of increased illumination.

The measurements were analyzed once again by dividing the cells into two groups depending on their responsiveness to light. "High responding" were neurons which fired on average more than one AP at low power settings (1, 2, and 4 mW), whereas "low responding" neurons fired less than one. Low responding neurons responded more to increasing illumination without any negative effect. However, the high responding neurons performed worse at high illumination intensity (**Fig. 3.3b**). In summary, for the experiments, the stimulus was chosen to be 3×2 ms light pulses (470 nm) at 30 Hz with 4 mW power (objective lens back aperture). This stimulus yielded an average of 1.57±0.54 APs in Thy1-ChR2 preparations.

In electroporated mice, we expected less neurons to express ChR2 when compared to the transgenic line. Additionally, severed axons during the slice prepera- tion would further reduce the viable presynaptic neuronal population. Moreover, it was not possible to stimulate cell body layer of L2/3 while imaging postsynap-

tic cells at L5 due to the design constraints of the experimental setup. Therefore, we checked if the axons could locally be depolarized and driven to fire APs, as reported by Petreanu et al. (2007).

While recording from hChR2(H134R) expressing neurons in L2/3, the photostimulus was delivered to the slice with a reduced field aperture ($\sim$80 μm diameter at object plane) either over L5, where the axons of L2/3 neurons innervated (axonal stimulation), or over L2/3, where the presynaptic somata lay (somatic stimulation). Axonal stimulation yielded APs with rapid onsets and longer delays. In contrast, the APs exhibited slow onsets and shorter delays with somatic stimulation (**Fig. 3.4a**, inset). The difference was more pronounced when the neurons failed to fire APs. Axonal stimulation did not manifest any response to the light pulses in failures, whereas subthreshold potentials were detected with somatic stimulation (**Fig. 3.4a**).

We deduced that with somatic stimulation, both APs and the ChR2 driven depolarization could be measured at the soma. However, with axonal stimulation, the local ChR2 depolarization could not propagate to the soma, and therefore only the backpropagating APs could be resolved. This led to the conclusion that it was possible to elicit APs via local axonal depolarization, which also suggested that the stimulation area could be kept to a minimum. This was an advantage in terms of reducing the overall excitation and the photodamage in the slice.

We also used 3 pulses at 30 Hz to stimulate axons of hChR2(H134R) expressing L2/3 cells, as discussed above, and optimized the stimulus protocol through similar dose-response measurements (pulse widths: 2 and 5 ms; power: 250, 350, 500 μW at the objective lens back aperture, see **Fig. 3.4b**). The light intensities used for optimization appear to be significantly lower than what was used for wtChR2, however this is due to reduced field aperture. It should be noted that the energy density was kept comparable, e.g. 4 mW with open aperture corresponded to 250 μW with reduced aperture.

Illumination intensity had no adverse effect on hChR2(H134R) expressing neurons, therefore 5 ms pulse width and 500 μW power was chosen for the experiments. This setting yielded an average of 2.14±0.14 APs in the L2/3 neurons
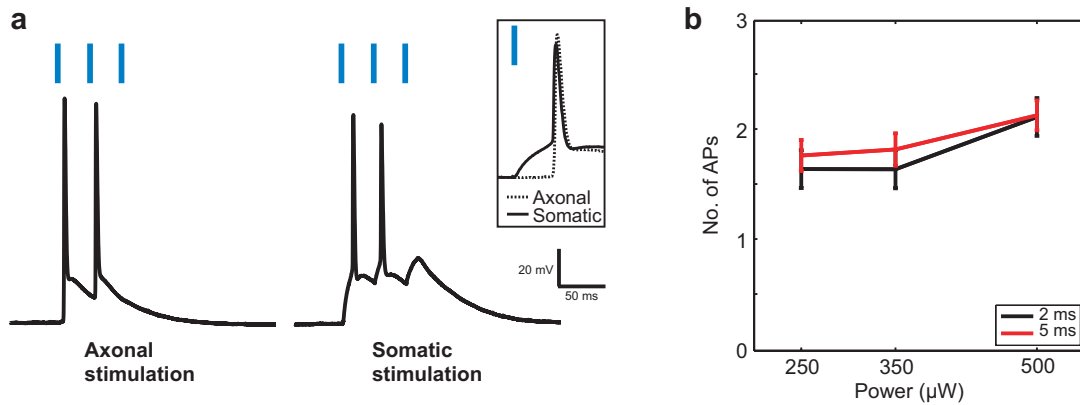
Figure 3.4: **Axonal excitability and dose-response curves for hChR2(H134R).** (a) Light stimulus, as indicated with blue lines, was delivered either over L5 to stimulate axons (left), or over L2/3 to stimulate the cell body (right). Failed response to the third pulse is not observable when the axon is stimulated, whereas a subthreshold current is measured in the somatic stimulation. The inset shows aligned APs of axonal (dashed) and somatic (solid) stimulation and depicts the difference in onset. (b) Dose-response curves for hChR2(H134R) at different light intensities and pulse widths. Error bars are standard error.

per stimulus consisting of three pulses. One concern was whether photostimulation would deplete the functional hChR2(H134R) channels over time on a thin structure like an axonal segment with limited membrane area. The endurance of the axonal stimulability was tested by illuminating the same area 100 times, while measuring for the number of elicited APs in the L2/3 neurons. There was no reduction in the performance (data not shown, n=4 cells).

3.3 Specificity in Evoked Presynaptic Activity

Once the stimulation protocol was optimized, it was necessary to confirm that the protocol did not evoke any APs in cells other than the ChR2 positive presynaptic population. Such an unspecific activity would have contaminated the mapping results with inputs delivered via polysynaptic transmission. Using the same ACSF as in mapping experiments, we measured responses of ChR2 negative cells in different layers, while stimulating at L5, with field aperture open in the Thy1-ChR2 mice, or reduced in the electroporated mice. Cell attached recordings were performed not to interfere with the membrane potential. In the electroporated mice, only L2/3 or L5 neurons were probed as they are the main
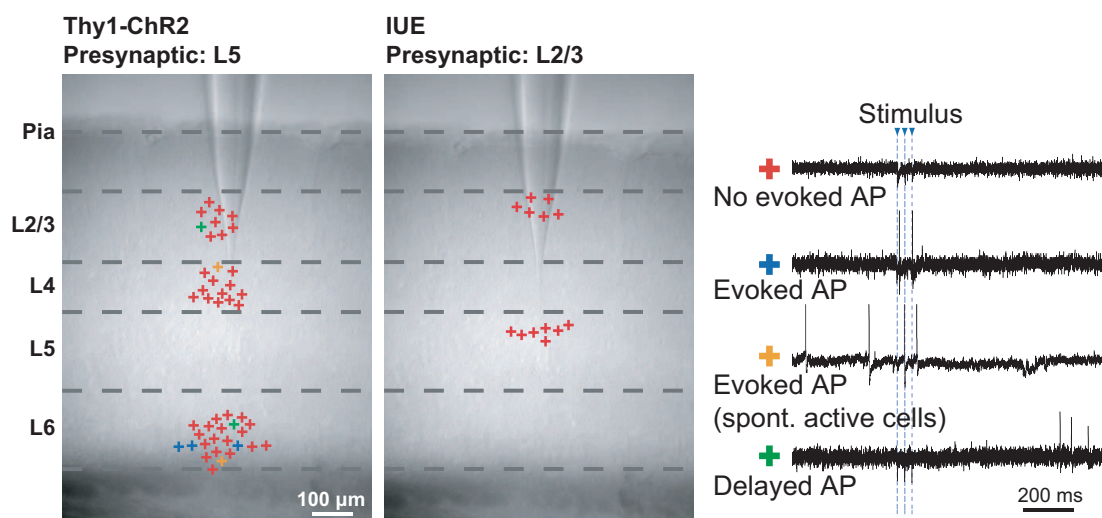
Figure 3.5: Unspecific activity in the ChR2 negative neurons. Spiking in neurons were measured by cell attached recordings upon light stimulus at L5. Cross markings show the vertical location of the cells which were recorded in slices from Thy1-ChR2 mice (left), and in electroporated mice (middle). Color codes for the type of activity which was observed; red, no evoked AP; blue, evoked AP; yellow, spontaneously active neurons with activity during stimulus; and green, delayed AP. Example traces for the different types of evoked activity are shown together with the stimulus (right).

targets of L2/3 pyramidal neurons.

Recordings in slices from the Thy1-ChR2 mice showed only three neurons in layer 6 (L6) which fired time-locked to the light stimulus. Otherwise, one neuron in L2/3 and one in L6 elicited delayed APs. One neuron in L4 and one neuron in L6 which were already spontaneously active, showed firing activity during the stimulus (n=9, L2/3; n=13, L4; n=23, L6). In electroporated mice, no evoked APs were detected (n=6, L2/3; n=7, L5) (**Fig. 3.5**).

3.4   Identification of Layer 5 Inputs

To map the connectivity between pre- and postsynaptic L5 populations, L5 pyra-
midal neurons were patched and filled with a fluorescent Ca^{2+} indicator and a
fluorescent volume marker (**Fig. 3.6**). Ca^{2+} signals upon light stimulation were
imaged as was shown to be possible by Zhang and Oertner (2007). Spines, in
which elevated Ca^{2+} signals were detected, were identified as input sites of presy-
naptic population (See Section 2.1). As L5 of the Thy1-ChR2 mice was populous
with wtChR2 expressing neurons, the postsynaptic cells were selected from those
with no visible yellow fluorescent protein (YFP) fluorescence under normal imag-
ing laser powers to minimize wtChR2 currents, which contributed to global Ca^{2+}
signals and impaired spine input identification process.

The size of the field of view was optimized to allow for simultaneous imaging
of Ca^{2+} signals from as many spines, meanwhile to be fast enough to resolve the
time course of these signals (5×19.8 μm at 10 Hz).

Figure 3.7a shows an acquisition from a trimmed tile (out of focus part
removed) over time, presented to demonstrate the raw data obtained during ex-
periments. Here, for the spines and the dendritic regions marked in the mor-
phology image, Ca^{2+} signals were acquired. The baseline frame shows the Ca^{2+}
fluorescence before the photostimulation, which immediately after the stimulus
(indicated with the blue line) increases. In the first time frame after the stimu-
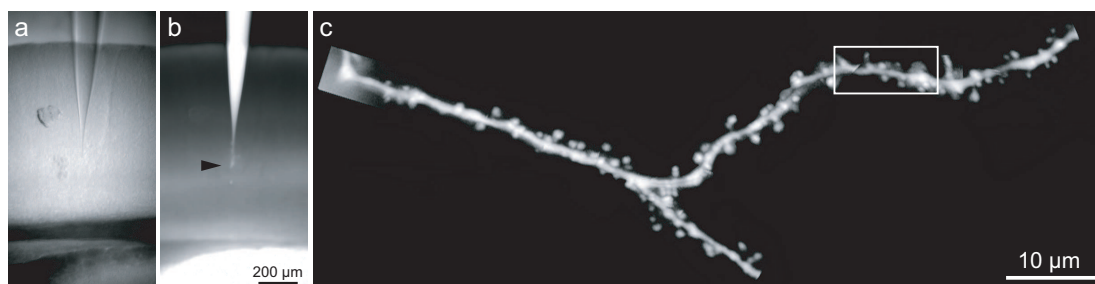
Figure 3.6: Postsynaptic L5 cell. (a) A postsynaptic cell in L5 is patched and
filled with Fluo-5F and Alexa 594. (b) YFP and Fluo-5F fluorescence show that the
soma of the neuron, marked with the arrowhead, resides within a dense basal dendrite
network. (c) Maximum z-projection from Alexa 594 fluorescence shows the segment of
the neuron that was mapped. Stretch enclosed by the rectangle is the tile in Figure 3.7.
Image is obtained by stitching the tiles from the experiment.

lus, elevated Ca^{2+} signals are visible in the spines (red boxes in the morphology image), which later spread into the dendrite. Towards the end of the acquisition, after 4 s, Ca^{2+} levels approach back to baseline levels. In the raw data, it is normal to observe apparently higher signals in the dendrite than that of the spines due to the larger volume of the dendrite, which contains to more fluorophores in the two-photon excitation volume. Therefore, the change in Ca^{2+} fluorescence (ΔG) was normalized to the volume marker (R) before comparing signals in spines to their closest respective dendritic region (black boxes). Normalized $\Delta G/R$ signals for the marked spines and dendritic regions at their bases from all acquisitions of this tile are plotted in **Figure 3.7b**.

To be able to decide from these traces whether spines received input, we had a simple assumption. The spine neck provides biochemical compartmentalization to the spine (Müller and Connor, 1991; Sabatini et al., 2002). Therefore, it is not expected to see a higher normalized Ca^{2+} signal in the dendrite when the source of Ca^{2+} is the spine. A spine was identified as receiving input when its signal peak was higher than of the signal at its base on the dendrite. If the peaks were comparable, then the spine peak had to occur earlier than the dendrite peak (see Section 2.10.2). Traces when the spines received input (**Fig. 3.7b**, round markers) clearly demonstrate this amplitude difference. When there is no input, the spine signal and the dendrite signal overlay with each other (traces with no markers). We also looked at the signal of the volume marker and confirmed that the acquisitions did not induce photobleaching (**Fig. 3.7c**).

It can also be argued that a global Ca^{2+} spike might contaminate the measurements. This was addressed by analyzing the propagation of the Ca^{2+} signal in the whole stretch of the dendrite. **Figure 3.8** shows for the tile in Figure 3.7, that dendritic signal elevation starts locally and spreads over the whole stretch over time, suggesting that if this was a spike, then it is likely a local NMDA spike (Antic et al., 2010), rather than a global Ca^{2+} spike. Additionally, the origin of the signal corresponds to where the identified inputs are.

We progressed along the basal dendrites of L5 pyramidal cells of Thy1-ChR2 and systematically acquired tiles to be able to measure responses from every single

spine on the dendritic stretch. In total, 157 of the 1436 analyzed spines were identified to be receiving input from L5 presynaptic neurons (identified fraction, 10.9%, n=13 cells). To be able to display them altogether on entire branches, tiles were stitched together to get an overall image of the branch. **Figure 3.9** displays all of the spines of the dendritic branch in Figure 3.6c, receiving input from L5.

We checked the reproducibility and the reliability of the input identification method. Approximately 65% of the identified input sites (with at least three trials) showed a response to the light stimulus more than once. The mean success rate was 46.1% for these inputs (**Fig. 3.10**). The performance of the response detection algorithm was also evaluated. We gave our subjective decision for each
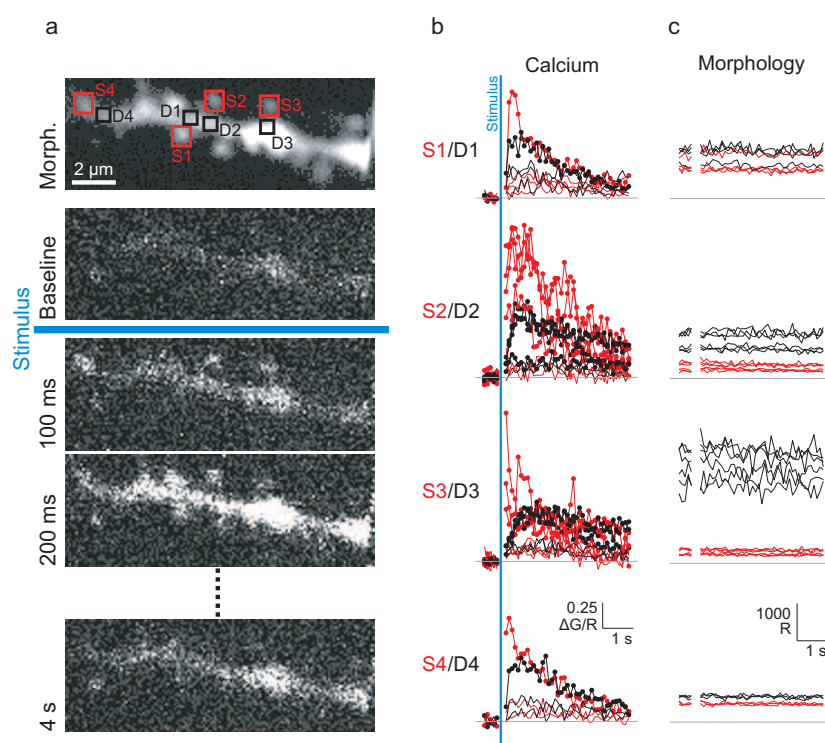
Figure 3.7: Fluorescence signals recorded from an experimental tile. (a) Morphology and time-lapse images of an acquisition from the tile, marked with the rectangle in Figure 3.6c, presented as raw data. Time of the photostimulus is shown with the horizontal blue line. The spines and the dendritic regions, whose traces are shown in b and c, are marked and labeled in the morphology image (red, spines; black, dendritic regions). (b) Calcium (ΔG/R), and (c) volume marker (R) signals from the ROIs shown in a. Traces with round markers in b belong to the acquisitions when the spines were identified as receiving input. Other traces, when the spines failed to show responses.
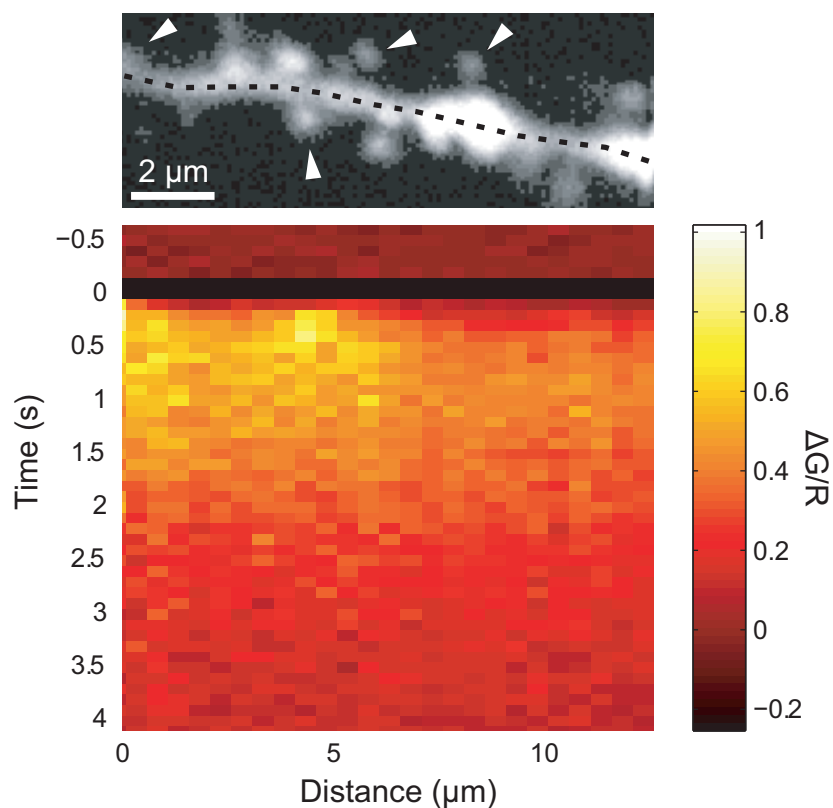
Figure 3.8: Ca²⁺ signal propagation in the dendritic stretch. The Ca²⁺ signal in the whole dendritic stretch of the tile in Figure 3.7 is aligned with structural data. Signal is retrieved along the trace (dashed line), with 0.6 µm bilateral extension and 0.5 µm binning along the trace. The black horizontal line in the distance-time plot is the stimulus frame. Color map codes for signal amplitude (ΔG/R). Spines receiving input are marked with arrowheads.
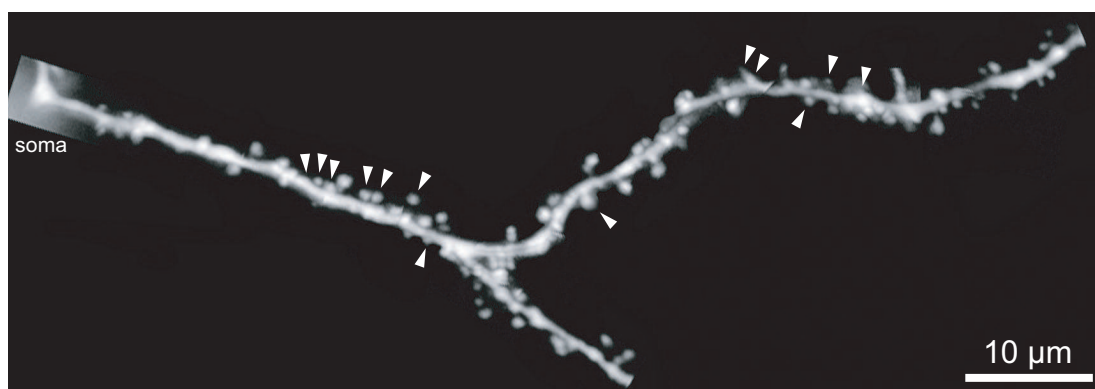

Figure 3.9: Dendritic branch with the spines receiving input from L5. Arrowheads mark the input sites. Image was obtained by stitching the tiles from the experiment.
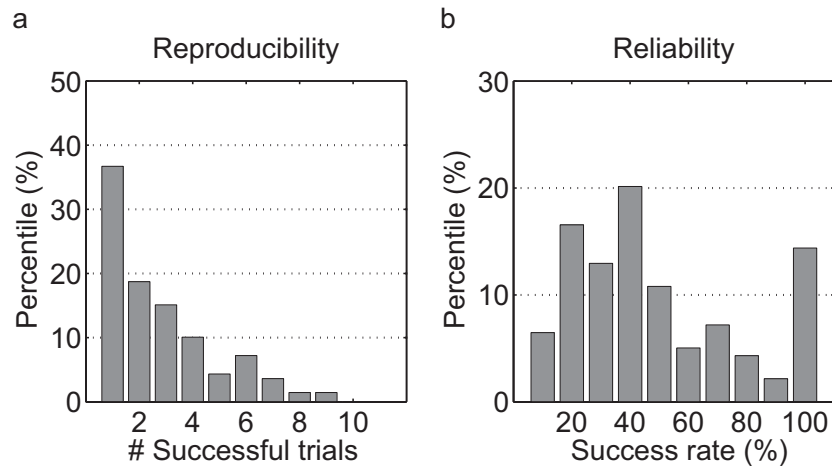
Figure 3.10: Reproducibility and reliability of the identification method.
~65% of the spines receiving input showed light evoked responses more than once (a).
These spines showed response on average 46.1% of the trials (b). Graphs were drawn
from spines with at least three trials (n=139).

trace, whether there was a response or not. The traces were labeled as ambiguous
when it was not straightforward to decide. In the individual traces (n=6949
acquisitions), the total discrepancy between human decision and the algorithm
was 1.91%, of which, from the human perspective, 0.72% were false negatives,
0.33% were false positives and 0.86% were ambiguities. The discrepancy in the
individual traces translated to the overall input identification (n=1436 spines)
by 3.92% total discrepancy, where 0.56% were false negatives, 1.12% were false
positives and 2.24% were ambiguities. Most of the false positives emerged from
the spines with low fluorescence intensity, i.e. small or out of focus spines, hence
more noise. False negatives were usually due to the signals with very fast decay.
Further analyses were conducted with the human corrected results.

The signal amplitudes of the spines with identified L5 input in successful
acquisitions were found to be significantly higher than the corresponding signals
at their bases on the dendrite (**Fig. 3.11**). Cumulative plots describe these
amplitude differences in detail (**Fig. 3.12**). For the spines with identified input,
all successful acquisitions showed signals with higher amplitude in the spines than
in the dendrites, whereas in failures, the signal amplitude in the spines was very
close to those in the dendrite, or the signals in the dendrite had higher amplitude.
The same relationship as in failures was observed for the spines with no identified
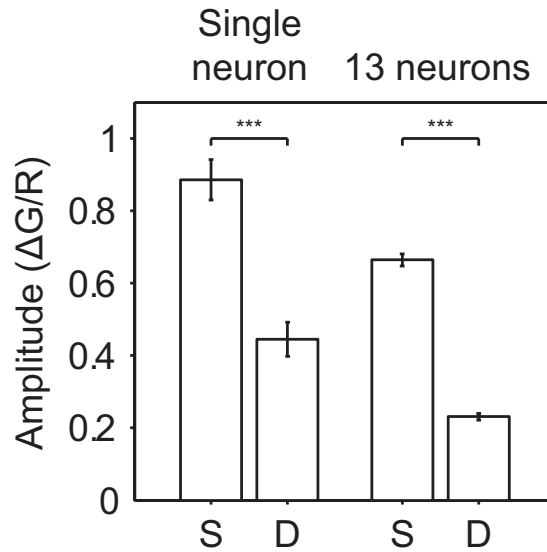
Figure 3.11: Spine and dendrite mean peak signal comparison. Mean peak signal amplitude of the spines with identified input (S) and of their dendritic base (D) from the branch in Figure 3.9 (left) and from all experiments (right, n=13 cells) are compared. For this branch, mean peak $\Delta G/R=0.89\pm0.06$ for the spines, and mean peak $\Delta G/R=0.44\pm0.05$ for the dendrite (p<0.001 two-sample two-tailed t-test, n=13 spines), and from all experiments, mean peak $\Delta G/R=0.66\pm0.02$ for the spines, and mean peak $\Delta G/R=0.23\pm0.01$ for the dendrite (p<0.001 two-sample two-tailed t-test, n=157 spines). Error bars represent standard error.

input.

The average τ_{decay} of the traces identified to be responses was calculated from exponential fits to be 1.89 ± 0.09 s (n=434). Hence, the 10 Hz image frame rate used in these experiments was proven to be adequate to catch these signals. These are rather slow signals and do not reflect physiological conditions, where τ_{decay} for spines was reported to be 12 ms (Sabatini et al., 2002). We used an intermediate affinity Ca^{2+} indicator (Fluo-5F, K_d=2300 nm) at a high concentration (1 mM) to be able to increase the Ca^{2+} detection sensitivity, which also dominated the endogenous Ca^{2+} buffering.

3.5 Morphological Comparisons

The morphological properties of the spines with L5 input were compared to those of the spines without any detected input. No significant differences were observed in the volume or the length of the spines between these two populations

(**Fig. 3.13**). It should be pointed out that the spines without identified input also contains L5 inputs which were not detected. This contamination from unidentified L5 inputs could be diluting the results, and might be occluding a difference, if it exists.

3.6 Spine-Dendrite Signal Coupling

We analyzed the spine-dendrite signal coupling in the acquisitions when the spines received input with an anticipation to see a reverse correlation between the spine length and the signal coupling, based on the evidence that spines are biochemical compartments facilitated by the spine neck (Müller and Connor, 1991; Sabatini
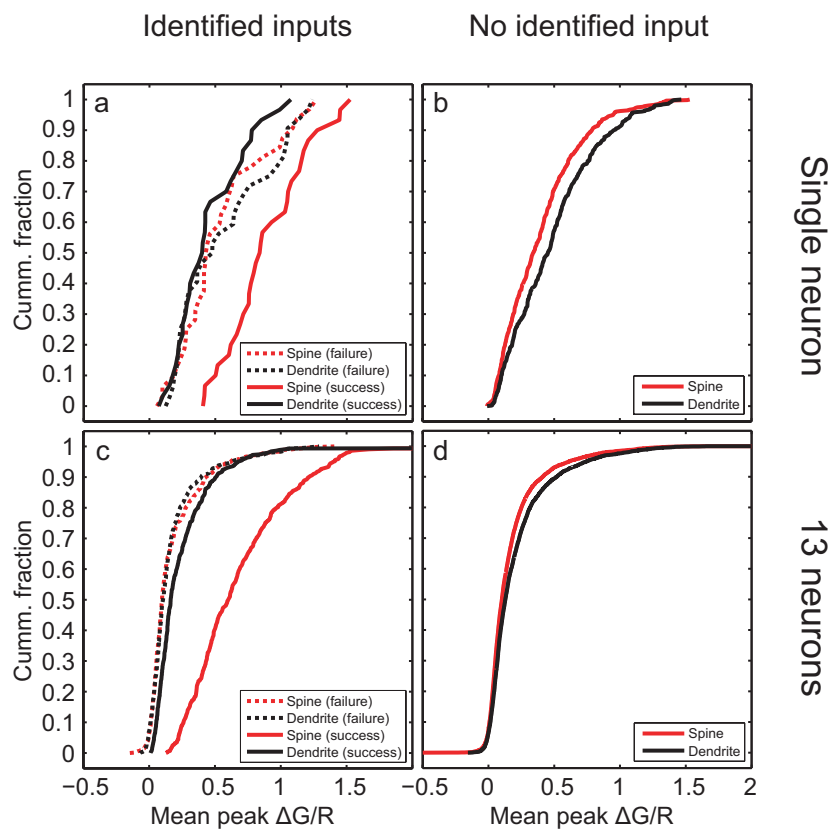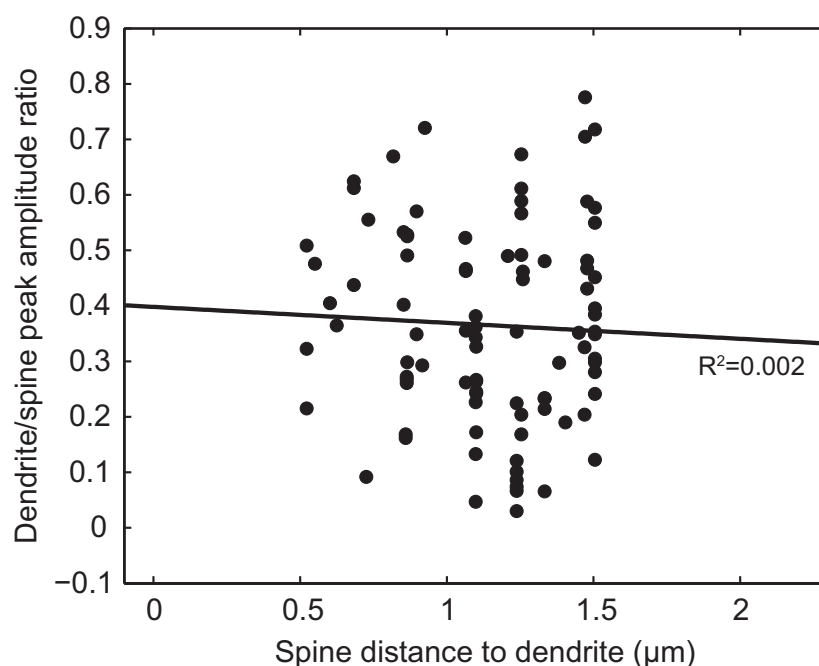

Figure 3.12: Spine and dendrite mean peak signal comparison (cumulative). Cumulative plots for the mean peak signal, for the spines with identified L5 input in the branch in Figure 3.9 (a), and in all experiments (c). Successful acquisitions (solid lines) and failures (dashed lines) are shown for the spines (red) and their bases on the dendrite (black). In successes spine signals are higher than dendrite signals, whereas in failures both signals overlay each other. Cumulative plots for the spines with no identified input show in the branch in Figure 3.9 (b), and in all experiments (d), that the signals from the dendrite (black) are higher than the signals from the spines (red).
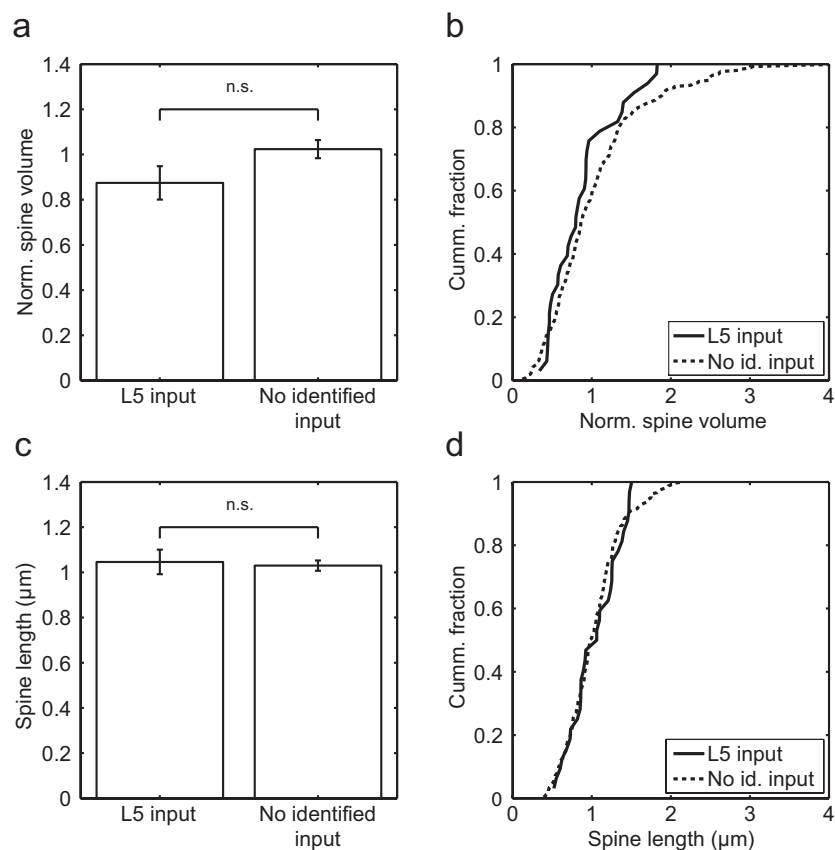
Figure 3.13: Morphological comparisons between the spines with identified L5 input and with no identified input. (a) Mean normalized volume of the spines with identified L5 input (0.87±0.07, n=24 spines) and the spines with no identified input (1.02±0.04, n=273 spines) show no significant difference (p=0.19, two-sample two-tailed t-test). Spine volumes were normalized to the mean spine volume for the segment (dendritic stretch between branching points). (b) Cumulative distribution of normalized spine volumes for the two spine populations, with identified L5 (solid) and no identified (dotted) input. (c) Comparison of mean spine lengths also show no significant difference between the spines with identified L5 (1.05±0.05 μm, n=23 spines) and no identified input (1.03±0.02 μm, n=255 spines) (p=0.80, two-sample two-tailed t-test). Spine lengths are z-projected approximate lengths. (d) Cumulative distribution of spine lengths, for spines with identified L5 (solid) and no identified input (dotted).

Figure 3.14: Spine-dendrite signal coupling depending on spine length. The ratios of dendrite mean peak amplitude to spine mean peak amplitude are calculated for each successful acquisition of a spine receiving input. Spine lengths are measured from z-projection of morphological stacks. Regression analysis does not show a correlation between signal coupling and spine length (R^2=0.002, n=72 acquisitions from 48 spines).

et al., 2002). However, such an effect of the spine length on the spine-dendrite coupling was not observed (**Fig. 3.14**).

This contradiction could be explained by various aspects which were not analyzed, such as the width of the spine neck, which also contributes to the signal compartmentalization, and the Ca^{2+} extrusion mechanisms (Sabatini et al., 2002). Additionally, the dendrite signals had in most of the cases multiple sources (multiple activated inputs), which invalidated the comparison. Furthermore, the measured length of the spines were z-projected 2D approximations, which might have occluded the results.

3.7 Spatial Organization of Layer 5 Inputs

The most interesting findings of this study were revealed by analyzing the spatial organization of the inputs. We simplified visualization of the input maps by migrating from marked two-photon images to 'dendrograms', which enabled a clearer glimpse of the data. For every branch mapped, the dendritic segments were traced to obtain a representative 3D reconstruction. These reconstructions made it possible to extract order and distance information of the spines along the dendrite. First, order-based dendrograms were generated, where the distances between schematized spines were in number of neighbors. **Figure 3.15** shows the order-based dendrogram for the branch in Figure 3.9 (refer to Appendix A.1 for order-based dendrograms of all cells). Even without any analysis, apparent clustering of spines with identified input was observable.

We analyzed the distribution of order-based nearest neighbor distances of the spines with identified input from all the mapped branches to investigate the existence of clusters. In doing so, a standard dataset was required to compare the experiments to. The best approach in this case was to compare the experimental data to simulated data from random input maps. Then, any significant difference would have meant that the spines with identified input in the experimental data were not randomly scattered on dendritic branches, but rather they had a non-random spatial organization. Surrogate branches were generated by keeping the total number of spines and the number of inputs constant, independently for every branch simulated, and by randomizing the assignment of inputs to the spines.
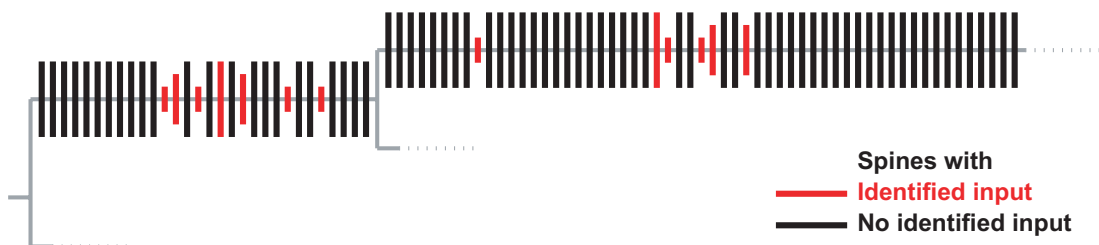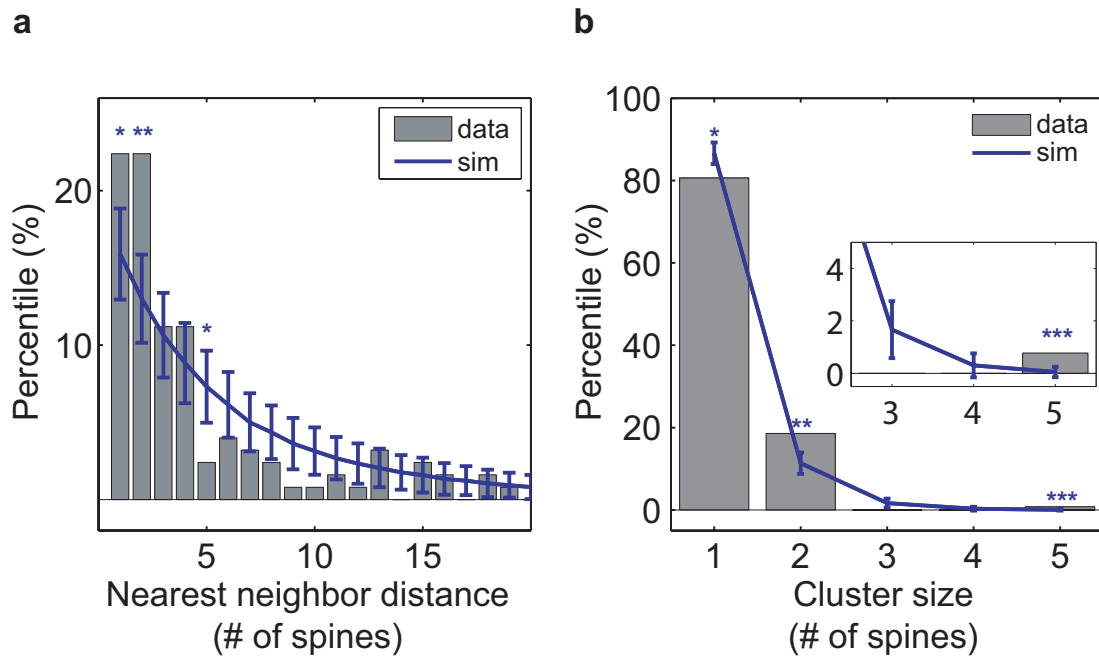

Figure 3.15: The order-based dendrogram for the branch in Figure 3.9. Spines with identified input are marked with red. Different lengths these spines represent their success rate in three steps: 0-33%, 33-66% and 66-100%. The spines with no identified input are black. Dashed lines indicate branches not mapped.

For each simulation instance, the distribution of order-based nearest neighbor distances was computed the same way that was done for the experimental data. Repetition of the Monte Carlo simulation 1000 times provided the percentile distribution for random cases of each order-based distance represented in the histogram. Comparison of the experimental findings to the simulations revealed that there were significantly more spines with identified input that were either immediate neighbors (nearest neighbor distance=1), or had only one spine in between that showed no response (nearest neighbor distance=2) (**Fig. 3.16a**). This finding provided numerical evidence for the observed proximity between the spines with identified input.

From a different perspective, we wanted to know how this applied to the size of clusters formed by immediate neighbors. A similar comparison of experimental data to Monte Carlo simulations revealed significantly less 'loner' spines (no neighbor with input, cluster size=1), but more neighbor pairs (cluster size=2) than what would have been expected if spatial organization of the inputs were random (**Fig. 3.16b**), similarly suggesting the existence of a proximity.

Order-based analysis provided an initial insight into the data, however real distances needed to be analyzed to be able to relate the findings to a framework where they could be applied to dendritic integration studies. **Figure 3.17** shows the refined dendrogram of the same branch, in real distances (refer to Appendix A.2 for distance-based dendrograms of all cells).

The same approach as in the order-based neighborhood analysis was used to assess real distance relationship between the spines with identified input, but with a single representational difference. In order-based analysis, distances were always integers, which then did not require any binning to plot and analyze the distribution, however this was not the case with distance-based analysis. Therefore, the experimental data was compared to the simulated data with cumulative distributions to avoid binning. Similarly, random dendritic branches were generated, keeping the location of spines constant and randomly assigning the same number of inputs to these preserved locations. **Figure 3.18** shows the cumulative distribution of nearest neighbor distances of all spines, of the spines with identified
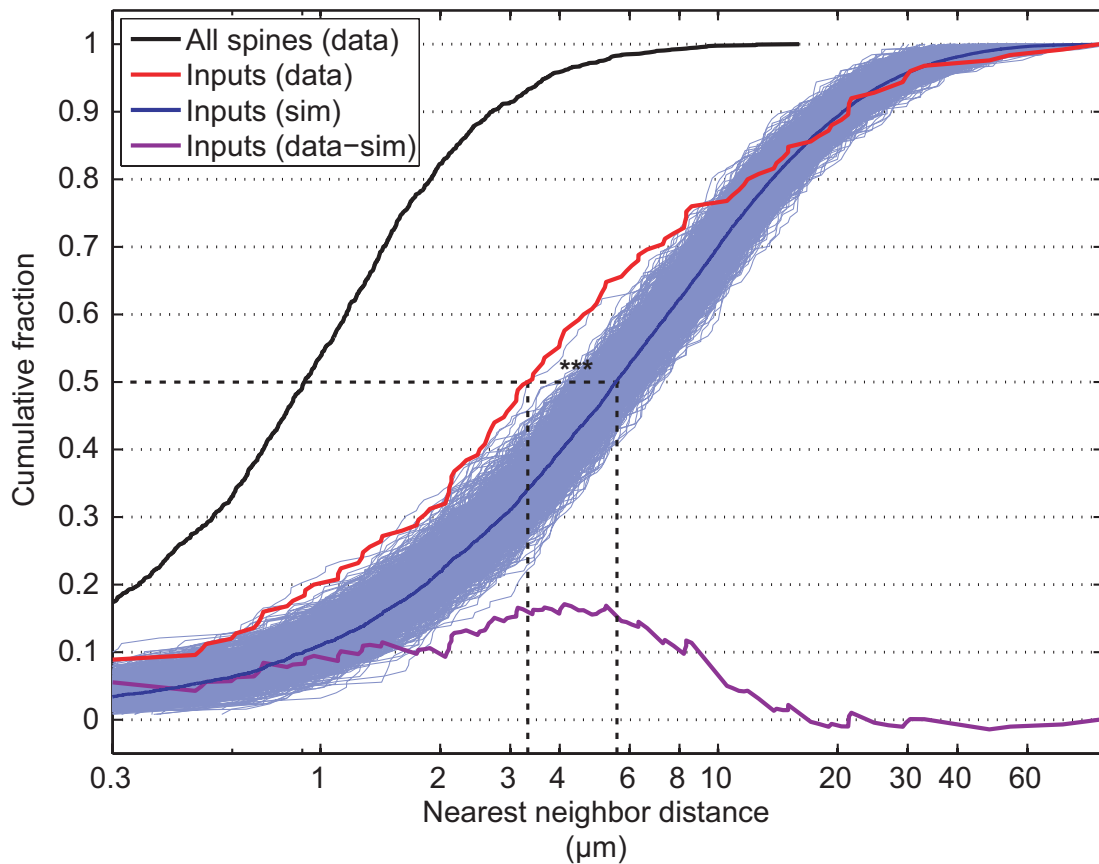
Figure 3.16: Order-based comparison of data to Monte Carlo simulations.
(a) Distribution of order-based nearest neighbor distances of spines with identified input, from experimental data (bars), and from Monte Carlo simulations (blue plot, n=1000 simulations). (b) Distribution of sizes of immediate neighbor clusters, from experimental data (bars), and from Monte Carlo simulations (blue plot, n=1000 simulations). Error bars are standard deviation. (*, p<0.05; **, p<0.01; ***, p<0.001, z-test)
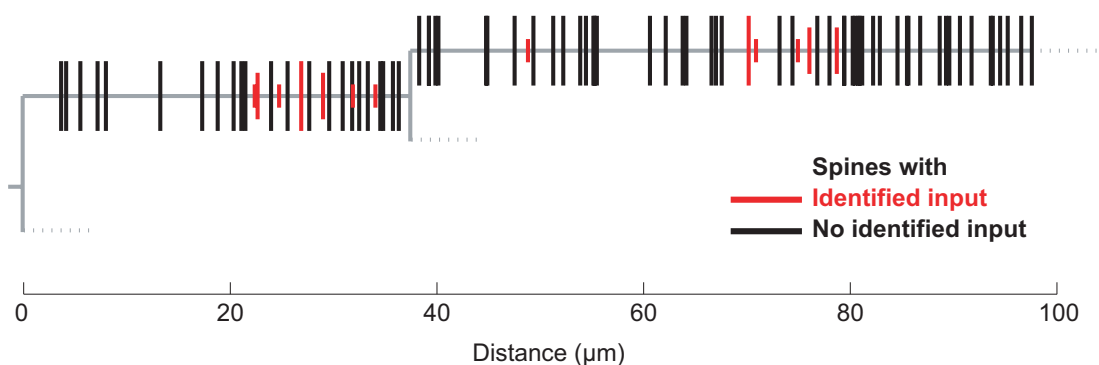
Figure 3.17: The distance-based dendrogram for the branch in Figure 3.9.
Spines with identified input are marked with red. Different lengths of spines with input represent their success rate in three steps: 0-33%, 33-66% and 66-100%. The spines with no observed response are black. Markings that appear thick are multiple spines which are very close to each other, whose markings could not be separated in this scale. Dashed lines indicate branches not mapped.

input, and of the simulated inputs. The distribution from all spines provides a minimum baseline for the other two distributions. This analysis also exhibited that the distances between the spines with identified input from experiments to be smaller than the random case expectations. Comparison of median values of data (3.42 μm) and simulations (5.55 μm) revealed a significant difference (p=0.0001, z-test). Distribution of inputs from experiments differed from simulations more for distances below ~10 μm.


Figure 3.18: Distance-based comparison of data to Monte Carlo simulations. Cumulative distributions of real distance-based nearest neighbor distances of all spines (experimental data, black), and of spines receiving L5 input (experimental data, red; Monte Carlo simulations, mean, blue; individual simulations, pale blue, n=1000 simulations; experimental data and simulation difference, purple). Median inter-input distance is 3.42 μm for the experimental data, and 5.55±0.56 (standard deviation) μm for the simulations. The median difference is highly significant (p=0.0001, z-test)

3.8   Detected Clusters and Their Properties

The results presented so far suggested the proximity of identified inputs with distances smaller than to be expected if they were randomly scattered on dendritic branches. This also suggests that these detected inputs could be clustered. As pointed out above, inter-input distances of experimental data deviated most from simulations below ∼10 μm. Also, it was shown in the context of long-term potentiation (LTP) that synapses could influence induction of plasticity of their nearby neighbors within 10 μm (Harvey and Svoboda, 2007). Furthermore, Takahashi et al. (2012) and Kleindienst et al. (2011) observed spontaneously active inputs that had synchronized activity to be within about 10 μm to each other. Therefore, we searched for patterns of identified input with an assumption that two spines within 10 μm to each other belonged to the same cluster.

We calculated the occurrence likelihood of detected patterns by permuting all pattern possibilities for a segment given the branch parameters, i.e. spine locations and the number of inputs, and finding the percentile of similar patterns (same or less length, same number of inputs). We chose a likelihood threshold of 2% to decide if a particular pattern was a cluster or not. Also, patterns needed to have at least three inputs to qualify as clusters. **Figure 3.19** shows the result of this analysis for the branch in Figure 3.9 (refer to Appendix A.2 for dendrograms with cluster analysis of all cells).
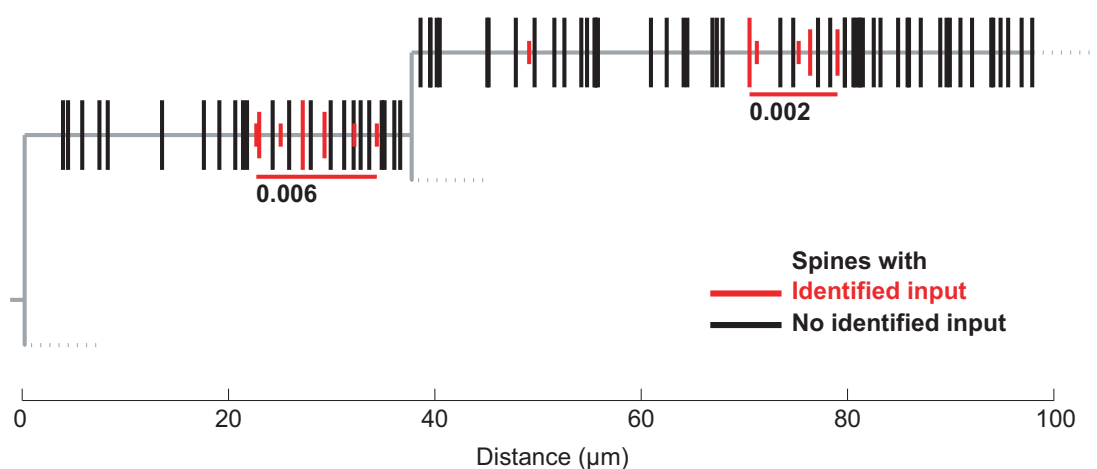
Figure 3.19: Detected clusters and their likelihood scores. The values under marked clusters are the likelihood scores.
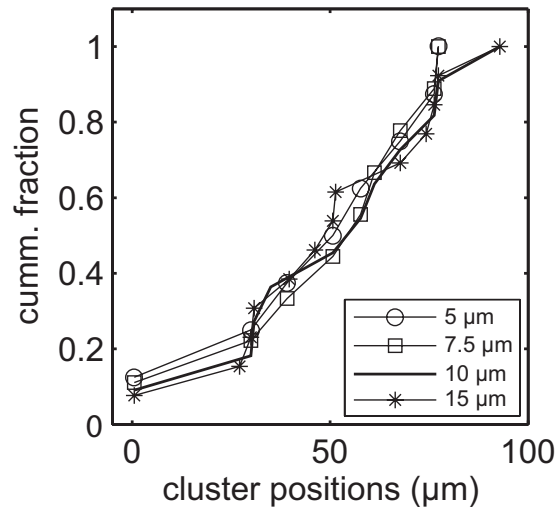
Figure 3.20: Cluster positions. Cumulative plots show the distribution of the cluster positions as the distance from the soma. Cluster location is its center of gravity. Different plots are results with different distance criteria (5, 7.5, 10, 15 μm).

In total 31 patterns were identified that met the distance criterion (10 μm). Of those, 11 patterns detected in 9 cells fulfilled the cluster definition (likelihood≤0.02, inputs≥3). These detected clusters had a mean length of 11.44±3.17 μm. They received input from 6.09±1.00 spines, corresponding to an input density of 0.75±0.17 spines/μm, and a packing ratio[1] of 0.48±0.04. The mean likelihood of clusters was 0.007±0.002. They did not have a spatial preference on dendritic segments, which is seen from the linearity in the cumulative distribution of their positions based on their center of gravity (**Fig. 3.20**, thick line).

Although the distance criterion had physiological basis, we still verified the sensitivity of cluster detection to different distance criteria (5, 7.5 and 15 μm). The potential effect of having a larger interaction distance was that (i) nearby clusters could merge, or (ii) detected clusters might gain more inputs, or, less likely, (iii) new clusters could be detected from sparsely distributed inputs. **Figure 3.21** displays some of the properties we compared with different distance criteria. As expected, longer clusters were detected with higher distance criteria (b). Likelihood distribution of detected clusters (a) did not differ very much, but there was a trend that with higher distance criteria detected clusters

---

[1]packing ratio is the ratio of the number of inputs to the total number of spines in the cluster.

scored worse. The input density (c) or packing ratio (d) of the detected clusters was less for the clusters detected with higher distance criteria, possibly due input dilution. The positions of detected clusters differed only slightly (**Fig. 3.20**), since new inputs added to the existing clusters with increased distance criteria could only influence the center of gravity of clusters to a certain extent. Overall, there were some differences, most with 15 µm distance criterion. Other distances did not yield radically different results. Therefore, the detection algorithm showed robustness to distance criteria between 5-10 µm.

We investigated the input cooperativity in clusters by visually analyzing coactivated spines in individual acquisitions. Previously, Harnett et al. (2012) demostrated that multiple coactivated spines exhibited input cooperativity which was detected by higher than expected EPSPs. In our experiments, the peak amplitudes of the input signals did not correlate with the number of successes in the acquisitions, hence did not reveal any cooperativity in terms of Ca^{2+} influx (**Fig. 3.22**, refer to Appendix A.3 for all examples).
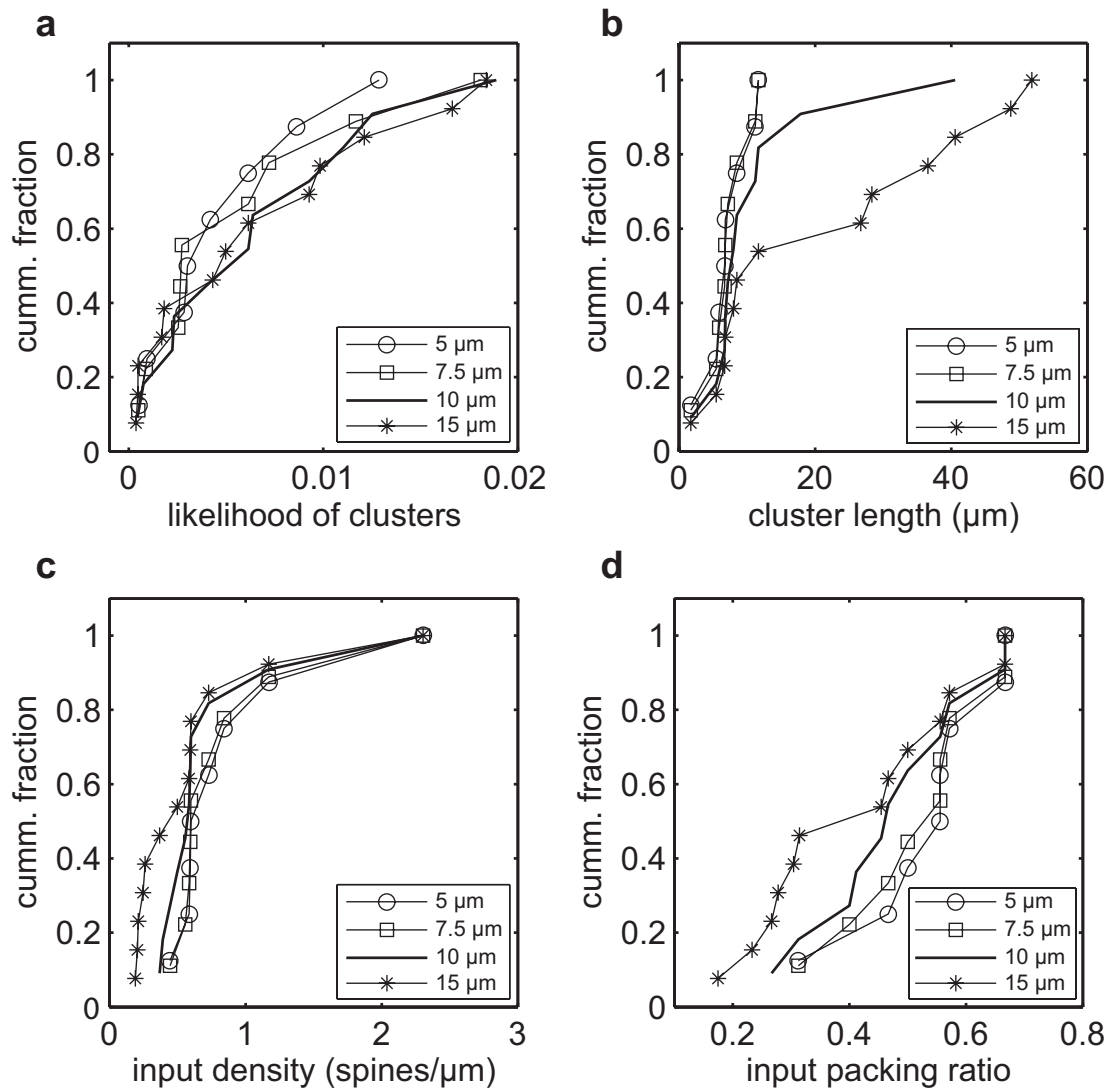
Figure 3.21: Cluster detection sensitivity to distance criteria. Outcomes of analyses with different distance criteria (5, 7.5, 10, 15 μm) shown as cumulative plots for comparison of (a) likelihood of clusters, (c) cluster length, (c) density of inputs in clusters, and (d) packing ratio of clusters.
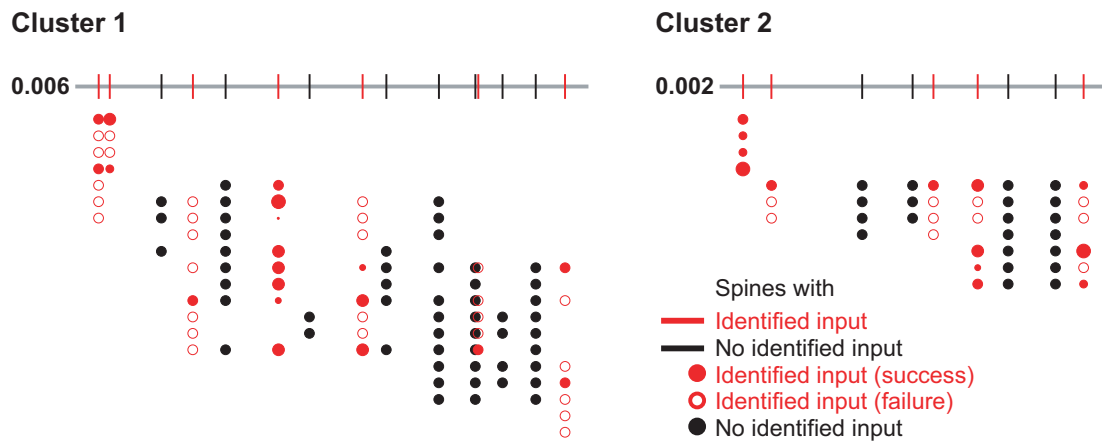
Figure 3.22: Spine cooperativity in clusters. Clusters from Figure 3.19 are shown with activity of their spines over different acquisitions (rows of circles). Red circles represent spines with identified input, with the size of filled circles representing peak $\Delta G/R$ amplitude of an input normalized to its mean, and open circles representing failures (no response detected in the acquisition). The fixed size of the open circles represent the mean peak amplitudes. Black circles correspond to the spines with no identified input. Likelihood scores are shown next to the clusters.

3.9   Identification of Layer 2/3 Inputs

We attempted to map the connectivity between presynaptic L2/3 and postsynaptic L5, with the intention of comparing the outcome of this second dataset with the mapping results shown above. We used the same approach to identify the spines receiving input from L2/3 (**Fig. 3.23**). We were able to demonstrate that in principle the technique could still be applied to mice obtained from a different genetic targeting method (IUE), using a different variant of ChR2 (hChR2(H134R)), and stimulating with a different protocol (local axonal stimulation).

Analysis of this dataset was performed as described for the previous dataset. No clusters were detected in this particular branch, which was expected since not many spines were identified (**Fig. 3.24**).
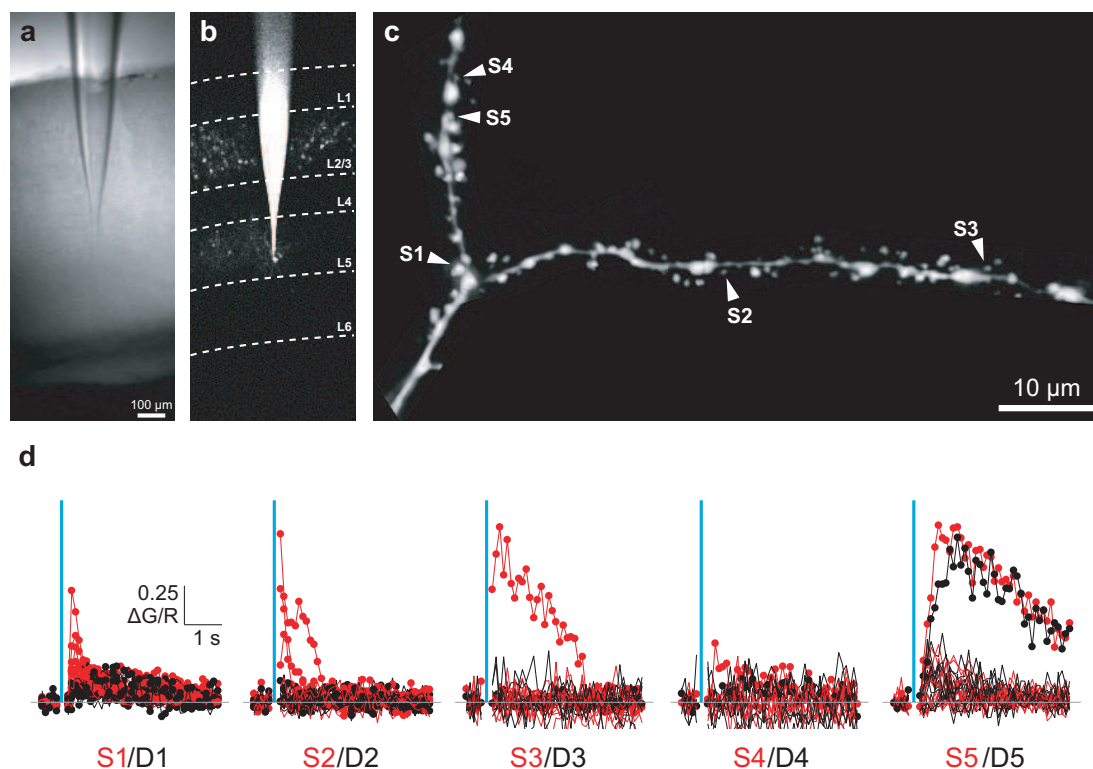
Figure 3.23: Identification of L2/3 inputs. (a, b) Location of the experimented neuron. Layers of the cortex are outlined. (c) Identified inputs from L2/3 are marked with arrowheads and labeled. (d) Calcium (ΔG/R) signals from spines shown in c and from their bases on the dendrite. Traces with round markers are from acquisitions when spines were identified as receiving input. Other traces represent when spines did not respond.
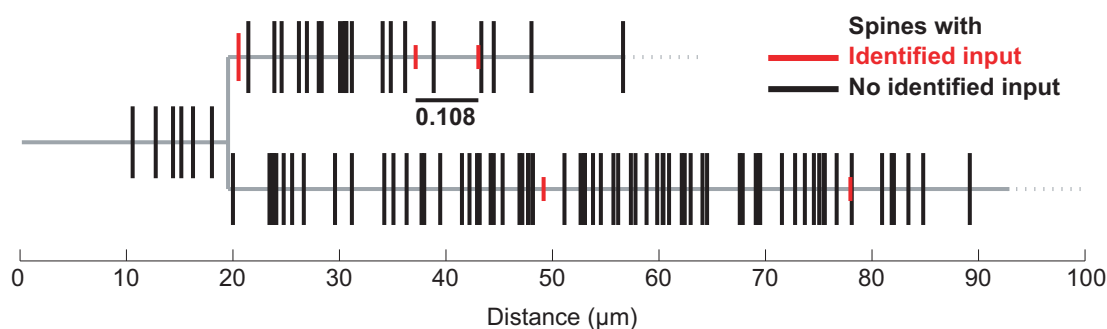
Figure 3.24: Cluster analysis for L2/3 inputs. No clusters were detected for the branch. The pattern analyzed is marked with black bar on the distance-based dendrogram, with the likelihood score shown beneath.

Unfortunately, any further analysis was not possible due to a lack of data. It should be stressed that the experiment demonstrated here for L2/3 to L5 connectivity is the only experiment in which multiple responding spines were detected. In other cases, either no spines or only a single spine were detected. We were persistent to get this dataset. In total, 101 mice were prepared (from ~110 surgeries, excluding mice for control and optimization experiments) with relatively high transfection and precise V1 targeting, of which 25 had especially dense transfection.

Optimization for the stimulation protocol concentrated on how efficiently presynaptic ChR2 expressing neurons were driven to fire APs. We checked the effect of the stimulus on the postsynaptic electrical currents, and investigated whether it could be possible to increase the input to the postsynaptic neurons by increasing the pulse width of the stimulation. In addition to the stimulus used in the experiments (3×5 ms pulses), a single 33 ms pulse and a single 66 ms pulse were tested, with reduced or open field aperture (**Fig. 3.25**). With reduced field (local axonal stimulation), we did not observe any difference between stimuli in terms of peak postsynaptic current and total driven charge. Wide field stimulation yielded higher currents as expected, since a wider area meant more axonal segments being stimulated, thus more contacts activated.

Another possibility for the high rate of undetected inputs could have been if contacts between L2/3 and L5 had less NMDAR, therefore the spines receiving input were not resolved with our method. We measured AMPAR and NMDAR

a

b
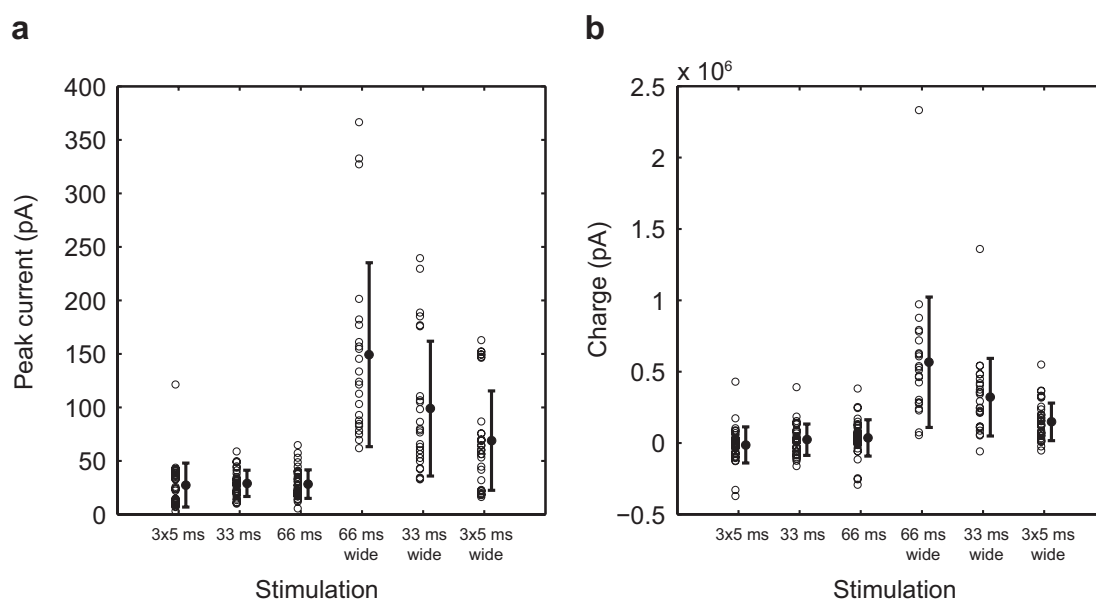
Figure 3.25: L5 postsynaptic currents under different L2/3 photostimulation protocols. Peak current (a), and total charge (b) in L5 postsynaptic cells under different L2/3 photostimulation protocols (3×5 ms, 33 ms and 66 ms pulses, with reduced or open field aperture). Open circles, individual measurements; filled circles, mean values; error bars, standard deviation (n=8 cells).

currents and compared our findings to what has been shown for pyramidal neurons in hippocampus (Scheuss and Bonhoeffer, 2013); we did not observe any lack of NMDAR (**Fig. 3.26**).

Finally, we compared electrophysiological recordings of mapping experiments from Thy1-ChR2 and electroporated mice. As expected, the peak current and the total charge was significantly higher in the Thy1-ChR2 dataset (**Fig. 3.27ab**). This was easily explained by the fact that more inputs could be identified in the Thy1-ChR2 dataset, and also more inputs were expected to be activated simultaneously since the stimulus was delivered with an open field aperture. The mean traces from the two datasets also show this difference between the light evoked postsynaptic currents (**Fig. 3.27c**).

There was another striking difference between the postsynaptic currents from the two datasets. **Figure 3.27c** shows that IUE trace has a rapid onset and decays much faster than the Thy1-ChR2 trace. It also has a shoulder, as indicated by the arrowhead, which suggest the postsynaptic currents from electroporated mice might have a fast and a slow component. This shoulder coincides with the
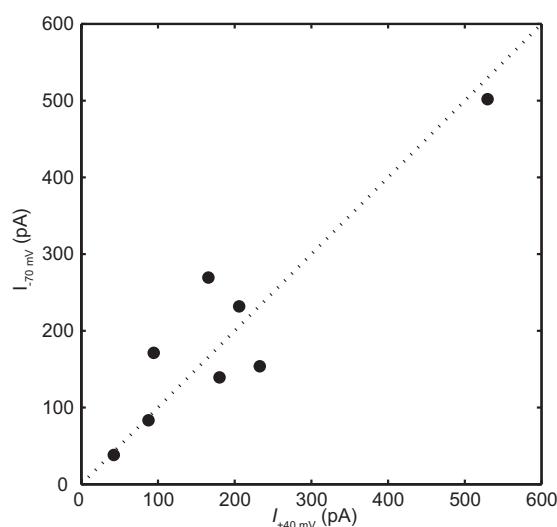
Figure 3.26: AMPAR and NMDAR currents in L2/3 inputs. AMPAR (-70 mV) versus NMDAR (+40 mV) currents line on the equality (dotted line) (n=9 cells).

peak of the current in Thy1-ChR2 mice. The Thy1-ChR2 trace only shows a slow activation and deactivation.

Different subtypes of NMDARs have different kinetics. NMDARs consisting of GluN2B subunits have lower conductance but a slower deactivation, where, for instance, those with GluN2A subunits have much larger currents, but a very fast decay. Both of these subunits are expressed by cortical neurons in adults (Paoletti et al., 2013). Recruiting different variants of NMDARs with different abundance could explain the difference in the kinetics of the postsynaptic currents between the two datasets. At this point, this is merely a speculation, however, also, an interesting outcome to investigate. Such a difference could also explain why our attempts to map inputs from L2/3 failed. It could be possible that the Ca^{2+} signals at these inputs were faster than what can be resolved, and that we could only detect the Ca^{2+} signals from a slow component.

In summary, we could not map L2/3 inputs on basal dendrites of L5 pyramidal cells in electroporated mice. There might be different reasons for this result. One would be that IUE yields sparse transfection even in the most efficient outcome and is not therefore suitable for mapping experiments. Another possibility could be that L2/3 does not make connections in the proximal segments of basal
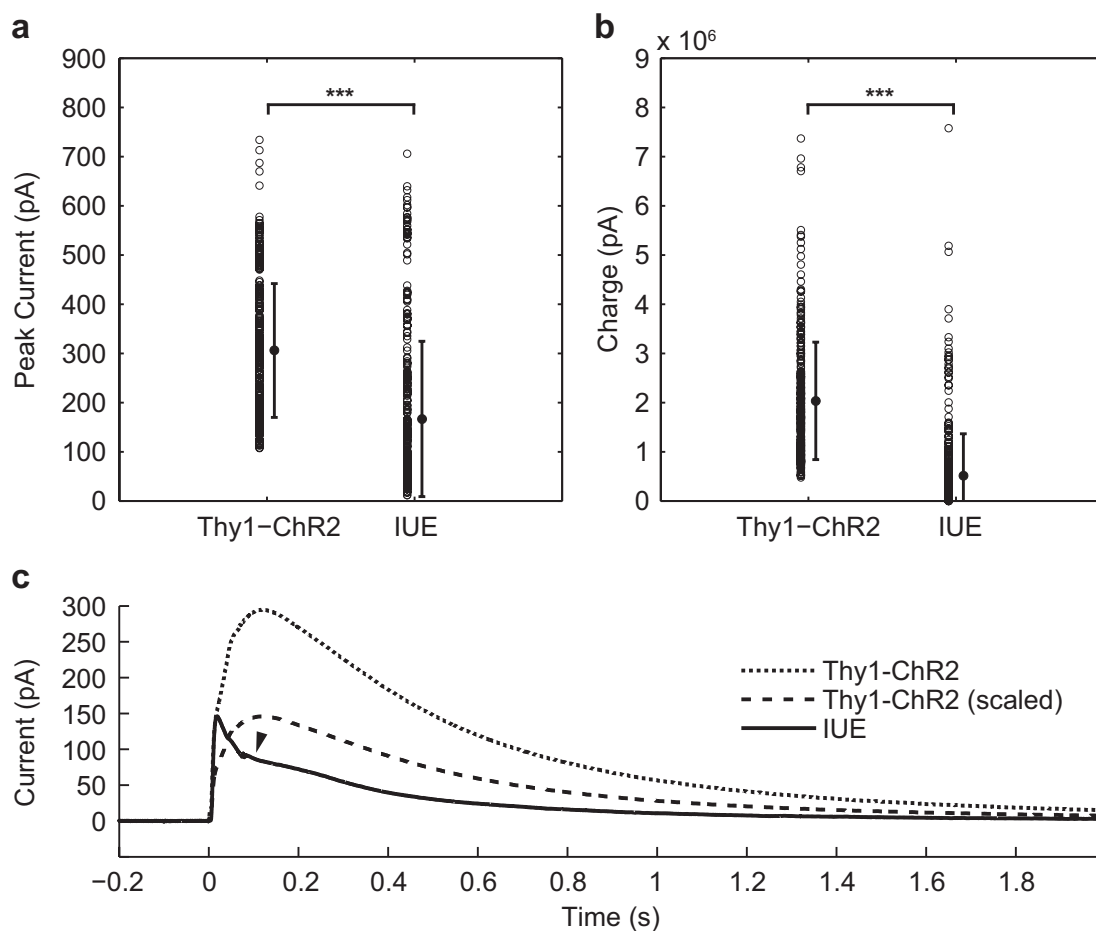
Figure 3.27:   Comparison of postsynaptic electrical currents from Thy1-ChR2 and electroporated mice. Comparison of (a) peak electrical current, and (b) total charge upon photostimulation in Thy1-ChR2 and electroporated mice (open circles, individual measurements ; filled circles, mean values; error bars, standard deviation. ***, p<0.001, two-sample two-tailed t-test, n=5 cells for each set). (c) The mean current traces from Thy1-ChR2 (dotted) and electroporated (solid) mice. Dashed trace is the scaled down mean trace of Thy1-ChR2. The arrowhead marks the shoulder in the trace from electroporated mice.

dendrites, where we did our mapping, but this would contradict what Petreanu et al. (2009) showed previously, where L5 pyramidal neurons in mouse barrel cortex received L2/3 input on proximal basal dendrites.

Chapter 4

Discussion

In this study we aimed to develop a new method for connectivity mapping, where the functional inputs between specific neuronal populations could be identified at synaptic resolution. This technique was applied to map the connectivity between postsynaptic L5 neurons and presynaptic L2/3 and L5 neurons. We were able to detect inputs and obtain systematically acquired input maps. The experimental data provides evidence that the inputs from L5 to L5 are clustered. Mapping of L2/3 inputs onto L5 was not successful under the conditions tried.

Overall, the method shows promise to complement existing connectivity mapping efforts, even more so with possible further improvements.

4.1 Effects of Undersampling of Inputs

There are multiple reasons to expect false negatives when using this method. Not every presynaptic cell is expected to be transfected, or if it is, a uniform expression level could be hard to achieve. It is an *in vitro* technique, requiring slicing of the brains which inflicts damage to the tissue and "broken inputs" as a consequence. Those cells which survive slicing still face stress *ex vivo* and tissue degrades in quality over the course of experiments, further contributing to nonviable inputs. It was shown that axonal photostimulation was possible in electroporated mice with hChR2(H134R), which in principle eliminates the necessity of having somata in slices. However, it was not verified whether severed axonal segments survived, or if they did, it was not characterized how long they could. Moreover, those cells which require somatic photostimulation to fire APs might fail to display their

inputs if their axons are severed during slicing.

We could stimulate neurons with ChR2 only to a certain limit. It was shown earlier in this report that cells, both from Thy1-ChR2 and electroporated mice, could not be driven to fire without failures. Considering not every AP yields vesicle release as characterized by the release probability (Borst, 2010), failures to drive the cells reliably will eventuate failures in synaptic transmission and consequently in "hidden inputs". Furthermore, not every synaptic event is expected to trigger the same postsynaptic influx due to the different molecular composition and/or state of the synapses (Marder and Goaillard, 2006). Then, some inputs could remain under the detection limit of the method.

This method relies heavily on the removal of Mg^{2+} blocks from NMDARs via depolarization. To facilitate clamping, a cesium based internal solution, including QX-314, to block Na^+ currents, and additionally TEA-Cl to block K^+ currents, was used during the mapping experiments to make the cells less leaky. Despite, other sources for signal attenuation might hinder removal of Mg^{2+} block in distal branches.

It is hard to estimate the extent of the unaccounted inputs, since they could stem from numerous reasons listed above, and since it is difficult to design control experiments for each case to quantify their contribution. Nonetheless, assuming their existence, different scenarios might be postulated for their effect on our results. The greatest concern, here, is whether our observation of clusters is merely an artifact of undersampling of the inputs.

One possibility is that L5 excitatory inputs to L5 basal dendrites are truly clustered as we observed. Then, clustering might be achieved either (i) if presynaptic neurons from all locations in L5 homogeneously innervate certain hotspots, or (ii) if subpopulations of L5 selectively innervate different hotspots, or (iii) if individual neurons in L5 make contacts at multiple neighboring synapses simultaneously, and thus the clusters do not even reflect the population circuitry but rather connectivity of a single neuron.

Paired recordings from adjacent L5 neurons in the rat somatosensory cortex and subsequent morphological investigation of the dendritic and axonal arbors

of these pairs revealed synaptic contacts between the two neurons to be distributed over different dendritic branches (Markram et al., 1997). Matsuzaki et al. (2011) stimulated individual L2/3 neurons via two-photon glutamate uncaging and mapped inputs to basal dendrites of L5 neurons via calcium imaging. They did not observe any cluster of neurons making contacts at the same dendritic branch, set aside neurons that made multiple adjacent connections. Therefore, the third mechanism for clustering seems highly unlikely and our observations do reflect the population connectivity.

If these clusters are innervated homogeneously, then this would mean that there could be no bias in the spatial organization of the unaccounted inputs. Depending on the amount, then, these inputs either would present themselves as the gaps in observed clusters, or in larger quantities they would completely disrupt observed clusters and yield a distribution that resembles random dispersion.

A different outcome is expected if the clusters were to be associated to specific subpopulation of neurons. To elaborate, different subpopulation scenarios are to be assumed. The subpopulations might have a spatial organization, that is, they are defined by the proximity of their members to each other and innervate different clusters on the dendrites of the target neurons. This kind of organization might be most susceptible to slicing. The unaccounted inputs then are expected to have an organization on the dendrites, where the loss of input from a subpopulation on the target neurons would remove clusters of detected inputs, resulting in a smaller number of detectable clusters.

The subpopulations might have genetic or epigenetic variability, which might influence the expression level of the transgene under the same promoter, i.e. some subpopulations would express ChR2 in higher quantities relative to other subpopulations, creating a bias for the mappable presynaptic populations. This would as well result in inputs that are missing as clusters from weakly driven presynaptic subpopulations. Similar effects could be expected if different subpopulations have different release probabilities, or make synapses of different strength. If there is no spatial, genetic or synaptic bias to subpopulations, then the outcome of this case is no different than clusters being innervated homogeneously. This holds

true for cases such as unaccounted inputs due to presynaptic cell death during the course of the experiments. Here, we assume there is no bias as any cell is as likely to die as any other cell under the same circumstances.

On the other hand, if there is no clustering in L5 to L5 connectivity, and the contacts are dispersed randomly on dendritic branches, loss of presynaptic partners and subsequently their contacts would manifest the unaccounted inputs at random locations. Mathematically, removal of random samples from a random population will end up with a random subpopulation. Order cannot be attained if all manipulations to a random system are random. No physiologically persuasive explanation comes to mind on how it would be possible to lose contacts in a way that the remaining ones start showing clustering, if there was not clustering to begin with.

To summarize, removal of random inputs from a clustered organization could end up in a distribution that resembles a random distribution, but removal of random inputs from a dispersed organization cannot create clusters. Any scenario that yields clusters with unaccounted inputs should therefore come from a clustered organization. In this respect, it could have been much more difficult to argue for a finding where the inputs were shown to be randomly distributed on branches.

An artifact could arise if the axons of Thy1-ChR2 are photostimulatable. This case is not desired as L5 of other cortical regions and the hippocampus also express ChR2. It was not possible to test axonal stimulation on these preparations, as the axonal and dendritic arbors overlapped and there was not a region where direct dendritic stimulation could have been avoided. However, judging from the inefficiency in somatic excitability, one can assume this case to be unlikely. Additionally, L5 gets it major input from L5 and L2/3 (Binzegger et al., 2004), hence other brain regions are not expected to innervate L5 significantly to produce misleading false-positives.

4.2   Clusters

This study is the first study that attempted to systematically map functional inputs of a presynaptic population to a postsynaptic population with single synapse resolution. It is also the first study to show plausible evidence for the existence of input clusters between populations, namely L5 pre- and postsynaptic populations. We showed a deviation from simulated segments with random input distribution at distances below 10 μm. The clusters we detected with low occurrence likelihood had a mean size of 11.44±3.17 μm and received 6.09±1.00 inputs.

Though not population specific, and not in large quantities, evidence of clustering in the nervous system already exists. One of the first hints of clustering came from synaptic plasticity studies by Harvey and Svoboda (2007), where they showed that the potentiation of a single synapse decreased the threshold of potentiation of its neighbors within an interaction distance of ~10 μm for ~10 min. This suggested a mechanism which could provoke cluster formation, such that synapses in close proximity promoted the potentiation of one another, and if these synapses received input within the time frame of this promoted potentiation, they could strengthen and stabilize together. Any synapse which would not be active within this time frame would eventually be eliminated, yielding a cluster of synapses with similar activity patterns (Winnubst and Lohmann, 2012). Later, the same authors explained this cross-talk with spread of activated Ras (Harvey et al., 2008). Another interesting hint for plasticity related clustering came from Makino and Malinow (2011) where they showed that sensory experience preferentially potentiated nearby synapses.

Two groups described that the synchronized spontaneous activity was clustered. Kleindienst et al. (2011) investigated the spontaneous activity in developing hippocampal networks and found that the synapses of CA3 pyramidal neurons which were coactivated within a window of 100 ms were more likely to be closer to each other than 16 μm. Establishment of the clustering was dependent on spontaneous activity, as they could abolish the cluster formation by blocking activity with TTX or NMDAR antagonist APV. They argued, spontaneous activity could

be able to organize the synapses at a subcellular level during the development. Similarly, Takahashi et al. (2012) showed in older rat hippocampal slice cultures, where they could resolve spontaneous input in individual spines via Ca^{2+} imaging, synapses that were coactived synchronously were within 8 μm to each other. They also looked at mouse L2/3 somatosensory cortex neurons *in vivo* and they found these synapses to be within 6 μm to each other. Both of these studies demonstrated the existence of clusters, however in terms of circuitry, it still needs to be shown where these inputs are specifically coming from.

Lavzin et al. (2012) demonstrated the role of NMDA spikes *in vivo*, in angular tuning of L4 spiny stellate neurons of barrel cortex. They tackled the underlying circuitry by artificially pairing corticocortical and thalamocortical inputs and evoking what they observed physiologically. Although the exact circuitry still remains to be shown, the existence of such regenerative NMDA spiking that require localized coactivation of inputs (Antic et al., 2010), provides a physiological basis for the employment of clusters.

Our method utilizes artificially evoked presynaptic activity to resolve inputs, therefore cannot address the physiological activation pattern of the inputs observed to be clustered. If they coactivate, then these findings can readily be explained in line of the reported findings introduced above. The mean inter-input distance in the detected clusters was 1.87±0.83 μm, well within the interaction distance for neighbor potentiation (Harvey and Svoboda, 2007), and the distances on clustered synchronous activity (Kleindienst et al., 2011; Takahashi et al., 2012).

Relevance of activity clustering to dendritic integration has been demonstrated by Losonczy and Magee (2006), who showed in hippocampal dendrites that inputs in a ∼20 μm segment of the dendrite could trigger supralinear summation if they were activated with 0.1 ms temporal separation. In this case, 5 inputs were sufficient to trigger the nonlinearity. If inputs were activated with a 2 ms temporal separation, though, the integration remained linear. The clusters we detected had a mean size ∼11 μm, and received input from ∼6 inputs. If these inputs have as well a high temporal coincidence, in addition to their spatial proximity, this could mean that they can potentially trigger the nonlinearities observed by Losonczy

and Magee (2006). Even if these inputs are not activated simultaneously enough to evoke nonlinear activity, sufficient temporal coincidence could be utilized to maximize the transmission probability of information, delivered by the clustered inputs of a redundant presynaptic neuronal population.

It should also be noted that there are conflicting findings to coactivation of inputs in clusters. It was shown *in vivo* that the organization of sensory inputs on dendritic branches of mice in somatosensory cortex (Varga et al., 2011), in visual cortex (Jia et al., 2010), and in auditory cortex (Chen et al., 2011) showed a widespread dispersion. It now needs to be demonstrated how clustering at the circuit level could relate to what happens in the sensory space. It could be possible that different traits of sensory inputs are delivered as temporally independent information channels, therefore would not reveal clustered inputs on a circuit level. In this respect, our results still comply with these findings if the inputs in the detected clusters are not coactivated.

4.3 Evaluation of the Method for Mapping and Its Future

The development of a novel method to investigate microcircuitry was an as important part of this study as what was found by applying it. Advantages and its contribution to mapping studies has been repeatedly pointed out throughout this report. However, can it be trusted? And, is it worth the effort to use it?

The method is reliable and gives trustworthy results. We showed the identified inputs had significantly higher signal than the signal in the dendrite. However, at this stage it should be regarded more as a proof of principle, as there is still room for improvement that should potentially increase the performance and the throughput. It is a method that provides a new level of information that was not possible to get previously, but the difficulty of the experiment itself prevents it from being a mapping method for large scale circuit analysis.

One drawback we encountered was the duration of the experiments. Typically, single experiments had an upper time limit of about two hours, limited by how long patched cells could be kept alive. Within this time window, we tried to scan

entire dendritic branches systematically. We could image with tiles of ~20 μm length. With the overlaps between the tiles, having to image multiple z-planes to capture every single spine, and repeating the measurements for at least three times at each location limited the extent of branches we could map. Our longest maps, summing subbranch lengths together, were around 300 μm. Some advancements could be utilized to extend the experiment time, and simultaneously make it more efficient to acquire the maps.

ChR2 Improvements

The primary reason why the cells needed to be patched was to depolarize them and to facilitate NMDAR currents for detection, where AMPARs were blocked to prevent polysynaptic transmission. We initially tried to obtain presynaptic specificity by performing experiments in the presence of tetrodotoxin (TTX)[1] and 4-aminopyridine (4-AP)[2]. In this setting, AP propagation was blocked by TTX, and synaptic transmission depended on local presynaptic bouton depolarization, enhanced by 4-AP (as done by Zhang and Oertner, 2007). Since polysynaptic input in this setting was not a possibility, it was not necessary to block AMPARs. However, when compared to our current settings, experiments with TTX and 4-AP yielded less detected inputs (data not shown), most likely due to use of wtChR2.

Over the last years many new variants of ChR2 were engineered with superior conductance in comparison to those we used (Berndt et al., 2011; Kleinlogel et al., 2011; Lin et al., 2013). It could be possible to use one of these new variants and to do the experiments by blocking APs. In this case, one could only patch the cell to fill it with a Ca^{2+} indicator, and afterwards retract the pipette to eliminate the loss of cells due to patching. Improving further, it could also be possible to use genetically encoded Ca^{2+} indicators and make the whole mapping process completely noninvasive. Use of a higher conducting ChR2 is also expected to increase the reliability of the evoked presynaptic activity, hence of the experiments overall.

---

[1]voltage-gated Na^+ channel blocker
[2]voltage gated K^+ channel blocker

Hardware Improvements

Hardware improvements can be implemented to make the acquisitions faster. Our system uses galvanometric scanners which have limited scan speeds when compared to some alternatives, such as resonant mirror scanners. Increasing the scan speed will enable to acquire bigger tiles and to proceed faster on the dendrite. It should be also possible to use acousto-optic modulators to perform random access scans (Lv et al., 2006; Otsu et al., 2008), deflecting the beam rapidly on the spine heads and the dendritic regions, and simultaneously imaging from a large area by only acquiring the information that is relevant. Faster acquisitions also mean that more time points can be gathered, which would subdue the effect of noise in the response detection.

It was necessary to protect the PMTs with a shutter during the delivery of the photostimulus. This resulted in missing approximately the first 50 ms of the Ca^{2+} signals while waiting for the shutter opening. Faster shutters, or use of PMTs that can be gated electronically should overcome this limitation. Another possibility is to use 'red' calcium indicators, since then the stray light of the photostimulation can be filtered out much more efficiently, releasing the requirement of a PMT protection.

Dendritic segments which were not parallel to the imaging plane also slowed down the experiment, since those locations needed higher number of z-planes for scanning all spines. A workaround to this problem could be achieved by controlling the focal plane of the objective lens rapidly via piezo controllers. Then on such branches, oblique scans can be made, making the acquisitions much more efficient. A microscopy technique that requires scanning is not even a necessity. A technique such as light sheet microscopy, also recently possible with two-photon fluorescence (Truong et al., 2011), will make the mapping process much faster.

Transfection Improvements

Another drawback was transfection. Using IUE, it was not possible to have a dense enough transfection in V1, which prevented us to map L2/3 inputs on L5 neurons. V1 in comparison to e.g. somatosensory cortex, is a region harder to

target with IUE. It could still be possible to conduct the mapping experiments with the electroporated mice if a different region, where it could be possible to have a denser transfection, is targeted.

Also, alternative methods for transfection could be considered to increase efficiency. With clever strategies using Cre lines (Sauer, 1998), it is possible to get dense transfections in specific neuronal populations via complementing virus injections. Additionally, with the increasing number of Cre lines available to researchers, it will be much quicker to create transgenic lines with specific subpopulations targeted.

4.4 Comparison to Current Mapping Methods

Different methods that map connectivity between different neuron populations were introduced previously in Section 1.3. Here, we discuss how our method differs and how it could potentially complement what already exists.

The most extensive connectivity maps can be acquired quickest by analyzing morphological data. The amount of overlapping axonal and dendritic arbors have been previously used to infer relative connectivity weights between different layers of the cortex (Binzegger et al., 2004). In this study, the location of the inputs were not addressed. These locations can be approximated with the assumption that when the dendrite and the axon are within a certain vicinity, they are potentially connected (Stepanyants and Chklovskii, 2005). The validity of this approximation was investigated by Shepherd et al. (2005) and shown to predict where inputs were. However, this method cannot be used to pinpoint the exact locations of synaptic inputs. These approaches are very useful to give an approximate idea to where to look for inputs, therefore could be used together with our method, especially for naive circuits where there might not be previous information where to expect the inputs.

mGRASP is also a method that makes it easy and quick to probe connectivity between neuronal populations at single synapse resolution (Kim et al., 2012). Specific pre- and postpopulations can be targeted genetically to express the two split GFP fragments, respectively, and contact sites can readily be detected. To

be able to probe whether these contacts are really functional synapses, our method can be incorporated, by expressing also ChR2 in the presynaptic population, and imaging the Ca^{2+} signals in the postsynaptic cells. Then, the tentative inputs revealed by mGRASP can rapidly be screened for physiological activity. This cooperation would be a gain for our method as well by eliminating the requirement of systematically scanning dendritic branches, which is time-wise a bottleneck.

Evoking presynaptic activity by photostimulation via ChR2 gives the advantage of population targeting, as it is a genetically encoded channel. This allows to drive larger populations of presynaptic cells simultaneously by wide field photostimulation, or specifically activate the presynaptic cells via axonal stimulation where the postsynaptic cells are imaged. This is an advantage in terms of maximizing activated inputs in the field of view. This is not possible with other photostimulation methods, such as glutamate uncaging, where the uncaging laser needs to be scanned on the presynaptic cell layer (Matsuzaki et al., 2011; Nikolenko et al., 2007). Electrical stimulation of the presynaptic cells has also been used to map inputs to postsynaptic cells, as done by Richardson et al. (2009), however, in this setting it is not possible to target the presynaptic population specifically.

Petreanu et al. (2007; 2009) also used ChR2 and were able to acquire population specificity. Their mapping strategy was to scan the tissue with the photostimulation laser and measure the light evoked postsynaptic electrical currents. Their maps did not resolve individual input sites, but rather gave the distribution of where they were. Petreanu et al. (2007) also demonstrated another particular advantage of ChR2 assisted circuit mapping, which was the ability to map long range connections via stimulating axons locally. This approach also could supply valuable information in directing a method such as ours on where to map, in especially naive circuits, and our method can provide the single synapse resolution.

Highest resolution maps can be acquired by EM based methods by reconstructing individual neurons from the EM images and locating the synapses between these neurons by identifying the postsynaptic density and the presynaptic vesicles. Briggman et al. (2011) and Bock et al. (2011) demonstrated that it is possible to combine EM based circuit analysis with prior *in vivo* neuron charac-

terization. This provided to obtain connectivity maps of neurons whose functions in the network were identified. Micheva and Smith (2007) combined EM with immunohistochemistry and could supply the connectivity maps with the molecular architecture of the network.

One drawback with EM is the requirement of fixed tissue which prevents obtaining the properties of the inputs. Additionally, the difficulty in data analysis hinders high throughput acquisition of maps. Advances in sample handling, such as with SBSEM (Denk and Horstmann, 2004), allowed to conveniently image complete blocks of tissue and obtain local connectivity. However, the volume of the tissue that can be analyzed is still limited, therefore it is currently not possible to map long range connections with EM. We can complement the limitations of EM based circuitry analysis. It is possible to map the inputs and probe their properties with our method. Although not demonstrated in this study, we can also work with neurons whose function in the network, such as orientation or direction selectivity in V1, have been identified with prior *in vivo* experiments. Also, it should be possible to map long range connections, as reported by Petreanu et al. (2007). The information we can supply from an experiment may further be analyzed in higher detail with EM by reconstructing the complete local connectivity of the cell we experimented on. This way both methods could address the gaps in the acquired data of the other and mutually supply the most extensive connectivity information ever to be shown between two neuronal populations.

Chapter 5

Conclusion

This study introduced a new method for cortical circuitry mapping. It was demonstrated that population specific presynaptic stimulation was evoked by using ChR2. Reliable calcium signals were detected upon photostimulation that enabled to pinpoint the input sites of the presynaptic L5 and L2/3 populations on the basal dendritic branches of postsynaptic L5 neurons. These indentified input sites were shown to have higher Ca^{2+} signals than the signals in the dendrite at their bases. The spines with identified L5 input did not exhibit any morphological difference to the spines with no identified input.

The spatial analysis of the L5 inputs revealed clusters according to the comparisons of the experimental data to the Monte-Carlo simulations and according to their likelihood of occurrence based on combinatorics. Although the method had various sources for false-negatives, this fact did not seem to affect the detection of clusters.

Due to the challenges of transfection of L2/3 neurons in V1, sufficient number of inputs were not detected to draw conclusions.

This method has proven to be reliable and can provide information that was not previously possible to get with existing methods. It can complement other methods by pre- and postsynaptic population specificity at single synapse resolution. Although currently it is more a proof of concept, it can be adapted for large scale input mapping with easy to implement advancements.

Eventually, using this method, it shall be possible to map the connectivity between any two populations of neurons in the brain, provided that it will be possible to target any presynaptic population with high ChR2 expression. Using

better performing ChR2 variants and targeting the postsynaptic populations to express genetically encoded Ca^{2+} indicators, it will be possible to conduct noninvasive, long duration, high throughput experiments, where inputs can be mapped on entire cells, not just on short segments. The method, in principle, will be able to map systematically the entire circuit architecture at synaptic resolution, unveiling information that is missing to relate single neuron processes to network computations.

Appendix A

Additional Data

A.1   Order-Based Dendrograms

Order-based dendrograms from all L5 to L5 input mapping experiments are presented in the following pages. By assuming homogeneous density in spine spatial distribution, order-based dendrograms show the spines which receive L5 input (red), where distance between schematized spines are in number of neighbors. Different lengths of spines with identified input show their success rate in three steps: 0-33%, 33-66% and 66-100%. Spines with no identified input are black. Dashed lines indicate the end of mapping for a particular branch. Figure legend is placed only in the first dendrogram.

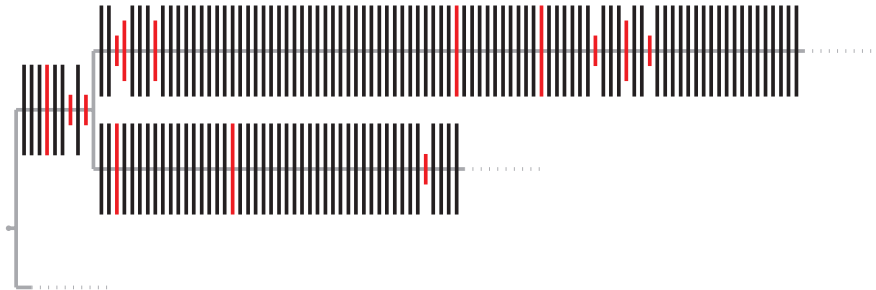Cell ID: 1
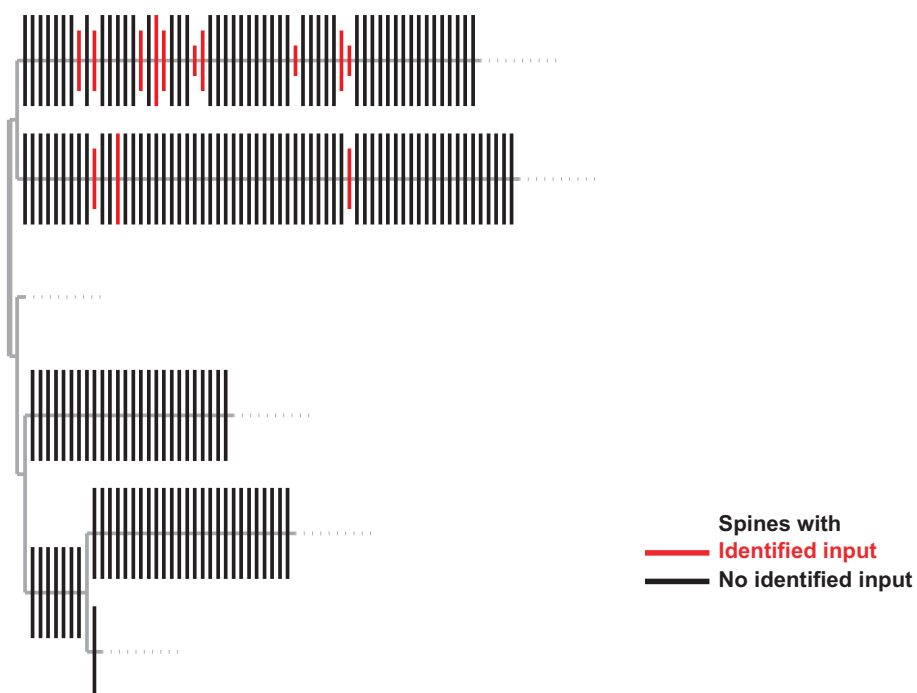
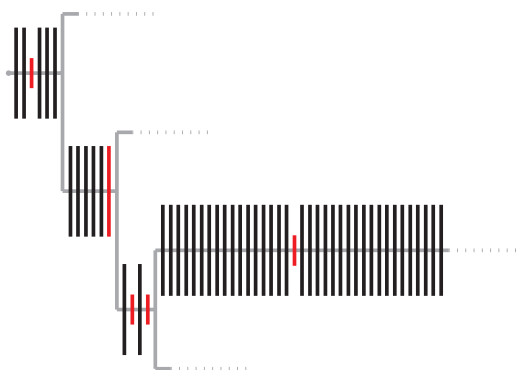Cell ID: 2
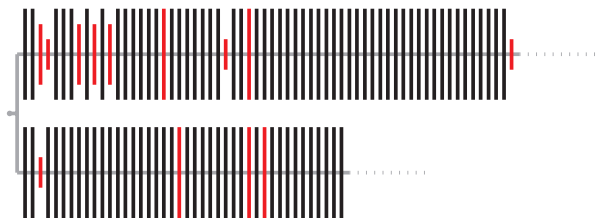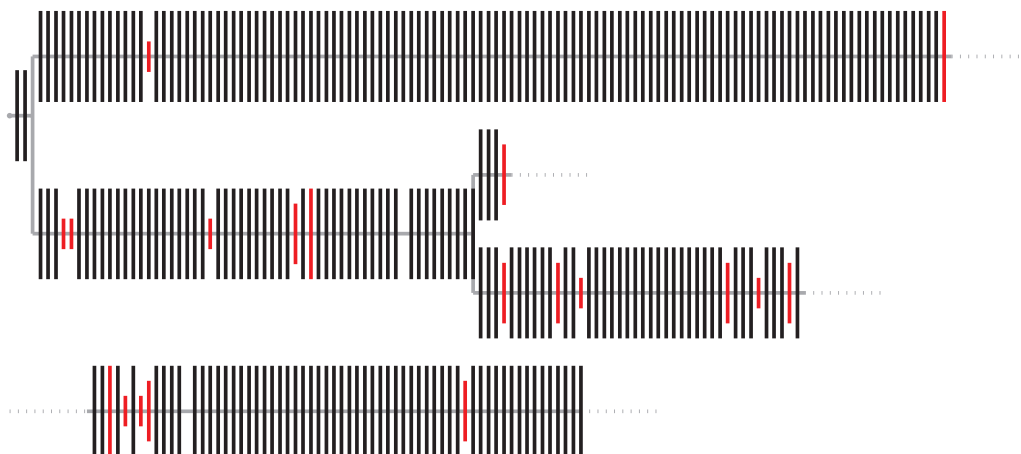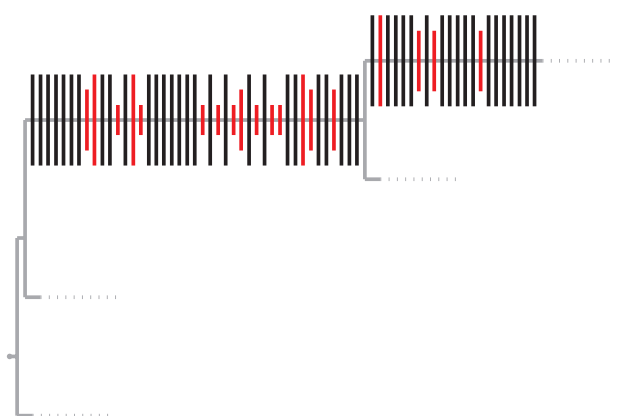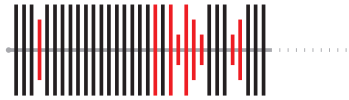
Cell ID: 3

Cell ID: 4
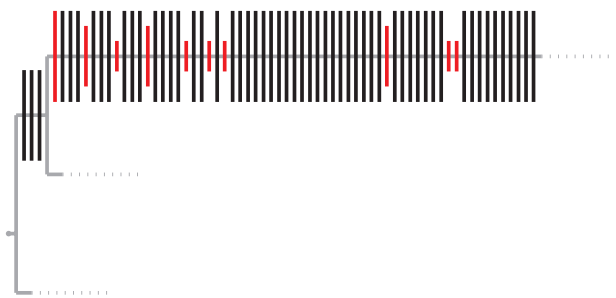
Cell ID: 5
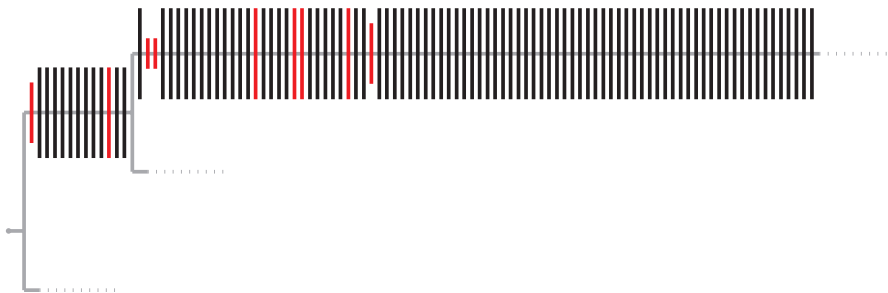
Cell ID: 6
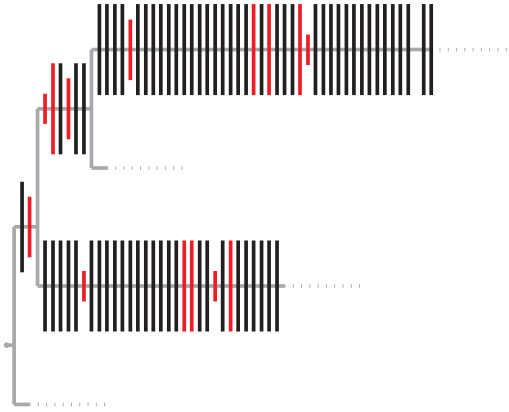
Cell ID: 7
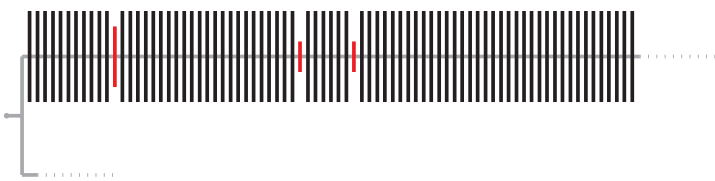
Cell ID: 8

Cell ID: 9

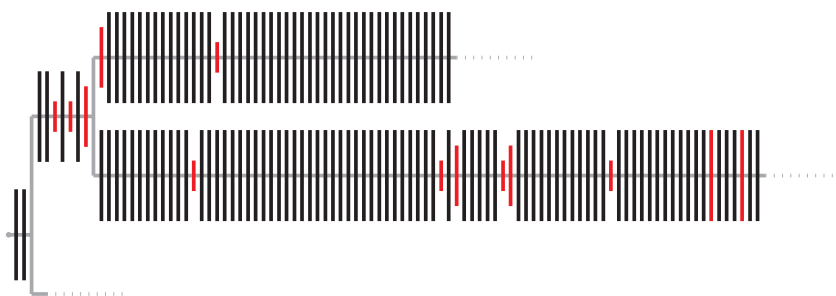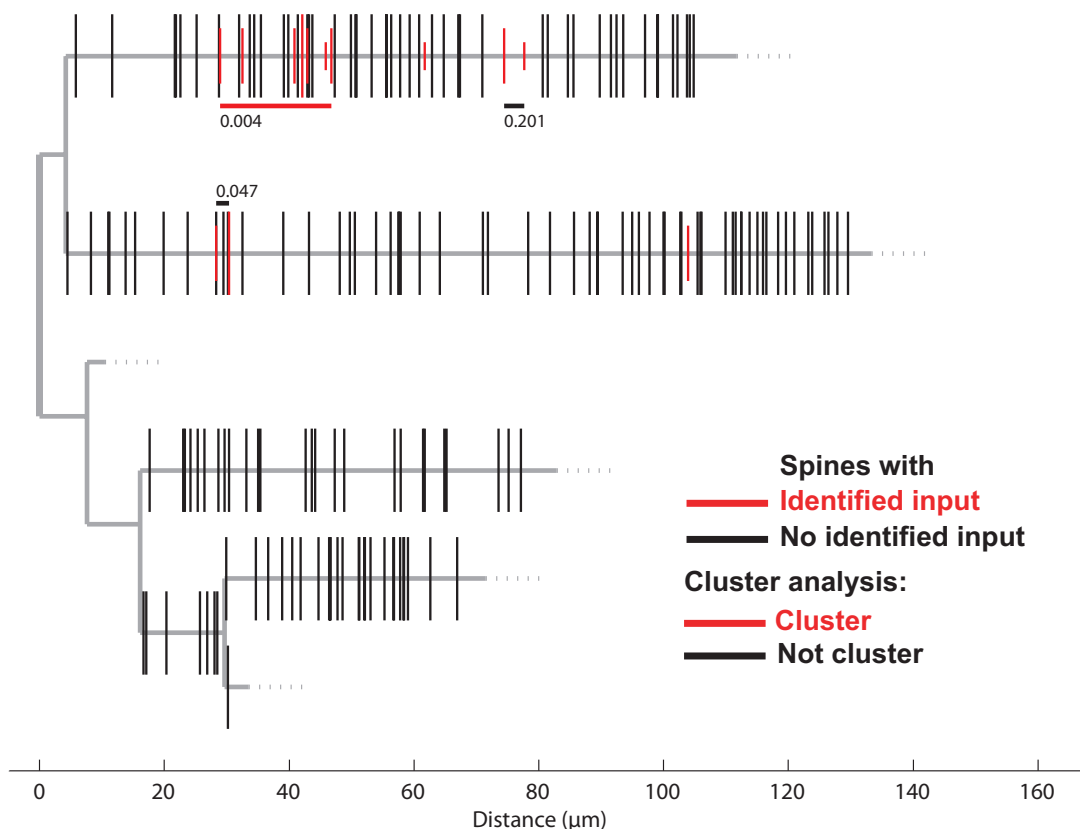Cell ID: 10 (shown previously)
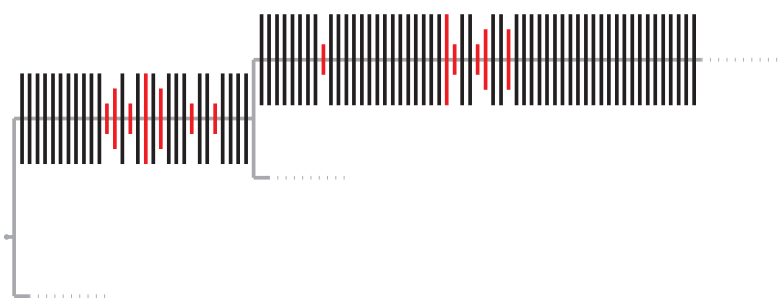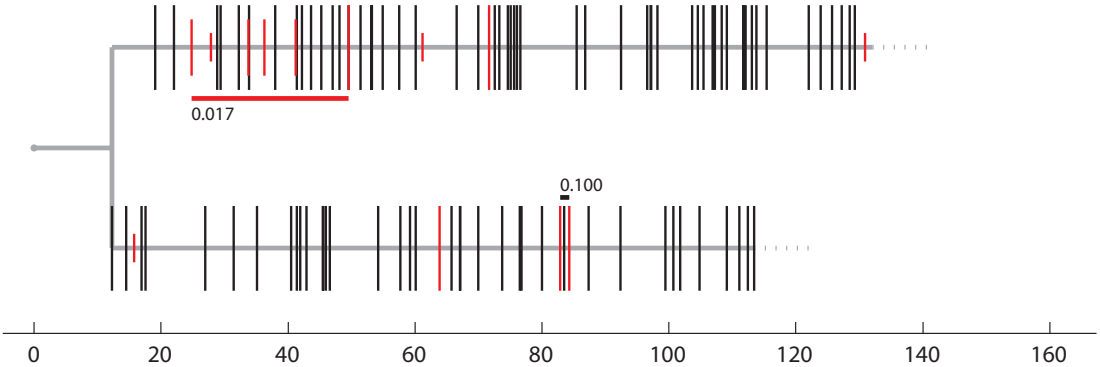
Cell ID: 11

Cell ID: 12

Cell ID: 13

A.2 Distance-Based Dendrograms with Clusters

Results of cluster analysis are shown on distance-based dendrograms from all L5 to L5 input mapping experiments in the following pages. Patterns formed by inputs that are within 10 µm to each other are marked underneath with a red line if they fulfilled the cluster detection criteria (likelihood≤0.02, inputs≥3), hence are clusters, or with a black line if they are not clusters. The likelihood scores are under pattern markings. Spines with identified input are marked with red. Different lengths of these spines show their success rate in three steps: 0-33%, 33-66% and 66-100%. Spines with no identified input are black. Markings that appear thick are multiple spines which are very close to each other, whose markings could not be separated in this scale. Dashed lines indicate the end of mapping for a particular branch. Figure legend is placed only in the first dendrogram. Scale bar is distance in µm.
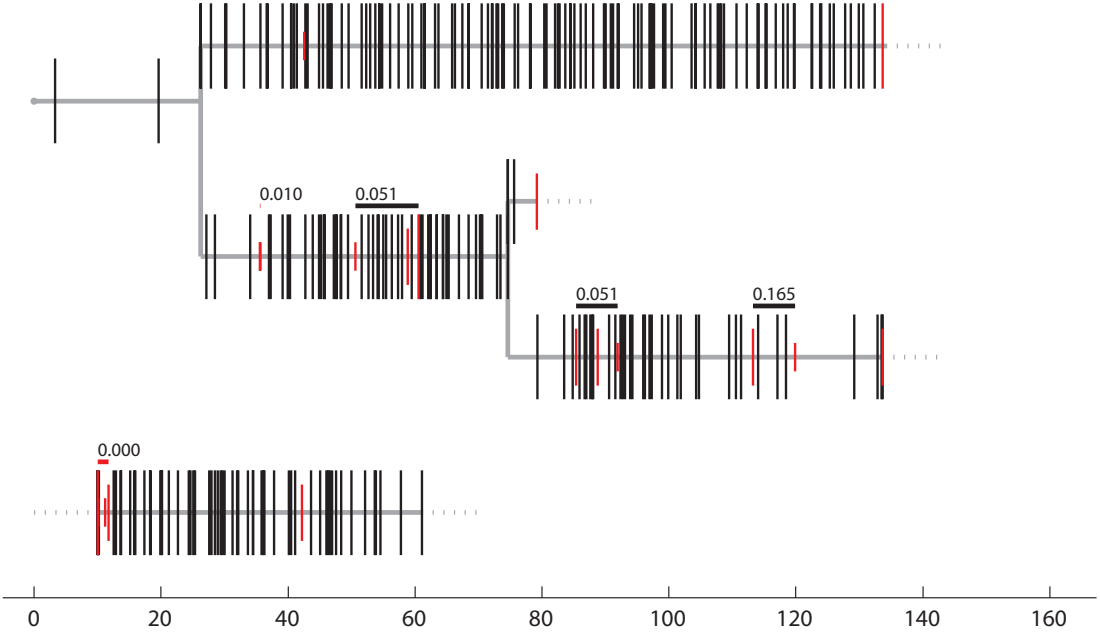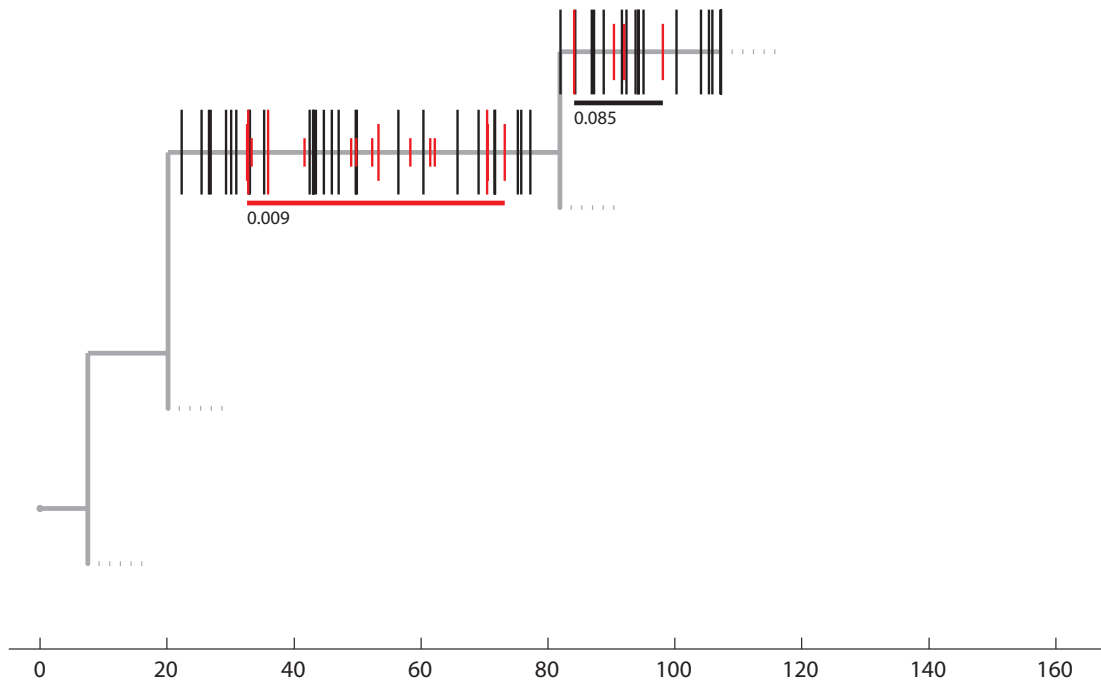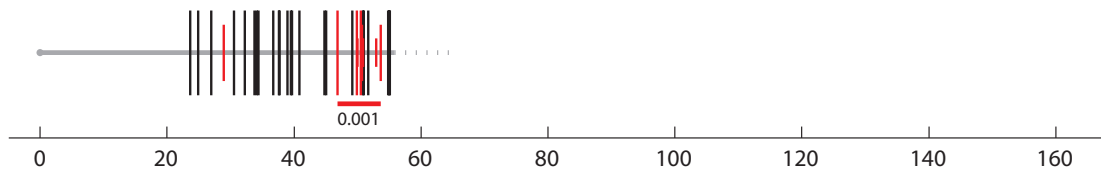
Cell ID: 1

Cell ID: 2

Cell ID: 3

Cell ID: 4

Cell ID: 5

Cell ID: 6

Cell ID: 7

Cell ID: 8

Cell ID: 9

Cell ID: 10 (shown previously)

Cell ID: 11

Cell ID: 12

Cell ID: 13
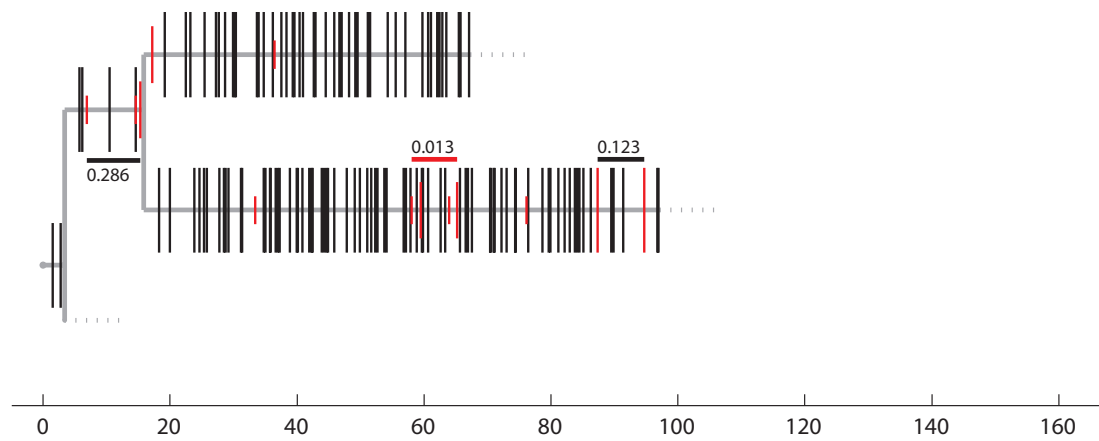
A.3   Spine Cooperativity in Patterns

Alternate visualizations to the patterns formed by inputs that are within 10 μm to each other are presented in the following pages. Here, patterns are shown with activity of their spines over different acquisitions (rows of circles). Red circles are the spines with identified input, with the size of filled circles representing peak ΔG/R amplitude of an input normalized to its mean, and open circles representing failures (no response detected in the acquisition). The fixed size of the open circles represent the mean peak amplitudes. Black dots represent the spines with no identified input. Cluster likelihood scores are shown next to the patterns. Please note that not all of these patterns fulfill the cluster detection criteria. Refer to previous section to see which are detected to be clusters. Figure legend is placed only in the patterns of first cell. Distances between spines are relative distances. Different patterns have different scaling.

Cell ID: 1

Cell ID: 2

Cell ID: 3
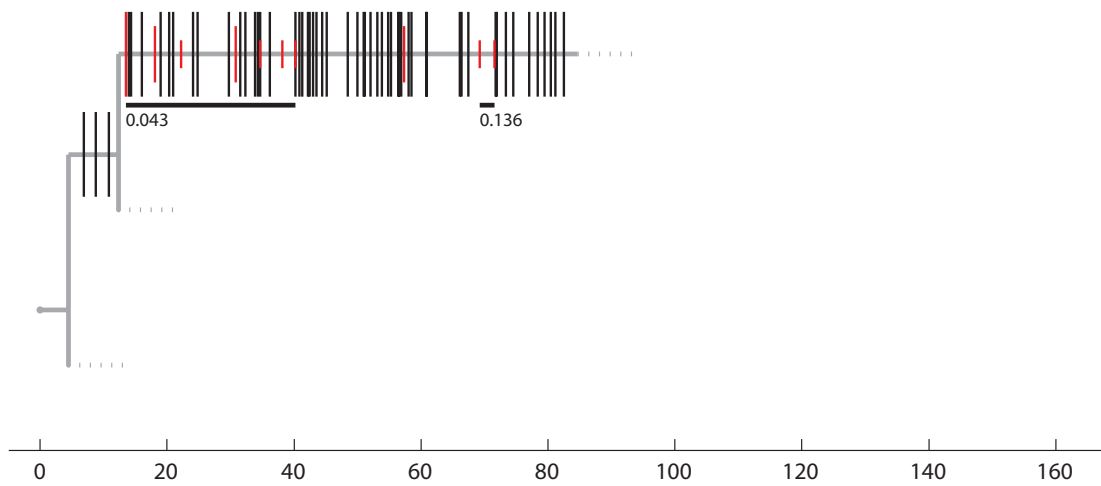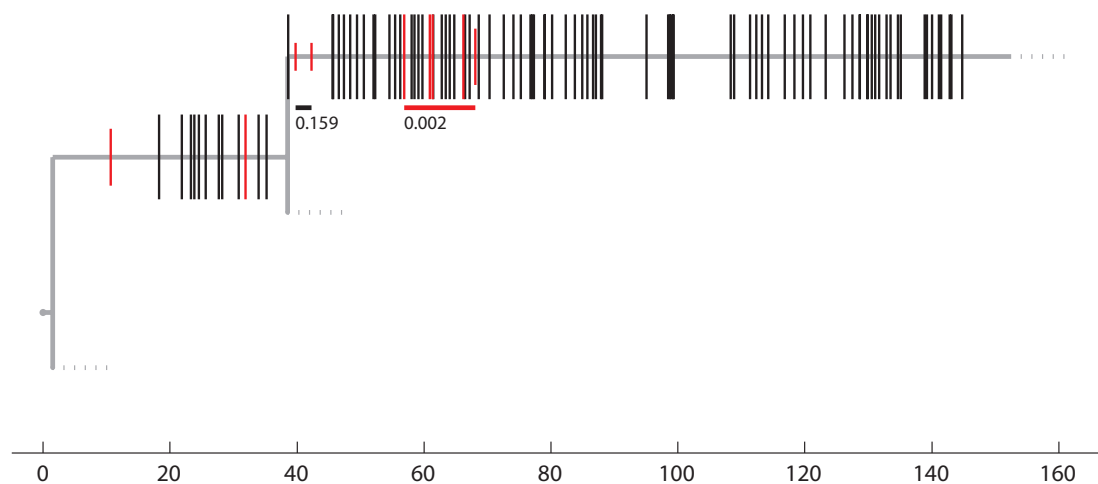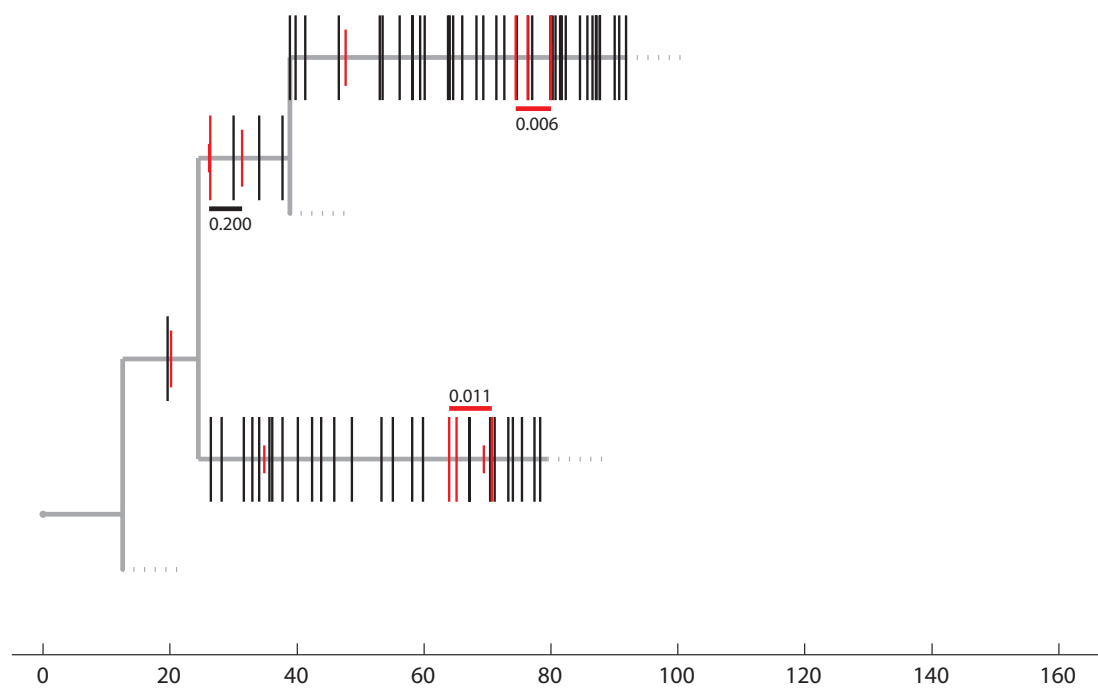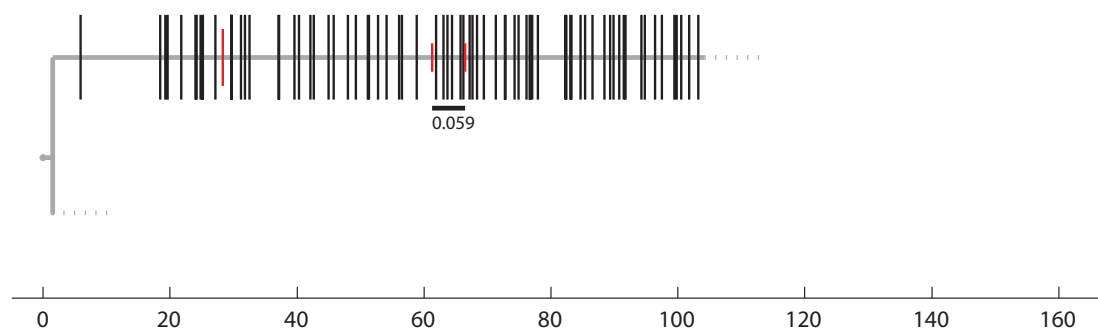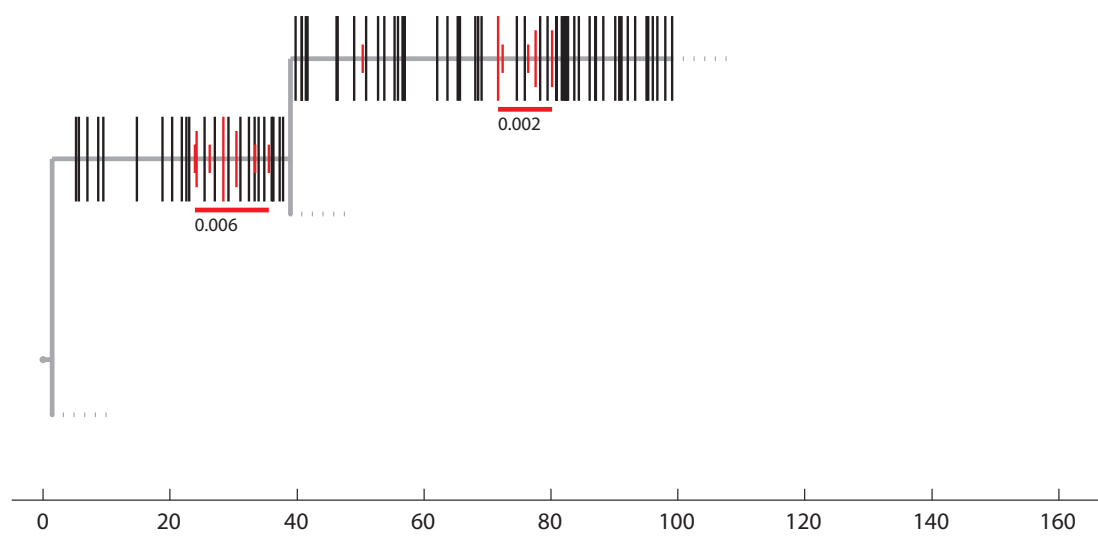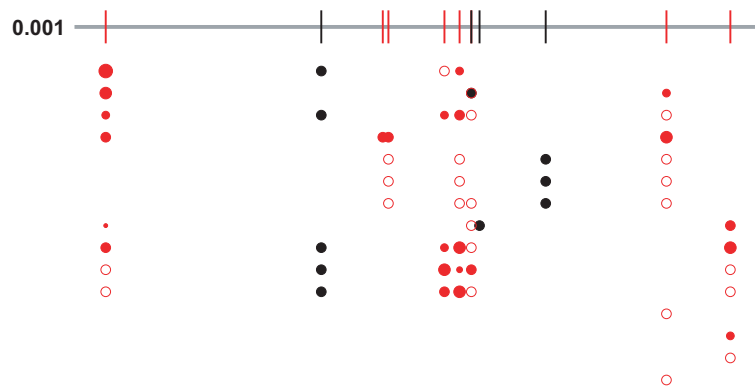

Cell ID: 4
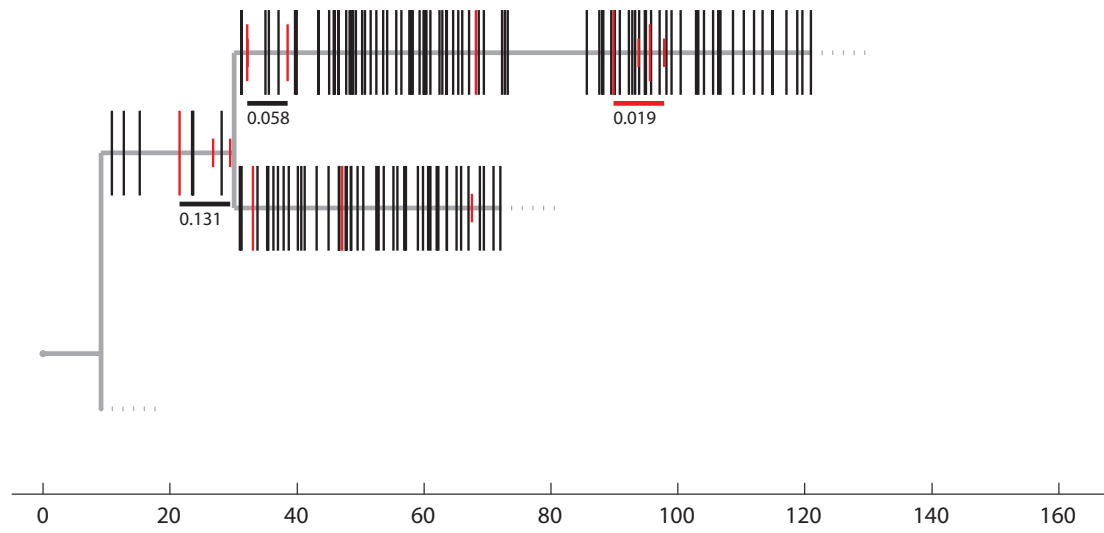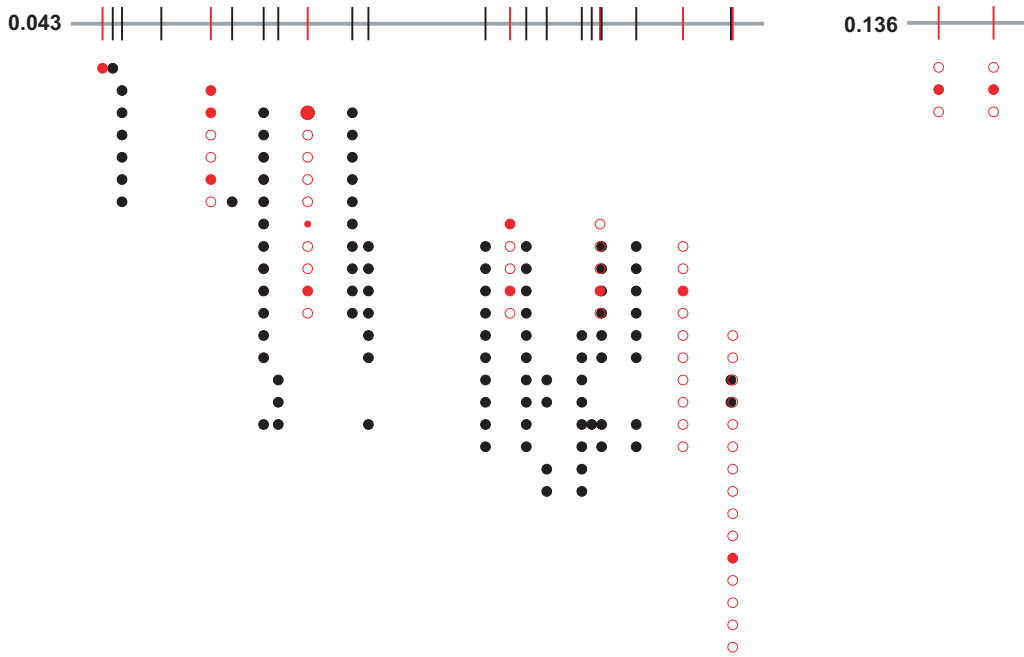

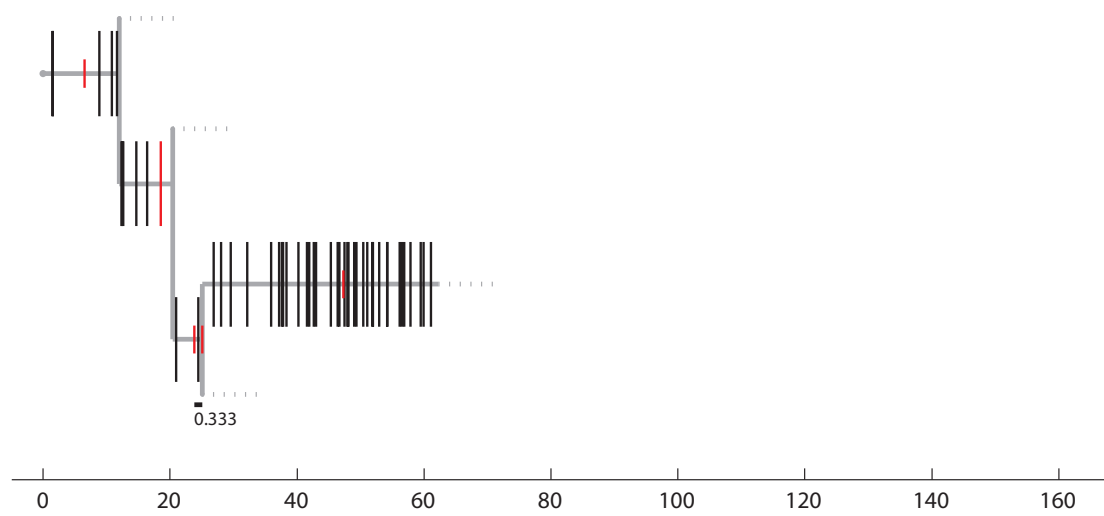Cell ID: 5
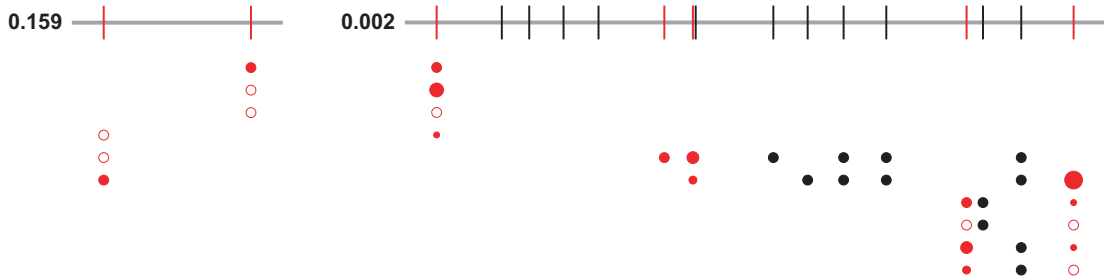
Cell ID: 6
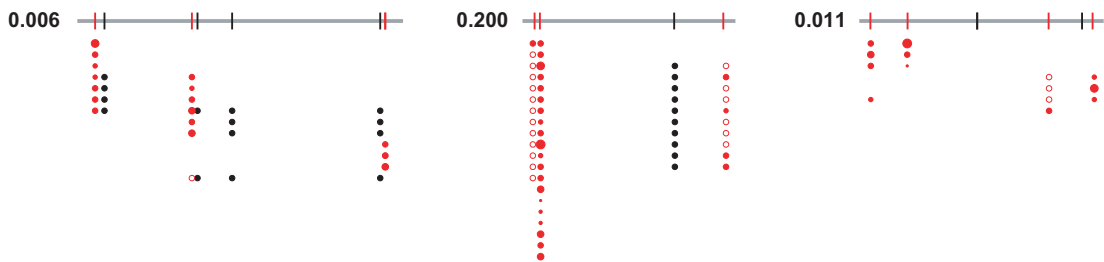
Cell ID: 7
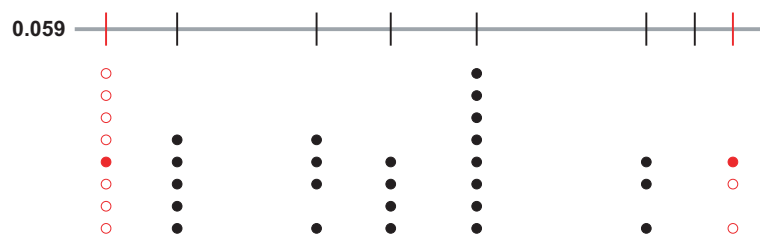
Cell ID: 8

Cell ID: 9

Cell ID: 10 (shown previously)
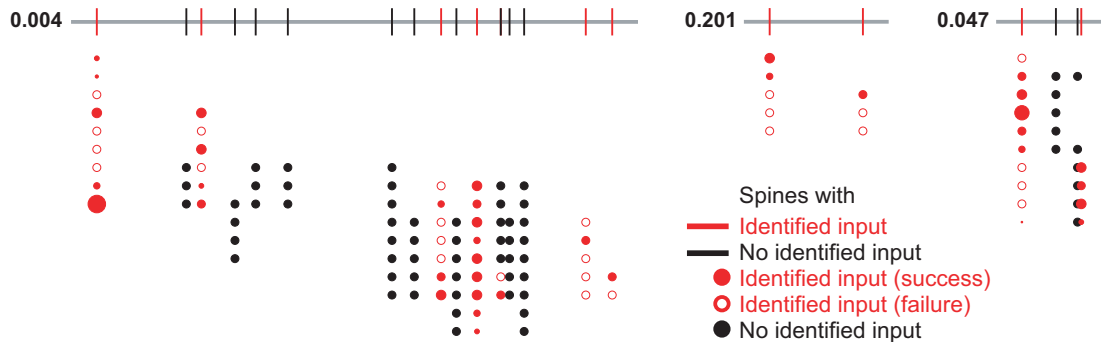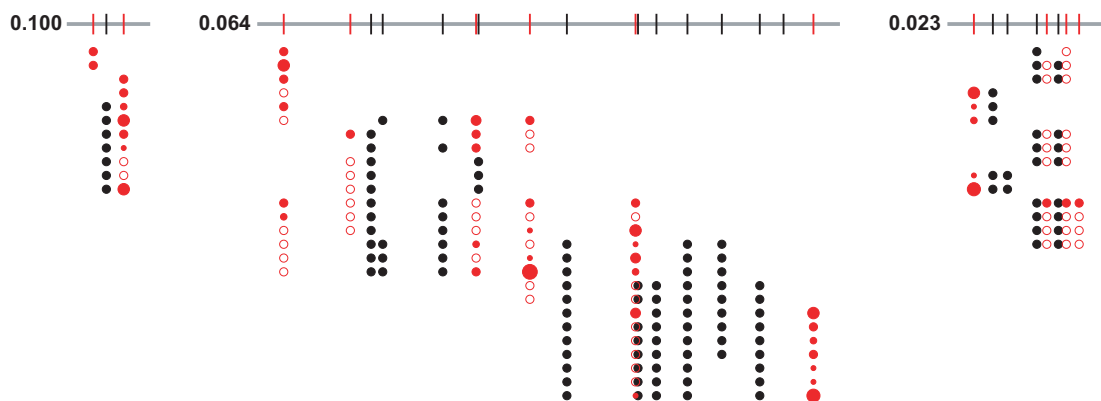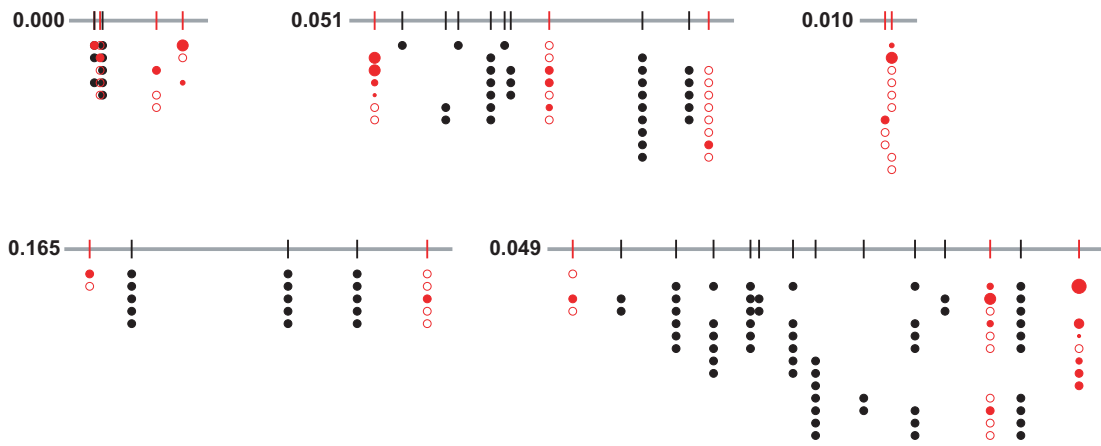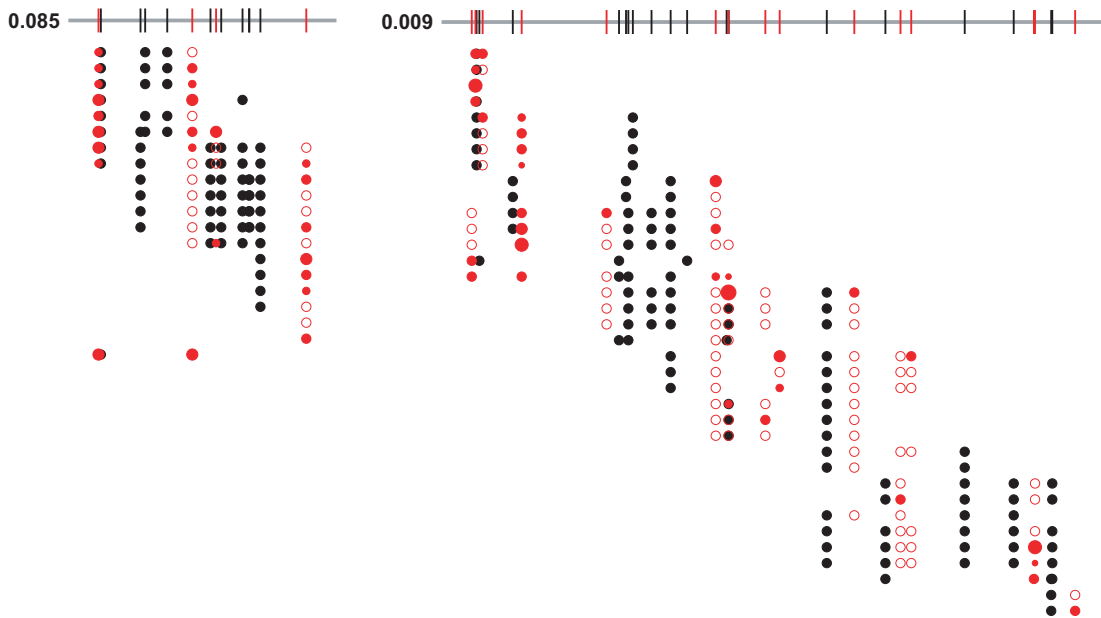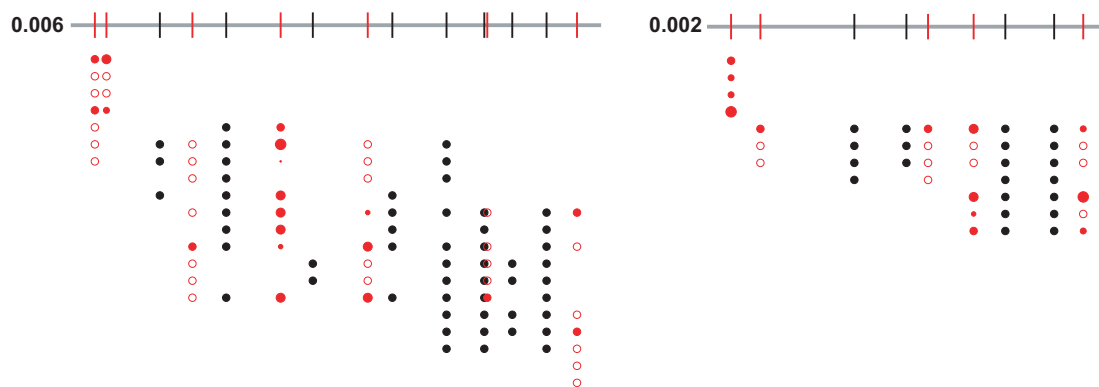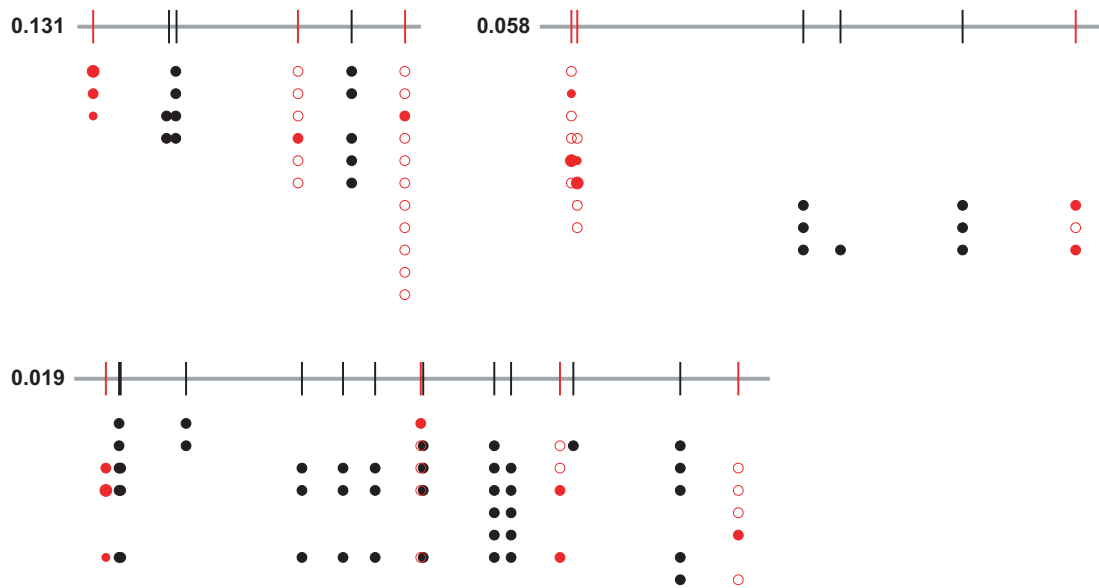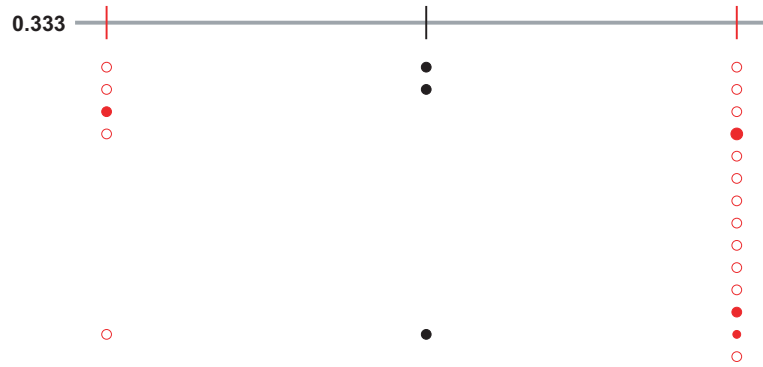

Cell ID: 11

Cell ID: 12

Cell ID: 13
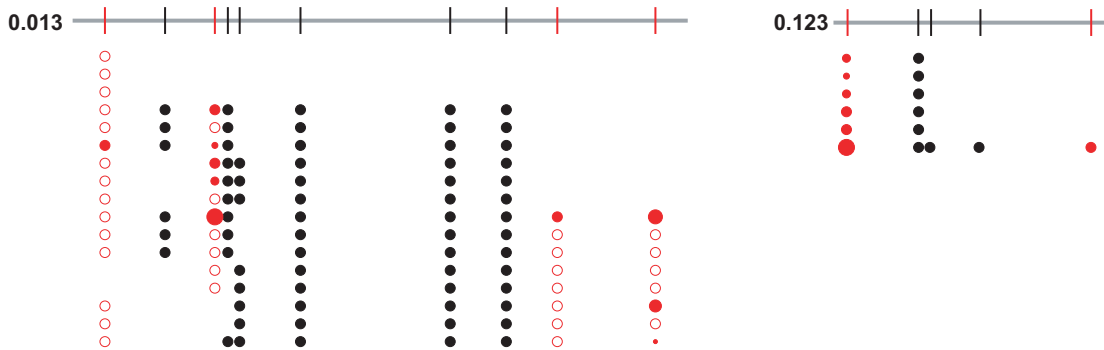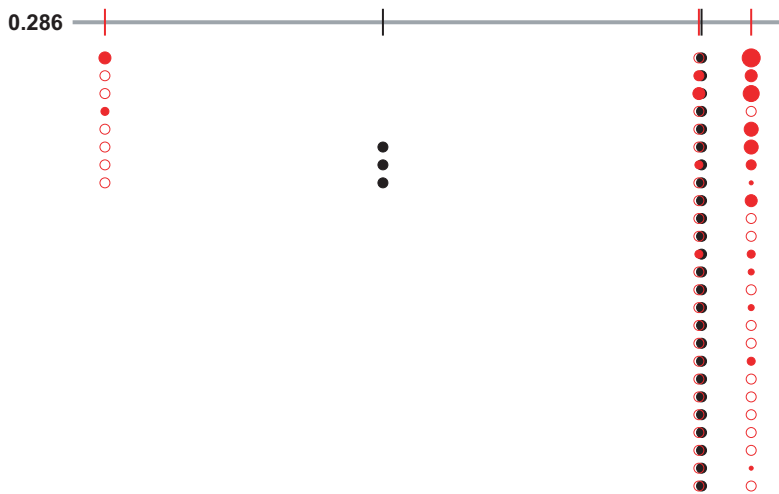
Appendix B

Materials

B.1 Solutions

ACSF Recipes

    choline ACSF in mM (Scheuss et al., 2006): 110 choline chloride, 2.5 KCl, 25 $NaHCO_3$, 1.25 NaH_2PO_4, 0.5 $CaCl_2$, 7 $MgCl_2$, 25 D-glucose, 11.6 Na-L-ascorbate, 3.1 Na-pyruvate.

    experimental ACSF recovery ACSF containing in µM: 10 NBQX, 50 picrotoxin, 10 D-serine.

    recovery ACSF in mM (Scheuss et al., 2006): 127 NaCl, 2.5 KCl, 25 $NaHCO_3$, 1.25 NaH_2PO_4, 2 $CaCl_2$, 1 $MgCl_2$, 25 D-glucose.

Internal Solutions

    "loose-seal" internal solution in mM (Sato et al., 2007): 10 KCl, 140 K-gluconate, 10 HEPES, 2 $MgCl_2$, 2 $CaCl_2$, 0.05 Alexa 594, pH 7.25.

    Cs-based internal solution in mM (Scheuss et al., 2006): 125 Cs-methanesulfonate, 10 HEPES, 10 Na_2phosphocreatine, 4 $MgCl_2$, 4 Na_2-ATP, 0.4 Na-GTP, 3 Na-L-ascorbate, 5 QX-314, 10 TEA-Cl, 1 Fluo-5F, 0.03 Alexa 594, pH 7.3.

    K-based internal solution in mM (Scheuss et al., 2006): 135 K-methylsulfate, 10 HEPES, 10 Na_2phosphocreatine, 4 $MgCl_2$, 4 Na_2-ATP, 0.4 Na-GTP, 3 Na-L-ascorbate, 0.03 Alexa 594, pH 7.3.

PBS in mM: 2.6 KCl, 1.4 KH_2PO_4, 136 NaCl, 8 Na_2HPO_4, pH 7.4.

B.2 Chemicals and Reagents

Cloning: Enzymes and Reagents

    ampicillin Sigma-Aldrich Chemie GmbH, Steinheim, DE, Cat.Nr. A9518-100G.

    iProof HF master mix Bio-Rad Laboratories GmbH, Munich, DE, Cat.Nr. 172-5310.

    LB Broth Difco LB Broth, Becton-Dickinson, Heidelberg, DE, Cat.Nr. 240210.

    NheI-HF New England Biolabs GmbH, Frankfurt am Main, DE, Cat.Nr. R3131S.

    PspXI New England Biolabs GmbH, Frankfurt am Main, DE, Cat.Nr. R0656S.

    T4 DNA ligase New England Biolabs GmbH, Frankfurt am Main, DE, Cat.Nr. M0202S.

    XhoI New England Biolabs GmbH, Frankfurt am Main, DE, Cat.Nr. R0146S.

Cloning: Plasmids

    pCAGGS - ChR2 - Venus Addgene, Cambridge, MA, US, Cat.Nr. 15753.

    pLenti - CaMKIIa - hChR2(H134R) - mCherry - WPRE Addgene, Cambridge, MA, US, Cat.Nr. 20943.

    pLenti - Synapsin - hChR2(H134R) - EYFP - WPRE Addgene, Cambridge, MA, US, Cat.Nr. 20945.

Cloning: Primers (Metabion GmbH, Martinsried, DE)

    PrimerF-A 5′-AATAAGCTAGCATGGACTATGGCGGCGCTTTG-3′.
    PrimerF-B 5′-TATTAGCTAGCATGGTGAGCAAGGGCGAGGAGGATAAC-3′.
    PrimerR 5′-TTATTGCTCGAGTTTACTTGTACAGCTCGTCCATGC-3′.
    PrimerSeq-A 5′-GTTCGGCTTCTGGCGTGT-3′.
    PrimerSeq-B 5′-GTTCACCTTGATGCCGTTCT-3′.
    PrimerSeq-C 5′-TTGCGGATATCTCCGTGAAT-3′.
    PrimerSeq-D 5′-GTCCTGTGGCAAGGTAGAGC-3′.
    PrimerSeq-E 5′-CACATGAAGCAGCACGACTT-3′.
    PrimerSeq-F 5′-TCCTGATCCACGAGCACATA-3′.
    PrimerSeq-G 5′-GCTCTACCTTGCCACAGGAC-3′.
    PrimerSeq-H 5′-ATCTGGCGGAGCCGAAAT-3′.
    PrimerSeq-I 5′-CCGACTACTTGAAGCTGTCCTT-3′.
    PrimerSeq-J 5′-CATGGTCTTCTTCTGCATTACG-3′.
    PrimerSeq-K 5′-TGGAGAGAAAGGCAAAGTGG-3′.

Experiments

    Alexa 594 Molecular Probes, Life Techonologies, Darmstadt, DE, Cat.Nr. A10438.
    CaCl$_2$ Sigma-Aldrich Chemie GmbH, Steinheim, DE, Cat.Nr. 21115-250ML.
    carbogen 95% O_2, 5% CO_2, Westfalen AG, Mnster, DE, Cat.Nr. Secudur C5 095.
    chloral hydrate Sigma-Aldrich Chemie GmbH, Steinheim, DE, Cat.Nr. C-8383-250G.
    choline chloride Sigma-Aldrich Chemie GmbH, Steinheim, DE, Cat.Nr. C1879-500G.
    (R)-CPP Tocris, Bristol, UK, Cat.Nr. 0247.
    Cs-methanesulfonate Sigma-Aldrich Chemie GmbH, Steinheim, DE, Cat.Nr. C-1426-25G.
    D-glucose Carl Roth GmbH, Karlsruhe, DE, Cat.Nr. 6887.1.
    D-serine Tocris, Bristol, UK, Cat.Nr. 0226.
    diethyl ether Sigma-Aldrich Chemie GmbH, Steinheim, DE, Cat.Nr. 32203-1L.
    Fluo-5F Molecular Probes, Life Technologies, Darmstadt, DE, Cat.Nr. F14221.
    HEPES Biomol GmbH, Hamburg, DE, Cat.Nr. 05288.100.
    K-gluconate Sigma-Aldrich Chemie GmbH, Steinheim, DE, Cat.Nr. G4500-100G.
    K-methylsulfate Pfaltz Bauer Inc., Waterbury, CT, US, Cat.Nr. M26480.
    KCl Fluka, Sigma-Aldrich Chemie GmbH, Steinheim, DE, Cat.Nr. 60135-250ML.
    KH$_2$PO$_4$ Merck KGaA, Darmstadt, DE, Cat.Nr. 1.04873.1000.
    MgCl$_2$ Fluka, Sigma-Aldrich Chemie GmbH, Steinheim, DE, Cat.Nr. 63069-100ML.
    Na$_2$-ATP Sigma-Aldrich Chemie GmbH, Steinheim, DE, Cat.Nr. A2383-1G.
    Na$_2$HPO$_4$ Merck KGaA, Darmstadt, DE, Cat.Nr. 1.06586.0500.
    Na$_2$phosphocreatine Sigma-Aldrich Chemie GmbH, Steinheim, DE, Cat.Nr. P7936-1G.
    Na-GTP Sigma-Aldrich Chemie GmbH, Steinheim, DE, Cat.Nr. G8877-1G.
    Na-L-ascorbate Sigma-Aldrich Chemie GmbH, Steinheim, DE, Cat.Nr. A7631-100G.
    Na-pyruvate Sigma-Aldrich Chemie GmbH, Steinheim, DE, Cat.Nr. P2256-25G.
    NaCl VWR International bvba, Leuven, BE, Cat.Nr. 27810.295.
    NaH$_2$PO$_4$ Merck KGaA, Darmstadt, DE, Cat.Nr. 1.06346.0500.
    NaHCO$_3$ Merck KGaA, Darmstadt, DE, Cat.Nr. 1.06329.1000.
    NBQX Tocris, Bristol, UK, Cat.Nr. 1044.
    picrotoxin Tocris, Bristol, UK, Cat.Nr. 1128.
    QX-314 Alomone Labs, Jerusalem, IL, Cat.Nr. Q-150.
    TEA-Cl Sigma-Aldrich Chemie GmbH, Steinheim, DE, Cat.Nr. 86614-25G.

Histology

    Anti-GFP Fitzgerald, Acton, MA, US, Cat.Nr. 20R-GR011.
    Anti-Rabbit Alexa Fluor 488 conjugated. Life Technologies, Darmstadt, DE, Cat.Nr. A11034.
    heparin Sigma-Aldrich Chemie GmbH, Steinheim, DE, Cat.Nr. H4784-250MG.
    lidocaine Research Biochemicals International, Natick, US, Cat.Nr. L102.
    NeuroTrace Red fluorescent Nissl Stain. Molecular Probes, Life Technologies, Darmstadt, DE, Cat.Nr. N-21482.

normal goat serum Sigma-Aldrich Chemie GmbH, Steinheim, DE, Cat.Nr. G6767.
paraformaldehyde Science Services, Munich, DE, Cat.Nr. 15714.
sucrose Merck KGaA, Darmstadt, DE, Cat.Nr. 1.07651.1000.
Triton X-100 Fluka, Sigma-Aldrich Chemie GmbH, Steinheim, DE, Cat.Nr. 93420.

In Utero **Electroporation**
Fast Green Sigma-Aldrich Chemie GmbH, Steinheim, DE, Cat.Nr. F7252-5G.
iodine tincture Braun AG, Melsungen, DE, Cat.Nr. 3864235.
isoflurane Baxter Deutschland GmbH, Unterschleißheim, DE, Cat.Nr. HDG9623.
Isopto-Max eye ointment Alcon Pharma GmbH, Freiburg, DE, Cat.Nr. 2DBA1.
metamizole Novalgin Tropfen, Sanofi-Aventis GmbH, Frankfurt Am Main, DE, Cat.Nr. 72121.
O$_2$ Westfalen AG, Mnster, DE, Cat.Nr. Secudur O.
saline Braun AG, Melsungen, DE, Cat.Nr. 12063451.
tattoo ink Ketchum Manufacturing Inc., Ottawa, CA, Cat.Nr. KI-1471-039.
Tris-HCl Carl Roth GmbH, Karlsruhe, DE, Cat.Nr. 9090.3.
Xylonest 2% with adrenalin (1:200000), Astra Zeneca GmbH, Wedel, DE, Cat.Nr. NE2808A4.

B.3   Equipment and Consumables

Acute Brain Slices
10 ml syringe Braun AG, Melsungen, DE, Cat.Nr. 4606108V.
23 gauge needle Neolus, Terumo Europe N.V., Leuven, BE, Cat.Nr. 74200-14.
27 gauge needle Neolus, Terumo Europe N.V., Leuven, BE, Cat.Nr. NN-2719R.
cutting blade Fine Science Tools GmbH, Heidelberg, DE, Cat.Nr. 10050-00.
glue Pattex, Henkel, Düsseldorf, DE.
sliding microtome Mikrom HM 400, Thermo Fisher Scientific Inc., Waltham, MA, US.
surgical blade Bruno Bayha GmbH, Tuttlingen, DE, Cat.Nr. 24.
vibratome VT1200S, Leica Biosystems GmbH, Nussloch, DE.

Experiments and Analysis
acquisition board BNC-2090A, National Instruments Germany GmbH, Munich, DE.
electro-optic modulator pockels cells: 350-80, controller: 302 RM, Conoptics, Danbury, CT, US.
galvanometric scanner Yanus iMic 2030 Scan Head, Till Photonics GmbH, Gräfelfing, DE.
headstage Axon Instruments CV-7B, Molecular Devices GmbH, Biberach an der Riss, DE.
Labview 8.6 National Instruments Germany GmbH, Munich, DE.
LED KSL 70, 470 nm, Rapp Optoelectronic, Wedel, DE.
Mai Tai Newport Spectra-Physics GmbH, Darmstadt, DE.
Matlab 2011a Mathworks, Ismaning, DE.
micromanipulator controller: Luigs-Neumann SM 5-9, actuators: Luigs-Neumann Junior, Ratingen, DE.
Millenia-Tsunami Newport Spectra-Physics GmbH, Darmstadt, DE.
MultiClamp 700B amplifier Axon Instruments, Molecular Devices GmbH, Biberach an der Riss, DE.
objective lens LUMPlanFI/IR 60×/0.90 W, Olympus Deutschland GmbH, Hamburg, DE.
oscilloscope TDS2014B, Tektronix UK Ltd., Berkshire, UK.
peristaltic pump Minipuls 3, Gilson, Middleton, WI, US.
PMT tubes: E850-22, Hamamatsu Photonics Deutschland GmbH, Herrsching am Ammersee, DE, power source: PS310, Stanford Research Systems, Sunnyvale, CA, US.
preamplifier DHPCA-100, Femto Messtechnik GmbH, Berlin, DE.

shutter Uniblitz VS25S2ZM0R1-21, driver:Uniblitz VCM-D1, Vincent Associates, Rochester, NY, US.

stepping motor Vextra PK244M-01B, Oriental Motor Europa GmbH, Düsseldorf, DE.

thin walled glass capillary World Precision Instruments, Sarasota, FL, US, Cat.Nr. TW150F-3.

vibration isolation table Table: M-ST-UT2 tuned-damped optical table; legs: I-2000. Newport Spectra-Physics GmbH, Darmstadt, DE.

In Utero Electroporation

adson forceps Fine Science Tools GmbH, Heidelberg, DE, Cat.Nr. 11006-12.

analog heatblock VWR International, Darmstadt, DE, Cat.Nr. 460-3249.

electrode BTX Tweezertrode 7mm, Harvard Apparatus, Holliston, MA, US, Cat.Nr. 45-0118.

electrode gel Signa gel, Parker Laboratories Inc., Fairfield, NJ, US, Cat.Nr. 15-60.

electroporator BTX ECM 830, Harvard Apparatus, Holliston, MA, US.

EndoFree Plasmid Mega Kit Qiagen GmbH, Hilden, DE, Cat.Nr. 12381.

gauze pad Gazin 7.5×7.5 mm, Lohmann Raucher GmbH, Neuwied, DE.

glass bead sterilizer Steri 350, Inotech Biosystems International, Dietikon, CH.

heating pad Homeothermic blanket system, Harvard Apparatus, Holliston, MA, US.

iris scissors Fine Science Tools GmbH, Heidelberg, DE, Cat.Nr. 14090-09.

Master-8 pulse stimulator A.M.P.I., Jerusalem, IL.

multipurpose tissue Molinea, Paul Hartmann AG, Molinea, DE, Cat.Nr. 992330/9.

narrow pattern forceps Fine Science Tools GmbH, Heidelberg, DE, Cat.Nr. 11002-12.

picospritzer Toohey Spritzer, Toohey Company, Fairfield, NJ, US.

plastic Pasteur pipette Alpha Laboratories Ltd., Hampshire, UK, Cat.Nr. LW4692.

polyester suture Size: 6-0. Needle: Taper point C-1, 13 mm, 3/8 circle. Ethicon Ethibond Excel, Johnson Johnson Medical GmbH, Norderstedt, DE, Cat.Nr. 6889H.

QIAEX II Gel Extraction Kit Qiagen GmbH, Hilden, DE, Cat.Nr. 20021.

QIAGEN Plasmid Mini Kit Qiagen GmbH, Hilden, DE, Cat.Nr. 12125.

ring forceps Karl Hammacher GmbH, Solingen, DE, Cat.Nr. HSC 703-96 (6 mm), HSC 702-93 (3 mm).

silk suture Size: 6-0. Needle: Taper point BV-1, 9.3 mm, 3/8 circle. Ethicon Perma-Hand Seide, Johnson Johnson Medical GmbH, Norderstedt, DE, Cat.Nr. K802H.

surgical drape Foliodrape, Paul Hartmann AG, Molinea, DE, Cat.Nr. 277507.

surgical microscope Carl Zeiss, West Germany.

thick wall glass capillary Clark, GC150F-10, Warner Instruments, Harvard Apparatus, Holliston, MA, US, Cat.Nr. 30-0057.

trimmer Aeuculap Isis GT420, Braun Vet Care GmbH, Tuttlingen, DE.

Ultrafree-MC centrifugal filter unit Millipore, Merck KGaA, Darmstadt, DE, Cat.Nr. UFC30GVNB.

vaporizer Isoflurane Vapor 2000, Dräger, Lübeck, DE.

vertical puller PC-10, Narishige International Ltd., London, UK.

Bibliography

S. D. Antic, W.-L. Zhou, A. R. Moore, S. M. Short, and K. D. Ikonomu. The decade of the dendritic nmda spike. *J Neurosci Res*, 88(14):2991–3001, Nov 2010. doi: 10.1002/jnr.22444. URL http://www.pubmed.org/20544831.

I. Ballesteros-Yáñez, R. Benavides-Piccione, G. N. Elston, R. Yuste, and J. DeFelipe. Density and morphology of dendritic spines in mouse neocortex. *Neuroscience*, 138(2):403–409, Jan 2006. doi: 10.1016/j.neuroscience. 2005.11.038. URL http://www.pubmed.org/16457955.

P. H. Barry and J. W. Lynch. Liquid junction potentials and small cell effects in patch-clamp analysis. *J Membr Biol*, 121(2):101–117, Apr 1991. URL http://www.pubmed.org/1715403.

A. Berndt, P. Schoenenberger, J. Mattis, K. M. Tye, K. Deisseroth, P. Hegemann, and T. G. Oertner. High-efficiency channelrhodopsins for fast neuronal stimulation at low light levels. *Proc Natl Acad Sci U S A*, 108 (18):7595–7600, May 2011. doi: 10.1073/pnas.1017210108. URL http://www.pubmed.org/21504945.

T. Binzegger, R. J. Douglas, and K. A. C. Martin. A quantitative map of the circuit of cat primary visual cortex. *J Neurosci*, 24(39):8441–8453, Sep 2004. doi: 10.1523/JNEUROSCI.1400-04.2004. URL http://www.pubmed.org/15456817.

M. G. Blanton, J. J. Lo Turco, and A. R. Kriegstein. Whole cell recording from neurons in slices of reptilian and mammalian cerebral cortex. *J Neurosci Methods*, 30(3):203–210, Dec 1989. URL http://www.pubmed.org/2607782.

D. D. Bock, W.-C. A. Lee, A. M. Kerlin, M. L. Andermann, G. Hood, A. W. Wetzel, S. Yurgenson, E. R. Soucy, H. S. Kim, and R. C. Reid. Network anatomy and in vivo physiology of visual cortical neurons. *Nature*, 471 (7337):177–182, Mar 2011. doi: 10.1038/nature09802. URL http://www.pubmed.org/21390124.

T. Bonhoeffer and R. Yuste. Spine motility. phenomenology, mechanisms, and function. *Neuron*, 35(6):1019–1027, Sep 2002. URL http://www.pubmed.org/12354393.

J. G. G. Borst. The low synaptic release probability in vivo. *Trends Neurosci*, 33(6):259–266, Jun 2010. doi: 10.1016/j.tins.2010.03.003. URL http://www.pubmed.org/20371122.

J. G. G. Borst and J. Soria van Hoeve. The calyx of held synapse: from model synapse to auditory relay. *Annu Rev Physiol*, 74:199–224, Jan 2012. doi: 10.1146/annurev-physiol-020911-153236. URL http://www.pubmed.org/22035348.

E. S. Boyden, F. Zhang, E. Bamberg, G. Nagel, and K. Deisseroth. Millisecond-timescale, genetically targeted optical control of neural activity. *Nat Neurosci*, 8(9):1263–1268, Sep 2005. doi: 10.1038/nn1525. URL http://www.pubmed.org/16116447.

T. Branco and M. Häusser. The single dendritic branch as a fundamental functional unit in the nervous system. *Curr Opin Neurobiol*, 20(4):494–502, Aug 2010. doi: 10.1016/j.conb.2010.07.009. URL http://www.pubmed.org/20800473.

T. Branco and M. Häusser. Synaptic integration gradients in single cortical pyramidal cell dendrites. *Neuron*, 69(5):885–892, Mar 2011. doi: 10.1016/j.neuron.2011.02.006. URL http://www.pubmed.org/21382549.

T. Branco, B. A. Clark, and M. Häusser. Dendritic discrimination of temporal input sequences in cortical neurons. *Science*, 329(5999):1671–1675, Sep 2010. doi: 10.1126/science.1191996. URL http://www.pubmed.org/20705816.

K. L. Briggman, M. Helmstaedter, and W. Denk. Wiring specificity in the direction-selectivity circuit of the retina. *Nature*, 471(7337):183–188, Mar 2011. doi: 10.1038/nature09818. URL http://www.pubmed.org/21390125.

S. P. Brown and S. Hestrin. Intracortical circuits of pyramidal neurons reflect their long-range axonal targets. *Nature*, 457(7233):1133–1136, Feb 2009. doi: 10.1038/nature07658. URL http://www.pubmed.org/19151698.

D. P. Buxhoeveden and M. F. Casanova. The minicolumn hypothesis in neuroscience. *Brain*, 125(Pt 5):935–951, May 2002. URL http://www.pubmed.org/11960884.

Z. F. H. Cao, D. Burdakov, and Z. Sarnyai. Optogenetics: potentials for addiction research. *Addict Biol*, 16(4): 519–531, Oct 2011. doi: 10.1111/j.1369-1600.2011.00386.x. URL http://www.pubmed.org/21929708.

X. Chen, U. Leischner, N. L. Rochefort, I. Nelken, and A. Konnerth. Functional mapping of single spines in cortical neurons in vivo. *Nature*, 475(7357):501–505, Jul 2011. doi: 10.1038/nature10193. URL http://www.pubmed.org/21706031.

J. D. Clements and J. M. Bekkers. Detection of spontaneous synaptic events with an optimally scaled template. *Biophys J*, 73(1):220–229, Jul 1997. doi: 10.1016/S0006-3495(97)78062-7. URL http://www.pubmed.org/9199786.

J. DeFelipe. From the connectome to the synaptome: an epic love story. *Science*, 330(6008):1198–1201, Nov 2010. doi: 10.1126/science.1193378. URL http://www.pubmed.org/21109663.

J. DeFelipe, L. Alonso-Nanclares, and J. I. Arellano. Microstructure of the neocortex: comparative aspects. *J Neurocytol*, 31(3-5):299–316, Jan 2002. URL http://www.pubmed.org/12815249.

W. Denk and H. Horstmann. Serial block-face scanning electron microscopy to reconstruct three-dimensional tissue nanostructure. *PLoS Biol*, 2(11):e329, Nov 2004. doi: 10.1371/journal.pbio.0020329. URL http://www.pubmed.org/15514700.

W. Denk and K. Svoboda. Photon upmanship: why multiphoton imaging is more than a gimmick. *Neuron*, 18 (3):351–357, Mar 1997. URL http://www.pubmed.org/9115730.

W. Denk, J. H. Strickler, and W. W. Webb. Two-photon laser scanning fluorescence microscopy. *Science*, 248 (4951):73–76, Apr 1990. URL http://www.pubmed.org/2321027.

W. Denk, M. Sugimori, and R. Llinás. Two types of calcium response limited to single spines in cerebellar purkinje cells. *Proc Natl Acad Sci U S A*, 92(18):8279–8282, Aug 1995. URL http://www.pubmed.org/7667282.

W. Denk, R. Yuste, K. Svoboda, and D. W. Tank. Imaging calcium dynamics in dendritic spines. *Curr Opin Neurobiol*, 6(3):372–378, Jun 1996. URL http://www.pubmed.org/8794079.

H. U. Dodt and W. Zieglgänsberger. Infrared videomicroscopy: a new look at neuronal structure and function. *Trends Neurosci*, 17(11):453–458, Nov 1994. URL http://www.pubmed.org/7531885.

R. J. Douglas and K. A. C. Martin. Mapping the matrix: the ways of neocortex. *Neuron*, 56(2):226–238, Oct 2007a. doi: 10.1016/j.neuron.2007.10.017. URL http://www.pubmed.org/17964242.

R. J. Douglas and K. A. C. Martin. Recurrent neuronal circuits in the neocortex. *Curr Biol*, 17(13):R496–R500, Jul 2007b. URL http://www.pubmed.org/17610826.

R. J. Douglas, K. A. C. Martin, and D. Whitteridge. A canonical microcircuit for neocortex. *Neural Computation*, 1(4):480–488, 1989. doi: 10.1162/neco.1989.1.4.480.

F. A. Edwards, A. Konnerth, B. Sakmann, and T. Takahashi. A thin slice preparation for patch clamp recordings from neurones of the mammalian central nervous system. *Pflugers Arch*, 414(5):600–612, Sep 1989. URL http://www.pubmed.org/2780225.

E. H. Feinberg, M. K. Vanhoven, A. Bendesky, G. Wang, R. D. Fetter, K. Shen, and C. I. Bargmann. Gfp reconstitution across synaptic partners (grasp) defines cell contacts and synapses in living nervous systems. *Neuron*, 57(3):353–363, Feb 2008. doi: 10.1016/j.neuron.2007.11.030. URL http://www.pubmed.org/18255029.

M. Ferrante, M. Migliore, and G. A. Ascoli. Functional impact of dendritic branch-point morphology. *J Neurosci*, 33(5):2156–2165, Jan 2013. doi: 10.1523/JNEUROSCI.3495-12.2013. URL http://www.pubmed.org/23365251.

J. C. Fiala, M. Feinberg, V. Popov, and K. M. Harris. Synaptogenesis via dendritic filopodia in developing hippocampal area ca1. *J Neurosci*, 18(21):8900–8911, Nov 1998. URL http://www.pubmed.org/9786995.

K. J. Field, W. J. White, and C. M. Lang. Anaesthetic effects of chloral hydrate, pentobarbitone and urethane in adult male rats. *Lab Anim*, 27(3):258–269, Jul 1993. URL http://www.pubmed.org/8366672.

N. L. Golding, T. J. Mickus, Y. Katz, W. L. Kath, and N. Spruston. Factors mediating powerful voltage attenuation along ca1 pyramidal neuron dendrites. *J Physiol*, 568(Pt 1):69–82, Oct 2005. doi: 10.1113/jphysiol.2005.086793. URL http://www.pubmed.org/16002454.

E. G. Gray. Axo-somatic and axo-dendritic synapses of the cerebral cortex: an electron microscope study. *J Anat*, 93:420–433, Oct 1959a. URL `http://www.pubmed.org/13829103`.

E. G. Gray. Electron microscopy of synaptic contacts on dendrite spines of the cerebral cortex. *Nature*, 183 (4675):1592–1593, Jun 1959b. URL `http://www.pubmed.org/13666826`.

W. N. Grimes, J. Zhang, C. W. Graydon, B. Kachar, and J. S. Diamond. Retinal parallel processors: more than 100 independent microcircuits operate within a single interneuron. *Neuron*, 65(6):873–885, Mar 2010. doi: 10.1016/j.neuron.2010.02.028. URL `http://www.pubmed.org/20346762`.

A. T. Gulledge, B. M. Kampa, and G. J. Stuart. Synaptic integration in dendritic trees. *J Neurobiol*, 64(1): 75–90, Jul 2005. doi: 10.1002/neu.20144. URL `http://www.pubmed.org/15884003`.

O. P. Hamill, A. Marty, E. Neher, B. Sakmann, and F. J. Sigworth. Improved patch-clamp techniques for high-resolution current recording from cells and cell-free membrane patches. *Pflugers Arch*, 391(2):85, Aug 1981. URL `http://www.pubmed.org/6270629`.

X. Han and E. S. Boyden. Multiple-color optical activation, silencing, and desynchronization of neural activity, with single-spike temporal resolution. *PLoS One*, 2(3):e299, Jan 2007. doi: 10.1371/journal.pone.0000299. URL `http://www.pubmed.org/17375185`.

M. T. Harnett, J. K. Makara, N. Spruston, W. L. Kath, and J. C. Magee. Synaptic amplification by dendritic spines enhances input cooperativity. *Nature*, 491(7425):599–602, Nov 2012. doi: 10.1038/nature11554. URL `http://www.pubmed.org/23103868`.

M. T. Harnett, N.-L. Xu, J. C. Magee, and S. R. Williams. Potassium channels control the interaction between active dendritic integration compartments in layer 5 cortical pyramidal neurons. *Neuron*, 79(3):516–529, Aug 2013. doi: 10.1016/j.neuron.2013.06.005. URL `http://www.pubmed.org/23931999`.

K. M. Harris and S. B. Kater. Dendritic spines: cellular specializations imparting both stability and flexibility to synaptic function. *Annu Rev Neurosci*, 17:341–371, Jan 1994. URL `http://www.pubmed.org/8210179`.

K. M. Harris and J. K. Stevens. Study of dendtiric spines by serial electron microscopy and three-dimensional reconstructions. In B. M. Lasek RJ, editor, *Intrinsic Determinants of Neuronal Form and Function*, pages 179–199, New York, 1988. Alan R. Liss, Inc.

A. R. Harvey, E. Ehlert, J. de Wit, E. S. Drummond, M. A. Pollett, M. Ruitenberg, G. W. Plant, J. Verhaagen, and C. N. Levelt. Use of gfp to analyze morphology, connectivity, and function of cells in the central nervous system. *Methods Mol Biol*, 515:63–95, Jan 2009. doi: 10.1007/978-1-59745-559-6_5. URL `http://www.pubmed.org/19378117`.

C. D. Harvey and K. Svoboda. Locally dynamic synaptic learning rules in pyramidal neuron dendrites. *Nature*, 450(7173):1195–1200, Dec 2007. doi: 10.1038/nature06416. URL `http://www.pubmed.org/18097401`.

C. D. Harvey, R. Yasuda, H. Zhong, and K. Svoboda. The spread of ras activity triggered by activation of a single dendritic spine. *Science*, 321(5885):136–140, Jul 2008. doi: 10.1126/science.1159675. URL `http://www.pubmed.org/18556515`.

A. M. Hattox and S. B. Nelson. Layer v neurons in mouse cortex projecting to different targets have distinct physiological properties. *J Neurophysiol*, 98(6):3330–3340, Dec 2007. doi: 10.1152/jn.00397.2007. URL `http://www.pubmed.org/17898147`.

M. Häusser and B. Mel. Dendrites: bug or feature? *Curr Opin Neurobiol*, 13(3):372–383, Jun 2003. doi: 10.1016/S0959-4388(03)00075-8. URL `http://www.pubmed.org/12850223`.

M. Häusser, N. Spruston, and G. J. Stuart. Diversity and dynamics of dendritic signaling. *Science*, 290(5492): 739–744, Oct 2000. URL `http://www.pubmed.org/11052929`.

M. J. Higley and B. L. Sabatini. Calcium signaling in dendritic spines. *Cold Spring Harb Perspect Biol*, 4(4): a005686, Apr 2012. doi: 10.1101/cshperspect.a005686. URL `http://www.pubmed.org/22338091`.

S. B. Hofer, T. D. Mrsic-Flogel, T. Bonhoeffer, and M. Hübener. Experience leaves a lasting structural trace in cortical circuits. *Nature*, 457(7227):313–317, Jan 2009. doi: 10.1038/nature07487. URL `http://www.pubmed.org/19005470`.

Z. J. Huang, A. Kirkwood, T. Pizzorusso, V. Porciatti, B. Morales, M. F. Bear, L. Maffei, and S. Tonegawa. Bdnf regulates the maturation of inhibition and the critical period of plasticity in mouse visual cortex. *Cell*, 98(6):739–755, Sep 1999. URL `http://www.pubmed.org/10499792`.

D. H. Hubel and T. N. Wiesel. Shape and arrangement of columns in cat's striate cortex. *J Physiol*, 165:559–568, Mar 1963. URL `http://www.pubmed.org/13955384`.

S. W. Jaslove. The integrative properties of spiny distal dendrites. *Neuroscience*, 47(3):495–519, Jan 1992. URL http://www.pubmed.org/1584406.

H. Jia, N. L. Rochefort, X. Chen, and A. Konnerth. Dendritic organization of sensory input to cortical neurons in vivo. *Nature*, 464(7293):1307–1312, Apr 2010. doi: 10.1038/nature08947. URL http://www.pubmed.org/20428163.

B. Judkewitz, A. Roth, and M. Häusser. Dendritic enlightenment: using patterned two-photon uncaging to reveal the secrets of the brain's smallest dendrites. *Neuron*, 50(2):180–183, Apr 2006. doi: 10.1016/j.neuron.2006.04.009. URL http://www.pubmed.org/16630828.

B. M. Kampa, J. J. Letzkus, and G. J. Stuart. Cortical feed-forward networks for binding different streams of sensory information. *Nat Neurosci*, 9(12):1472–1473, Dec 2006. doi: 10.1038/nn1798. URL http://www.pubmed.org/17099707.

E. M. Kasper, A. U. Larkman, J. Lübke, and C. Blakemore. Pyramidal neurons in layer 5 of the rat visual cortex. i. correlation among cell morphology, intrinsic electrophysiological properties, and axon targets. *J Comp Neurol*, 339(4):459–474, Jan 1994. doi: 10.1002/cne.903390402. URL http://www.pubmed.org/8144741.

T. Keck, T. D. Mrsic-Flogel, M. Vaz Afonso, U. T. Eysel, T. Bonhoeffer, and M. Hübener. Massive restructuring of neuronal circuits during functional reorganization of adult visual cortex. *Nat Neurosci*, 11(10):1162–1167, Oct 2008. doi: 10.1038/nn.2181. URL http://www.pubmed.org/18758460.

J. Kim, T. Zhao, R. S. Petralia, Y. Yu, H. Peng, E. Myers, and J. C. Magee. mgrasp enables mapping mammalian synaptic connectivity with light microscopy. *Nat Methods*, 9(1):96, Jan 2012. doi: 10.1038/nmeth.1784. URL http://www.pubmed.org/22138823.

T. Kleindienst, J. Winnubst, C. Roth-Alpermann, T. Bonhoeffer, and C. Lohmann. Activity-dependent clustering of functional synaptic inputs on developing hippocampal dendrites. *Neuron*, 72(6):1012–1024, Dec 2011. doi: 10.1016/j.neuron.2011.10.015. URL http://www.pubmed.org/22196336.

S. Kleinlogel, K. Feldbauer, R. E. Dempski, H. Fotis, P. G. Wood, C. Bamann, and E. Bamberg. Ultra light-sensitive and fast neuronal activation with the ca^2+-permeable channelrhodopsin catch. *Nat Neurosci*, 14(4):513–518, Apr 2011. doi: 10.1038/nn.2776. URL http://www.pubmed.org/21399632.

C. Koch and T. Poggio. A theoretical analysis of electrical properties of spines. *Proc R Soc Lond B Biol Sci*, 218(1213):455–477, Jul 1983a. URL http://www.pubmed.org/6136978.

C. Koch and T. Poggio. Electrical properties of dendritic spines. *Trends Neurosci*, 6:80–83, 1983b. doi: 10.1016/0166-2236(83)90043-7.

M. Kokaia, M. Andersson, and M. Ledri. An optogenetic approach in epilepsy. *Neuropharmacology*, 69:89–95, Jun 2013. doi: 10.1016/j.neuropharm.2012.05.049. URL http://www.pubmed.org/22698957.

M. E. Larkum, T. Nevian, M. Sandler, A. Polsky, and J. Schiller. Synaptic integration in tuft dendrites of layer 5 pyramidal neurons: a new unifying principle. *Science*, 325(5941):756–760, Aug 2009. doi: 10.1126/science.1171958. URL http://www.pubmed.org/19661433.

M. Lavzin, S. Rapoport, A. Polsky, L. Garion, and J. Schiller. Nonlinear dendritic processing determines angular tuning of barrel cortex neurons in vivo. *Nature*, 490(7420):397–401, Oct 2012. doi: 10.1038/nature11451. URL http://www.pubmed.org/22940864.

F. Leiss, E. Koper, I. Hein, W. Fouquet, J. Lindner, S. Sigrist, and G. Tavosanis. Characterization of dendritic spines in the drosophila central nervous system. *Dev Neurobiol*, 69(4):221–234, Mar 2009. doi: 10.1002/dneu.20699. URL http://www.pubmed.org/19160442.

J. Y. Lin, M. Z. Lin, P. Steinbach, and R. Y. Tsien. Characterization of engineered channelrhodopsin variants with improved properties and kinetics. *Biophys J*, 96(5):1803–1814, Mar 2009. doi: 10.1016/j.bpj.2008.11.034. URL http://www.pubmed.org/19254539.

J. Y. Lin, P. M. Knutsen, A. Muller, D. Kleinfeld, and R. Y. Tsien. Reachr: a red-shifted variant of channel-rhodopsin enables deep transcranial optogenetic excitation. *Nat Neurosci*, Sep 2013. doi: 10.1038/nn.3502. URL http://www.pubmed.org/23995068.

J. P. Little and A. G. Carter. Subcellular synaptic connectivity of layer 2 pyramidal neurons in the medial prefrontal cortex. *J Neurosci*, 32(37):12808–12819, Sep 2012. doi: 10.1523/JNEUROSCI.1616-12.2012. URL http://www.pubmed.org/22973004.

S. Q. Liu and S. G. Cull-Candy. Synaptic activity at calcium-permeable ampa receptors induces a switch in receptor subtype. *Nature*, 405(6785):454–458, May 2000. doi: 10.1038/35013064. URL http://www.pubmed.org/10839540.

M. London and M. Häusser. Dendritic computation. *Annu Rev Neurosci*, 28:503–532, Jan 2005. doi: 10.1146/annurev.neuro.28.061604.135703. URL http://www.pubmed.org/16033324.

M. London, A. Schreibman, M. Häusser, M. E. Larkum, and I. Segev. The information efficacy of a synapse. *Nat Neurosci*, 5(4):332–340, Apr 2002. doi: 10.1038/nn826. URL http://www.pubmed.org/11896396.

A. Losonczy and J. C. Magee. Integrative properties of radial oblique dendrites in hippocampal ca1 pyramidal neurons. *Neuron*, 50(2):291–307, Apr 2006. doi: 10.1016/j.neuron.2006.03.016. URL http://www.pubmed.org/16630839.

M. Ludwig and Q. J. Pittman. Talking back: dendritic neurotransmitter release. *Trends Neurosci*, 26(5): 255–261, May 2003. doi: 10.1016/S0166-2236(03)00072-9. URL http://www.pubmed.org/12744842.

X. Lv, C. Zhan, S. Zeng, W. R. Chen, and Q. Luo. Construction of multiphoton laser scanning microscope based on dual-axis acousto-optic deflector. *Rev Sci Instrum*, 77, 2006. doi: 10.1063/1.2190047.

J. C. Magee. Dendritic integration of excitatory synaptic input. *Nat Rev Neurosci*, 1(3):181–190, Dec 2000. doi: 10.1038/35044552. URL http://www.pubmed.org/11257906.

J. C. Magee and E. P. Cook. Somatic epsp amplitude is independent of synapse location in hippocampal pyramidal neurons. *Nat Neurosci*, 3(9):895–903, Sep 2000. URL http://www.pubmed.org/10966620.

J. C. Magee and D. Johnston. Synaptic activation of voltage-gated channels in the dendrites of hippocampal pyramidal neurons. *Science*, 268(5208):301–304, Apr 1995. URL http://www.pubmed.org/7716525.

J. C. Magee and D. Johnston. Plasticity of dendritic function. *Curr Opin Neurobiol*, 15(3):334–342, Jun 2005. doi: 10.1016/j.conb.2005.05.013. URL http://www.pubmed.org/15922583.

H. Makino and R. Malinow. Compartmentalized versus global synaptic plasticity on dendrites controlled by experience. *Neuron*, 72(6):1001–1011, Dec 2011. doi: 10.1016/j.neuron.2011.09.036. URL http://www.pubmed.org/22196335.

E. Marder and J.-M. Goaillard. Variability, compensation and homeostasis in neuron and network function. *Nat Rev Neurosci*, 7(7):563–574, Jul 2006. doi: 10.1038/nrn1949. URL http://www.pubmed.org/16791145.

T. W. Margrie, M. Brecht, and B. Sakmann. In vivo, low-resistance, whole-cell recordings from neurons in the anaesthetized and awake mammalian brain. *Pflugers Arch*, 444(4):491–498, Jul 2002. doi: 10.1007/s00424-002-0831-z. URL http://www.pubmed.org/12136268.

H. Markram, J. Lübke, M. Frotscher, A. Roth, and B. Sakmann. Physiology and anatomy of synaptic connections between thick tufted pyramidal neurones in the developing rat neocortex. *J Physiol*, 500 (Pt 2):409–440, Apr 1997. URL http://www.pubmed.org/9147328.

D. W. Marquardt. An algorithm for least-squares estimation of nonlinear parameters. *Journal of the Society for Industrial and Applied Mathematics*, 11(2):431–441, Jan 1963. doi: 10.1137/0111030.

M. Matsuzaki, G. C. Ellis-Davies, Y. Kanemoto, and H. Kasai. Simultaneous two-photon activation of presynaptic cells and calcium imaging in postsynaptic dendritic spines. *Neural Syst Circuits*, 1(1):2, Jan 2011. doi: 10.1186/2042-1001-1-2. URL http://www.pubmed.org/22330013.

K. D. Micheva and S. J. Smith. Array tomography: a new tool for imaging the molecular architecture and ultrastructure of neural circuits. *Neuron*, 55(1):25–36, Jul 2007. doi: 10.1016/j.neuron.2007.06.014. URL http://www.pubmed.org/17610815.

J. P. Miller, W. Rall, and J. Rinzel. Synaptic amplification by active membrane in dendritic spines. *Brain Res*, 325(1-2):325–330, Jan 1985. URL http://www.pubmed.org/2983830.

V. B. Mountcastle. Modality and topographic properties of single neurons of cat's somatic sensory cortex. *J Neurophysiol*, 20(4):408–434, Jul 1957. URL http://www.pubmed.org/13439410.

V. B. Mountcastle. The columnar organization of the neocortex. *Brain*, 120 (Pt 4):701–722, Apr 1997. URL http://www.pubmed.org/9153131.

W. Müller and J. A. Connor. Dendritic spines as individual neuronal compartments for synaptic ca2+ responses. *Nature*, 354(6348):73–76, Nov 1991. URL http://www.pubmed.org/1682815.

G. Nagel, T. Szellas, W. Huhn, S. Kateriya, N. Adeishvili, P. Berthold, D. Ollig, P. Hegemann, and E. Bamberg. Channelrhodopsin-2, a directly light-gated cation-selective membrane channel. *Proc Natl Acad Sci U S A*, 100(24):13940–13945, Nov 2003. doi: 10.1073/pnas.1936192100. URL http://www.pubmed.org/14615590.

V. Nikolenko, K. E. Poskanzer, and R. Yuste. Two-photon photostimulation and imaging of neural circuits. *Nat Methods*, 4(11):943–950, Nov 2007. doi: 10.1038/nmeth1105. URL http://www.pubmed.org/17965719.

E. A. Nimchinsky, B. L. Sabatini, and K. Svoboda. Structure and function of dendritic spines. *Annu Rev Physiol*, 64:313–353, Jan 2002. doi: 10.1146/annurev.physiol.64.081501.160008. URL http://www.pubmed.org/11826272.

H. Niwa, K. Yamamura, and J. Miyazaki. Efficient selection for high-expression transfectants with a novel eukaryotic vector. *Gene*, 108(2):193–199, Dec 1991. URL http://www.pubmed.org/1660837.

Y. Otsu, V. Bormuth, J. Wong, B. Mathieu, G. P. Dugué, A. Feltz, and S. Dieudonné. Optical monitoring of neuronal activity at high frame rate with a digital random-access multiphoton (ramp) microscope. *J Neurosci Methods*, 173(2):259–270, Aug 2008. doi: 10.1016/j.jneumeth.2008.06.015. URL http://www.pubmed.org/18634822.

S. L. Palay and G. E. Palade. The fine structure of neurons. *J Biophys Biochem Cytol*, 1(1):69–88, Jan 1955. URL http://www.pubmed.org/14381429.

L. M. Palmer and G. J. Stuart. Membrane potential changes in dendritic spines during action potentials and synaptic input. *J Neurosci*, 29(21):6897–6903, May 2009. doi: 10.1523/JNEUROSCI.5847-08.2009. URL http://www.pubmed.org/19474316.

P. Paoletti, C. Bellone, and Q. Zhou. Nmda receptor subunit diversity: impact on receptor properties, synaptic plasticity and disease. *Nat Rev Neurosci*, 14(6):383–400, Jun 2013. doi: 10.1038/nrn3504. URL http://www.pubmed.org/23686171.

A. Peters and M. L. Feldman. The projection of the lateral geniculate nucleus to area 17 of the rat cerebral cortex. i. general description. *J Neurocytol*, 5(1):63–84, Feb 1976. URL http://www.pubmed.org/1249593.

A. Peters and I. R. Kaiserman-Abramof. The small pyramidal neuron of the rat cerebral cortex. the perikaryon, dendrites and spines. *Am J Anat*, 127(4):321–355, Apr 1970. URL http://www.pubmed.org/4985058.

A. Peters and B. R. Payne. Numerical relationships between geniculocortical afferents and pyramidal cell modules in cat primary visual cortex. *Cereb Cortex*, 3(1):69–78, Jan 1993. URL http://www.pubmed.org/8439740.

L. Petreanu, D. Huber, A. Sobczyk, and K. Svoboda. Channelrhodopsin-2-assisted circuit mapping of long-range callosal projections. *Nat Neurosci*, 10(5):663–668, May 2007. doi: 10.1038/nn1891. URL http://www.pubmed.org/17435752.

L. Petreanu, T. Mao, S. M. Sternson, and K. Svoboda. The subcellular organization of neocortical excitatory connections. *Nature*, 457(7233):1142–1145, Feb 2009. doi: 10.1038/nature07709. URL http://www.pubmed.org/19151697.

R. A. Piskorowski and V. Chevaleyre. Synaptic integration by different dendritic compartments of hippocampal ca1 and ca2 pyramidal neurons. *Cell Mol Life Sci*, 69(1):75–88, Jan 2012. doi: 10.1007/s00018-011-0769-4. URL http://www.pubmed.org/21796451.

P. Poirazi and B. W. Mel. Impact of active dendrites and structural plasticity on the memory capacity of neural tissue. *Neuron*, 29(3):779–796, Mar 2001. URL http://www.pubmed.org/11301036.

A. Polsky, B. W. Mel, and J. Schiller. Computational subunits in thin dendrites of pyramidal cells. *Nat Neurosci*, 7(6):621–627, Jun 2004. doi: 10.1038/nn1253. URL http://www.pubmed.org/15156147.

M. Prigge, F. Schneider, S. P. Tsunoda, C. Shilyansky, J. Wietek, K. Deisseroth, and P. Hegemann. Color-tuned channelrhodopsins for multiwavelength optogenetics. *J Biol Chem*, Jul 2012. doi: 10.1074/jbc.M112.391185. URL http://www.pubmed.org/22843694.

W. Rall. Time constants and electrotonic length of membrane cylinders and neurons. *Biophys J*, 9(12):1483–1508, Dec 1969a. doi: 10.1016/S0006-3495(69)86467-2. URL http://www.ncbi.nlm.nih.gov/pmc/articles/PMC1367649/.

W. Rall. Distributions of potential in cylindrical coordinates and time constants for a membrane cylinder. *Biophys J*, 9(12):1509–1541, Dec 1969b. doi: 10.1016/S0006-3495(69)86468-4. URL http://www.ncbi.nlm.nih.gov/pmc/articles/PMC1367650/.

W. Rall and J. Rinzel. Branch input resistance and steady attenuation for input to one branch of a dendritic neuron model. *Biophys J*, 13(7):648–687, Jul 1973. URL http://www.pubmed.org/4715583.

W. G. Regehr, M. R. Carey, and A. R. Best. Activity-dependent regulation of synapses by retrograde messengers. *Neuron*, 63(2):154–170, Jul 2009. doi: 10.1016/j.neuron.2009.06.021. URL http://www.pubmed.org/19640475.

S. Remy, J. Csicsvari, and H. Beck. Activity-dependent control of neuronal output by local and global dendritic spike attenuation. *Neuron*, 61(6):906–916, Mar 2009. doi: 10.1016/j.neuron.2009.01.032. URL http://www.pubmed.org/19323999.

S. Remy, H. Beck, and Y. Yaari. Plasticity of voltage-gated ion channels in pyramidal cell dendrites. *Curr Opin Neurobiol*, 20(4):503–509, Aug 2010. doi: 10.1016/j.conb.2010.06.006. URL http://www.pubmed.org/20691582.

R. J. Richardson, J. A. Blundon, I. T. Bayazitov, and S. S. Zakharenko. Connectivity patterns revealed by mapping of active inputs on dendrites of thalamorecipient neurons in the auditory cortex. *J Neurosci*, 29(20): 6406–6417, May 2009. doi: 10.1523/JNEUROSCI.0258-09.2009. URL http://www.pubmed.org/19458212.

J. Rinzel and W. Rall. Transient response in a dendritic neuron model for current injected at one branch. *Biophys J*, 14(10):759–790, Oct 1974. URL http://www.pubmed.org/4424185.

N. L. Rochefort and A. Konnerth. Dendritic spines: from structure to in vivo function. *EMBO Rep*, 13(8): 699–708, Aug 2012. doi: 10.1038/embor.2012.102. URL http://www.pubmed.org/22791026.

M.-P. Rols. Mechanism by which electroporation mediates dna migration and entry into cells and targeted tissues. *Methods Mol Biol*, 423:19–33, Jan 2008. URL http://www.pubmed.org/18370188.

B. L. Sabatini, M. Maravall, and K. Svoboda. Ca(2+) signaling in dendritic spines. *Curr Opin Neurobiol*, 11 (3):349–356, Jun 2001. URL http://www.pubmed.org/11399434.

B. L. Sabatini, T. G. Oertner, and K. Svoboda. The life cycle of ca(2+) ions in dendritic spines. *Neuron*, 33(3): 439–452, Jan 2002. URL http://www.pubmed.org/11832230.

R. K. Saiki, D. H. Gelfand, S. Stoffel, S. J. Scharf, R. Higuchi, G. T. Horn, K. B. Mullis, and H. A. Erlich. Primer-directed enzymatic amplification of dna with a thermostable dna polymerase. *Science*, 239:487–491, Jan 1988. doi: 10.1126/science.2448875. URL http://adsabs.harvard.edu/abs/1988Sci...239..487S.

T. Saito and N. Nakatsuji. Efficient gene transfer into the embryonic mouse brain using in vivo electroporation. *Dev Biol*, 240(1):237–246, Dec 2001. doi: 10.1006/dbio.2001.0439. URL http://www.pubmed.org/11784059.

T. R. Sato, N. W. Gray, Z. F. Mainen, and K. Svoboda. The functional microarchitecture of the mouse barrel cortex. *PLoS Biol*, 5(7):e189, Jul 2007. doi: 10.1371/journal.pbio.0050189. URL http://www.pubmed.org/17622195.

B. Sauer. Inducible gene targeting in mice using the cre/lox system. *Methods*, 14(4):381–392, Apr 1998. doi: 10.1006/meth.1998.0593. URL http://www.pubmed.org/9608509.

V. Scheuss and T. Bonhoeffer. Function of dendritic spines on hippocampal inhibitory neurons. *Cereb Cortex*, Jul 2013. doi: 10.1093/cercor/bht171. URL http://www.pubmed.org/23825320.

V. Scheuss, R. Yasuda, A. Sobczyk, and K. Svoboda. Nonlinear [ca2+] signaling in dendrites and spines caused by activity-dependent depression of ca2+ extrusion. *J Neurosci*, 26(31):8183–8194, Aug 2006. doi: 10.1523/JNEUROSCI.1962-06.2006. URL http://www.pubmed.org/16885232.

A. Schüz and G. Palm. Density of neurons and synapses in the cerebral cortex of the mouse. *J Comp Neurol*, 286(4):442–455, Aug 1989. doi: 10.1002/cne.902860404. URL http://www.pubmed.org/2778101.

I. Segev and W. Rall. Computational study of an excitable dendritic spine. *J Neurophysiol*, 60(2):499–523, Aug 1988. URL http://www.pubmed.org/2459320.

G. M. Shepherd and R. K. Brayton. Logic operations are properties of computer-simulated interactions between excitable dendritic spines. *Neuroscience*, 21(1):151–165, Apr 1987. URL http://www.pubmed.org/3601072.

G. M. G. Shepherd, A. Stepanyants, I. Bureau, D. Chklovskii, and K. Svoboda. Geometric and functional organization of cortical circuits. *Nat Neurosci*, 8(6):782–790, Jun 2005. doi: 10.1038/nn1447. URL http://www.pubmed.org/15880111.

V. A. Skeberdis, V. Chevaleyre, C. G. Lau, J. H. Goldberg, D. L. Pettit, S. O. Suadicani, Y. Lin, M. V. L. Bennett, R. Yuste, P. E. Castillo, and R. S. Zukin. Protein kinase a regulates calcium permeability of nmda receptors. *Nat Neurosci*, 9(4):501–510, Apr 2006. doi: 10.1038/nn1664. URL http://www.pubmed.org/16531999.

I. Song and R. L. Huganir. Regulation of ampa receptors during synaptic plasticity. *Trends Neurosci*, 25(11): 578–588, Nov 2002. URL http://www.pubmed.org/12392933.

K. E. Sorra and K. M. Harris. Overview on the structure, composition, function, development, and plasticity of hippocampal dendritic spines. *Hippocampus*, 10(5):501–511, Jan 2000. URL http://www.pubmed.org/11075821.

N. Spruston. Pyramidal neurons: dendritic structure and synaptic integration. *Nat Rev Neurosci*, 9(3):206–221, Mar 2008. doi: 10.1038/nrn2286. URL http://www.pubmed.org/18270515.

A. Stepanyants and D. B. Chklovskii. Neurogeometry and potential synaptic connectivity. *Trends Neurosci*, 28 (7):387–394, Jul 2005. doi: 10.1016/j.tins.2005.05.006. URL http://www.pubmed.org/15935485.

A. Stepanyants, P. R. Hof, and D. B. Chklovskii. Geometry and structural plasticity of synaptic connectivity. *Neuron*, 34(2):275–288, Apr 2002. URL http://www.pubmed.org/11970869.

G. J. Stuart and M. Häusser. Dendritic coincidence detection of epsps and action potentials. *Nat Neurosci*, 4 (1):63–71, Jan 2001. doi: 10.1038/82910. URL http://www.pubmed.org/11135646.

G. J. Stuart and N. Spruston. Determinants of voltage attenuation in neocortical pyramidal neuron dendrites. *J Neurosci*, 18(10):3501–3510, May 1998. URL http://www.pubmed.org/9570781.

G. J. Stuart, N. Spruston, B. Sakmann, and M. Häusser. Action potential initiation and backpropagation in neurons of the mammalian cns. *Trends Neurosci*, 20(3):125–131, Mar 1997. URL http://www.pubmed.org/9061867.

K. Svoboda and R. Yasuda. Principles of two-photon excitation microscopy and its applications to neuroscience. *Neuron*, 50(6):823–839, Jun 2006. doi: 10.1016/j.neuron.2006.05.019. URL http://www.pubmed.org/16772166.

N. V. Swindale. Dendritic spines only connect. *Trends Neurosci*, 4:240–241, Sep 1981. doi: 10.1016/0166-2236(81)90075-8.

N. Takahashi, K. Kitamura, N. Matsuo, M. Mayford, M. Kano, N. Matsuki, and Y. Ikegaya. Locally synchronized synaptic inputs. *Science*, 335(6066):353–356, Jan 2012. doi: 10.1126/science.1210362. URL http://www.pubmed.org/22267814.

A. Tashiro and R. Yuste. Structure and molecular organization of dendritic spines. *Histol Histopathol*, 18(2): 617–634, Apr 2003. URL http://www.pubmed.org/12647812.

A. M. Thomson, D. C. West, Y. Wang, and A. P. Bannister. Synaptic connections and small circuits involving excitatory and inhibitory neurons in layers 2-5 of adult rat and cat neocortex: triple intracellular recordings and biocytin labelling in vitro. *Cereb Cortex*, 12(9):936–953, Sep 2002. URL http://www.pubmed.org/12183393.

M. K. Trower. A rapid pcr-based colony screening protocol for cloned inserts. *Methods Mol Biol*, 58:329–333, Jan 1996. doi: 10.1385/0-89603-402-X:329. URL http://www.pubmed.org/8713880.

T. V. Truong, W. Supatto, D. S. Koos, J. M. Choi, and S. E. Fraser. Deep and fast live imaging with two-photon scanned light-sheet microscopy. *Nat Methods*, 8(9):757–760, Sep 2011. doi: 10.1038/nmeth.1652. URL http://www.pubmed.org/21765409.

D. Tsay and R. Yuste. On the electrical function of dendritic spines. *Trends Neurosci*, 27(2):77–83, Feb 2004. doi: 10.1016/j.tins.2003.11.008. URL http://www.pubmed.org/15102486.

Z. Varga, H. Jia, B. Sakmann, and A. Konnerth. Dendritic coding of multiple sensory inputs in single cortical neurons in vivo. *Proc Natl Acad Sci U S A*, 108(37):15420–15425, Sep 2011. doi: 10.1073/pnas.1112355108. URL http://www.pubmed.org/21876170.

P. Vetter, A. Roth, and M. Häusser. Propagation of action potentials in dendrites depends on dendritic morphology. *J Neurophysiol*, 85(2):926–937, Feb 2001. URL http://www.pubmed.org/11160523.

H. Wang, J. Peca, M. Matsuzaki, K. Matsuzaki, J. Noguchi, L. Qiu, D. Wang, F. Zhang, E. Boyden, K. Deisseroth, H. Kasai, W. C. Hall, G. Feng, and G. J. Augustine. High-speed mapping of synaptic connectivity using photostimulation in channelrhodopsin-2 transgenic mice. *Proc Natl Acad Sci U S A*, 104 (19):8143–8148, May 2007. doi: 10.1073/pnas.0700384104. URL http://www.pubmed.org/17483470.

S. R. Williams. Spatial compartmentalization and functional impact of conductance in pyramidal neurons. *Nat Neurosci*, 7(9):961–967, Sep 2004. doi: 10.1038/nn1305. URL http://www.pubmed.org/15322550.

S. R. Williams and G. J. Stuart. Dependence of epsp efficacy on synapse location in neocortical pyramidal neurons. *Science*, 295(5561):1907–1910, Mar 2002. doi: 10.1126/science.1067903. URL http://www.pubmed.org/11884759.

J. Winnubst and C. Lohmann. Synaptic clustering during development and learning: the why, when, and how. *Front Mol Neurosci*, 5:70, Jan 2012. doi: 10.3389/fnmol.2012.00070. URL http://www.pubmed.org/22666187.

N.-l. Xu, M. T. Harnett, S. R. Williams, D. Huber, D. H. O'Connor, K. Svoboda, and J. C. Magee. Nonlinear dendritic integration of sensory and motor input during an active sensing task. *Nature*, 492(7428):247–251, Dec 2012. doi: 10.1038/nature11601. URL http://www.pubmed.org/23143335.

Y. Yoshimura, J. L. M. Dantzker, and E. M. Callaway. Excitatory cortical neurons form fine-scale functional networks. *Nature*, 433(7028):868–873, Feb 2005. doi: 10.1038/nature03252. URL http://www.pubmed.org/15729343.

R. Yuste. Dendritic spines and distributed circuits. *Neuron*, 71(5):772–781, Sep 2011. doi: 10.1016/j.neuron.2011.07.024. URL http://www.pubmed.org/21903072.

R. Yuste. Electrical compartmentalization in dendritic spines. *Annu Rev Neurosci*, 36:429–449, Jul 2013. doi: 10.1146/annurev-neuro-062111-150455. URL http://www.pubmed.org/23724997.

R. Yuste and T. Bonhoeffer. Morphological changes in dendritic spines associated with long-term synaptic plasticity. *Annu Rev Neurosci*, 24:1071–1089, Jan 2001. URL http://www.pubmed.org/11520928.

R. Yuste and W. Denk. Dendritic spines as basic functional units of neuronal integration. *Nature*, 375(6533):682–684, Jun 1995. doi: 10.1038/375682a0. URL http://www.pubmed.org/7791901.

F. Zhang, A. M. Aravanis, A. Adamantidis, L. de Lecea, and K. Deisseroth. Circuit-breakers: optical technologies for probing neural signals and systems. *Nat Rev Neurosci*, 8(8):577–581, Aug 2007a. doi: 10.1038/nrn2192. URL http://www.pubmed.org/17643087.

F. Zhang, L.-P. Wang, M. Brauner, J. F. Liewald, K. Kay, N. Watzke, P. G. Wood, E. Bamberg, G. Nagel, A. Gottschalk, and K. Deisseroth. Multimodal fast optical interrogation of neural circuitry. *Nature*, 446 (7136):633–639, Apr 2007b. doi: 10.1038/nature05744. URL http://www.pubmed.org/17410168.

Y.-P. Zhang and T. G. Oertner. Optical induction of synaptic plasticity using a light-sensitive channel. *Nat Methods*, 4(2):139–141, Feb 2007. doi: 10.1038/nmeth988. URL http://www.pubmed.org/17195846.

W. R. Zipfel, R. M. Williams, and W. W. Webb. Nonlinear magic: multiphoton microscopy in the biosciences. *Nat Biotechnol*, 21(11):1369–1377, Nov 2003. doi: 10.1038/nbt899. URL http://www.pubmed.org/14595365.

R. S. Zucker. Calcium- and activity-dependent synaptic plasticity. *Curr Opin Neurobiol*, 9(3):305–313, Jun 1999. URL http://www.pubmed.org/10395573.

R. Zufferey, J. E. Donello, D. Trono, and T. J. Hope. Woodchuck hepatitis virus posttranscriptional regulatory element enhances expression of transgenes delivered by retroviral vectors. *J Virol*, 73(4):2886–2892, Apr 1999. URL http://www.pubmed.org/10074136.

Eidesstattliche Versicherung/Affidavit

Hiermit versichere ich an Eides statt, dass ich die vorliegende Dissertation "Channelrhodopsin Assisted Synapse Identity Mapping Reveals Clustering of Layer 5 Intralaminar Inputs" selbstständig angefertigt habe, mich außer der angegebenen keiner weiteren Hilfsmittel bedient und alle Erkenntnisse, die aus dem Schrifttum ganz oder annähernd übernommen sind, als solche kenntlich gemacht und nach ihrer Herkunft unter Bezeichnung der Fundstelle einzeln nachgewiesen habe.

I hereby confirm that the dissertation "Channelrhodopsin Assisted Synapse Identity Mapping Reveals Clustering of Layer 5 Intralaminar Inputs" is the result of my own work and that I have only used sources or materials listed and specified in the dissertation.

München/Munich,   Onur Gökçe
16.10.2013